

**Numerical investigation of two phase flow using automatic controller
system and chaotic approach**

A Dissertation

Presented to

The Faculty of the Graduate School

University of Missouri

In Partial Fulfillment

of the Requirement for the Degree

Doctor of Philosophy

By

Sam Pouryoussefi

Dissertation Supervisor: Dr. Yuwen Zhang

May 2016

The undersigned, appointed by the dean of the Graduate School, have examined the
dissertation entitled

**Numerical investigation of two phase flow using automatic controller system and
chaotic approach**

Presented by Sam Pouryoussefi,

a candidate for the degree of doctor of philosophy,

and hereby certify that, in their opinion, it is worthy of acceptance.

Professor Yuwen Zhang

Professor Frank Feng

Professor Chung-Lung Chen

Professor Chanwoo Park

Professor Mahmoud Almasri

Acknowledgement

I am highly grateful to my supervisor Dr. Yuwen Zhang, Chairman of the department of Mechanical and Aerospace Engineering for his encouragement, support, patience and guidance throughout this research work also in daily life. This dissertation would not have been possible without guidance and help of him. I would like to thank the member of my thesis evaluation committee, Dr. Frank Feng, Dr. C.L Chen, Dr. Chanwoo Park and Dr. Mahmoud Almasri for giving the time to provide valuable comments and criticisms. I would like to express my gratitude to my parents, Hamid Pouryoussefi and Manijeh Yaghmai. Last but not least, I want to thank my wife Ela Nadafy for her support and understanding.

Support for this work by the U.S. National Science Foundation under grant number CBET-1066917 is gratefully acknowledged.

Table of contents

Acknowledgement	ii
List of Figures.....	vi
Table Captions.....	xiii
Nomenclature	xiv
Abstract	xvii
Chapter 1: Introduction	1
Chapter 2: Two phase flow pattern identification and fuzzy logic	13
2.1 Geometry configuration.....	15
2.2 Governing Equation.....	17
2.2.1 Continuity equation.....	18
2.2.2 Momentum equation for VOF model.....	19
2.2.3 Turbulence model	21
2.3 Results and Discussions.....	23
2.3.1 Turbulence modeling and grid independence test	23
2.3.2 Flow patterns simulation	27
2.3.3 Image Processing	35

2.3.4 Fuzzy Logic and Genetic Algorithm.....	41
2.4 Conclusion	53
Chapter 3: Numerical simulation of flow in a 2D pulsating heat pipe	54
3.1 Physical Modeling and Governing equations	54
3.1.1 The VOF Model.....	56
3.1.2 Energy Equation.....	57
3.1.3 Wall Adhesion	58
3.2 Chaos	59
3.2.1 Examples of Chaos application.....	61
3.3 Results and Discussion	63
3.3.1 Volume fractions and Time series Analysis	63
3.3.1.1. Correlation Dimension Analysis.....	83
3.3.1.2. Power spectrum Density Analysis.....	86
3.3.1.3. Lyapunov Exponent Analysis.....	89
3.3.1.4. Autocorrelation function Analysis.....	92
3.4 Conclusions	94
Chapter 4: Numerical simulation of flow in a 2D multi-turn pulsating heat pipe.....	96
4.1 Physical modeling	97
4.2 Results and discussion	100

4.2.1 Non-linear temperature oscillations	110
4.2.2 Correlation dimension and Autocorrelation function	113
4.2.3 Thermal behavior	117
4.3. Conclusion	121
Chapter 5: Nonlinear analysis of chaotic flow in a 3D closed-loop pulsating heat pipe	122
5.1 Physical modeling.....	123
5.2 Results and Discussions.....	126
5.2.1 Volume Fractions.....	129
5.2.2 Spectral Analysis of Time Series	140
5.2.3 Correlation Dimension	149
5.2.4 Autocorrelation Function.....	152
5.2.5 Lyapunov Exponent	155
5.2.6 Phase Space Reconstruction	158
5.2.7 Thermal Performance.....	162
5.3 Conclusion	165
Reference	167
VITA	177

List of Figures

Figure 1.1. Air-Water two phase flow in vertical pipe with different flow patterns	2
Figure 1.2. Schematic closed loop pulsating heat pipe	7
Figure 2.2. Three air and three water inlets (the green color shows the air inlets).....	15
Figure 2.1. Grid mesh used in the study (not in scale).....	16
Figure 2.3. K- ϵ Standard turbulence modeling.....	23
Figure 2.4. K- ϵ realizable turbulence modeling.....	24
Figure 2.5. K- ϵ RNG turbulence modeling.....	25
Figure 2.6. Reynolds stress turbulence modeling.....	26
Figure 2.7. Grid independency investigation.....	27
Figure 2.8. Void fraction contours for bubbly flow.....	28
Figure 2.9. Void fraction contours for bubbly- slug flow.....	30
Figure 2.10. Void fraction contours for slug flow.....	32
Figure 2.11. Void fraction contours for slug- churn flow.....	33
Figure 2.12. Void fraction contours for churn flow.....	34
Figure 2.13. Void fraction contours for annular flow.....	35

Figure 2.14. Image processing on an image obtained from simulation.....	37
Figure 2.15. Input (a) and Output (b) membership functions.....	42
Figure 2.16. First (a), Second (b), Third (c) and Forth (d) input membership functions...	45
Figure 2.17. Comparison of Hewitt map with fuzzy logic results.....	52
Figure 3.1. Pulsating heat pipe structure.....	55
Figure 3.2. Meshing configuration (not in scale).....	55
Figure 3.3. Double Pendulum Motion.....	61
Figure 3.4. Location plot of the pendulum motion.....	62
Figure 3.5. Volume fractions for $T_h=145\text{ }^\circ\text{C}$, $T_c=35\text{ }^\circ\text{C}$ and filling ratio of 30%.....	68
Figure 3.6. Volume fractions for $T_h=150\text{ }^\circ\text{C}$, $T_c=35\text{ }^\circ\text{C}$ and filling ratio of 60%.....	72
Figure 3.7. Liquid and vapor plugs in the vertical tube of the PHP.....	73
Figure 3.8. Liquid film around the vapor plugs at evaporator, condenser and adiabatic sections.....	74
Figure 3.9. Formation and growing of the vapor bubble inside the liquid plug.....	74
Figure 3.10. Vapor bubbles combination in evaporator.....	75
Figure 3.11. Vapor bubbles combination in adiabatic section.....	76
Figure 3.12. Vapor condensation and liquid accumulation on the condenser surfaces.....	76

Figure 3.13. Liquid droplet formation at the bottom of the condenser.....	77
Figure 3.14. Time series of temperature for the adiabatic walls; (a): wall #1, (b): wall #4, (c): wall #8	79
Figure 3.15. Formation of abnormal vapor plugs in evaporator.....	82
Figure 3.16. Correlation dimension values (D_c).....	85
Figure 3.17. Power spectrum density of the times series of temperature for the adiabatic walls; (a): wall #1, (b): wall #4, (c): wall #8.....	88
Figure 3.18. Lyapunov exponents as a function of evaporator temperature at different filling ratios.....	91
Figure 3.19. Autocorrelation function versus time.....	93
Figure 4.1. Pulsating heat pipe structure.....	98
Figure 4.2. Meshing configuration.....	99
Figure 4.3. Volume fractions of liquid and vapor at different times with $Q=40$ W, $T_c=30$ °C and $FR= 35\%$; (a): $t=0.1$ s, (b): $t=1.7$ s, (c): $t=20$ s.....	103
Figure 4.4. Volume fractions of liquid and vapor at different times with $Q=55$ W, $T_c=25$ °C and $FR= 60\%$; (a): $t=0.1$ s, (b): $t=2.6$ s, (c): $t=20$ s.....	106
Figure 4.5. Vapor and liquid plugs in the PHP.....	107

Figure 4.6. Comparing formation of abnormal vapor plugs (a) with normal vapor plugs (b) at evaporator.....	108
Figure 4.7. Temperature oscillations at evaporator (a) and adiabatic wall (b).....	111
Figure 4.8. Power spectrum density of the adiabatic wall temperature time series (point #4).....	112
Figure 4.9. Correlation dimension values (Dc).....	114
Figure 4.10. Autocorrelation function versus time.....	116
Figure 4.11. Axial mean temperature distribution for heating powers of 55 W (a) and 40 W (b).....	117
Figure 4.12. Thermal resistance versus heating power.....	120
Figure 5.2. Meshing configuration.....	124
Figure 5.1. Schematic cross sectional view of the 3D PHP.....	125
Figure 5.3. Comparison of thermal resistance versus heating power between simulation results of current study and experimental results of reference	128
Figure 5.4. Volume fractions of liquid and vapor at t=0.1 s under heating power of 70 W and condenser temperature of 20 °C for ethanol, FR of 40% (a) and water, FR of 65% (b).....	129

Figure 5.5. Volume fractions of liquid and vapor under heating power of 70 W and condenser temperature of 20 °C for ethanol as working fluid with FR of 40% at t=0.8 s.....	131
Figure 5.6. Volume fractions of liquid and vapor under heating power of 70 W and condenser temperature of 20 °C for ethanol as working fluid with FR of 40% at t=20 s.....	132
Figure 5.7. Volume fractions of liquid and vapor under heating power of 70 W and condenser temperature of 20 °C for water as working fluid with FR of 65% at t=0.8 s.....	133
Figure 5.8. Volume fractions of liquid and vapor under heating power of 70 W and condenser temperature of 20 °C for water as working fluid with FR of 65% at t=20 s.....	134
Figure 5.9. Vapor and liquid plugs in the PHP.....	135
Figure 5.10 Liquid film around the vapor plugs at evaporator (a), adiabatic section (b) and condenser (c).....	137
Figure 5.11. Liquid film thickness versus heating power.....	138
Figure 5.12. Vapor bubbles combination.....	139
Figure 5.13. Time series of temperature (a) and PSD diagram (b) for point #16 under heating power of 90 W, condenser temperature of 20 °C, filling ratio of 45% and water as working fluid.....	142

Figure 5.14. Time series of temperature (a) and PSD diagram (b) for point #11 under heating power of 90 W, condenser temperature of 20 °C, filling ratio of 55% and ethanol as working fluid.....144

Figure 5.15. Time series of temperature (a) and PSD diagram (b) for point #20 under heating power of 90 W, condenser temperature of 20 °C, filling ratio of 70% and water as working fluid.....146

Figure 5.16. Time series of temperature (a) and PSD diagram (b) for point #25 under heating power of 90 W, condenser temperature of 20 °C, filling ratio of 65% and ethanol as working fluid.....148

Figure 5.17. Correlation dimension values (D_c) with water (a) and ethanol (b) as working fluids.....151

Figure 5.18 Autocorrelation function versus time with water (a) and ethanol (b) as working fluids.....154

Figure 5.19. Lyapunov exponents versus evaporator heating power at different filling ratios with water (a) and ethanol (b) as working fluids.....157

Figure 5.20. Reconstructed 3D attractor patterns under (a): heating power of 75 W, condenser temperature of 20 °C, filling ratio of 55% and ethanol as working fluid (b): heating power of 40 W, condenser temperature of 20 °C, filling ratio of 60% and water as working fluid (c): heating power of 80 W, condenser temperature of 20 °C, filling ratio of 65% and ethanol as working fluid.....161

Figure 5.21. Thermal resistance versus heating power at different filling ratios and water as working fluid.....	163
Figure 5.22 Thermal resistance versus heating power at different filling ratios and ethanol as working fluid.....	164

Table Captions

Table 2.1. Results obtained from image processing for bubbly and slug flow patterns.....	39
Table 2.2. Results obtained from image processing for churn and annular flow pattern.....	40
Table 2.3. Rules of fuzzy algorithm.....	47
Table 2.4. Flow pattern identification by fuzzy logic and Hewitt map for Bubbly and Slug.....	48
Table 2.5. Flow pattern identification by fuzzy logic and Hewitt map for Churn and Annular.....	50

Nomenclature

T Temperature ($^{\circ}\text{C}$)

g Gravity Acceleration (m/s^2)

F Body Force (N)

A Cross-sectional Area (m^2)

D Diameter of the tube (m)

f Friction factor

P Pressure (N/m^2)

\dot{q} Heat flux (W/m^2)

R_{th} Thermal resistance (K/W)

C_p Specific Heat (J/Kg.K)

k Thermal Conductivity (W/m.K)

L Length (m)

\dot{m}_{qp} mass transfer from phase q to phase p (kg/s)

\dot{m}_{pq} mass transfer from phase p to phase q (kg/s)

S_{aq} Source term

V Volume of cell

U_f Volume flux through the face, based on normal velocity

\mathbf{v} Velocity (m/s)

E Energy (J)

S_h Source term

R Radius for surface tension

\mathbf{n} Surface normal vector

K Curvature

$C(r)$ Correlation dimension

F_{vol} Volume force at the surface

N Number of data points in the attractor

f Frequency (Hz)

T Time period (s)

PSD Power spectrum density (W/Hz)

ACF Autocorrelation function

Greek Symbols

λ Lyapunov exponent

τ Delay component, Lag

σ Surface tension (N/m)

ρ Density (Kg/m³)

μ Dynamic viscosity (N.s/m²)

α_q q^{th} fluid's volume fraction in the cell

θ_w Contact angle at the wall

Abstract

An automatic and intelligent system to recognize the two-phase water-air flow regime in a vertical tube based on fuzzy logic and genetic algorithm is proposed. Two approaches, volume of fluid (VOF) and Eulerian model, were used for the numerical simulation of gas-liquid two-phase flow. Four different turbulence models, i.e., k- ϵ RNG, k- ϵ standard, Reynolds stress and k- ϵ realizable, were employed. Image processing procedure was implemented to obtain the flow pattern. It was found that the k- ϵ RNG gives best results for turbulence modeling and the fuzzy logic code predicts the flow pattern well. In addition, in the present study investigation of chaotic flow in a two and three dimensional closed-loop pulsating heat pipe has been carried out numerically. Constant temperature and heat flux boundary conditions have been applied for the heating (evaporator) section and only constant temperature for cooling (condenser) section. Water and ethanol were as used as working fluids. Volume of Fluid (VOF) method has been employed for two-phase flow simulation. Volume fraction of liquid and vapor in the pulsating heat pipe was investigated under different operating conditions. Approaches such as spectral analysis of temperature time series, correlation dimension, autocorrelation function, Lyapunov exponent and phase space reconstruction were used to investigate chaos in the pulsating heat pipe. Thermal resistance behavior was analyzed with respect to heating power and optimal points were found in case of thermal performance of the pulsating heat pipe. Spectral analysis of temperature time series using Power Spectrum Density showed existence of dominant peak in PSD diagram indicates periodic or quasi-periodic behavior in temperature oscillations at particular frequencies. Correlation dimension values for ethanol were higher than water under the same operating conditions.

High values of correlation dimension referred to high frequency, small scale temperature oscillations, caused by miniature bubbles or short vapor plugs dynamically flowing in PHP tubes. Decay of autocorrelation function with respect to time indicated finite prediction ability of the system. Change in working fluid did not lead to any particular conclusion for ACF behavior. An O-ring structure pattern was obtained for reconstructed 3D attractor at periodic or quasi-periodic behavior of temperature oscillations.

Chapter 1

Introduction

Multiphase flow problem is related to energy, process engineering, oil and gas industry and many other engineering areas. The features of the flow pattern in a multiphase flow are of significant importance in design and implementation in industrial processes. Figure 1.1 shows Air-Water two phase flow in vertical pipe with different flow patterns. Two-phase flow in vertical pipes is encountered in several plants in the chemical and in the nuclear fields. The chemical industries utilize vertical pipes in bubble columns and in fluidized beds for heat and mass transfer operations. In the nuclear industry, a typical example of vertical pipe is the natural circulating flow in the chimney region of Boiling Water Reactor (BWR). The correct design and operation of these devices can be managed with the proper prediction of the flow patterns and flow properties at the operating conditions of interest.

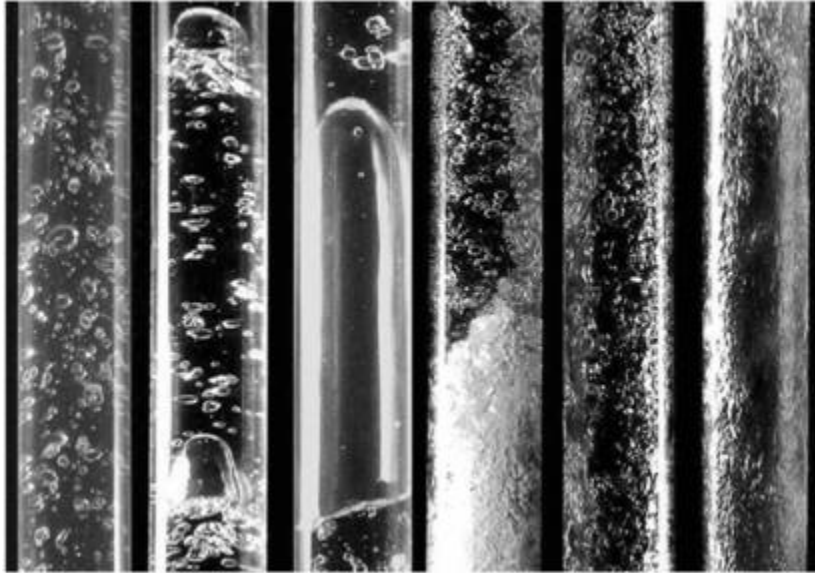


Figure 1.1. Air-Water two phase flow in vertical pipe with different flow patterns [1]

Many researchers have investigated the flow pattern in straight tubes with different diameters [1], [2], [3], [4] and [5]. Banasiak et al. [6] studied two-phase flow regime identification by means of a 3D electronic capacitance tomography (ECT) and fuzzy-logic classification. They studied two-phase gas-liquid mixtures flow pattern identification using combination of fuzzy logic and volumetric 3D ECT images. Mesquita et al. [7] used fuzzy inference on image analysis to determine two-phase flow patterns. A fuzzy classification system for two-phase flow instability patterns was developed and the flow pattern was classified based on the obtained experimental images. They also optimized the fuzzy inference to use single gray scale profiles and concluded that good results could be obtained if enough image acquisition parameters were used.

In general the flow pattern identification is done either by visual observation or by using flow pattern maps [8], [9] and [10]; but sometimes the visualization method cannot be used and other techniques like nuclear radiation attenuation, impedance electrical technique are exploited. Zeguai et al. [11] studied the flow pattern of a two-phase laminar flow in a horizontal tube. They proposed flow maps and performed some pattern rearrangements. Pietrzak [12] studied two-phase liquid-liquid flow in a pipe bend. A flow map was proposed based on the experimental results. Zhao et al. [13] studied the flow pattern of two-phase flow in a vertical pipe experimentally. A new method was proposed to study the flow patterns and good agreement was observed between the experimental results and their model.

A growing number of studies have been carried out with the use of fuzzy-neural networks to recognize flow pattern which are used in many industries like petroleum, energy and so on [14], [15], [16], [17], [18], [19], [20], [21], [22] and [23]. Gao et al. [24] carried out gas-liquid two phase flow experiments in a small diameter pipe for measuring local flow information from different flow patterns. They proposed a modality transition-based network for mapping the experimental multivariate measurements into a directed weighted complex network. They developed a new distributed conductance sensor for measuring local flow signals at different positions and then proposed a novel approach based on multi-frequency complex network to uncover the flow structures from experimental multivariate measurements [25]. They demonstrated how to derive multi-frequency complex network from multivariate time series based on the Fast Fourier transform. Zhang et al. [26] developed a numerical method based on a two-phase level set with the global mass correction and immersed boundary method to simulate wave

interaction with a semi-submerged chamber. The flow field, free surface and pressure distribution were presented at different instants in time to reveal the energy loss clearly. Many investigations about flow regime recognition based on experimental and numerical results have been carried out. These methods are mostly time-consuming effortful and subjective. The objective of this study is to propose an automatic and intelligent system to recognize the flow regime based on fuzzy logic and genetic algorithm. This intelligent controller system is simple and more accurate comparing other methods for two phase flow pattern recognition. Fuzzy controllers are very simple conceptually. They consist of an input stage, a processing stage, and an output stage. The input stage maps sensor or other inputs, such as switches, thumbwheels, and so on, to the appropriate membership functions and truth values. The processing stage invokes each appropriate rule and generates a result for each, then combines the results of the rules. Finally, the output stage converts the combined result back into a specific control output value. Fuzzy rules are linguistic IF-THEN- constructions that have the general form "IF A THEN B" where A and B are (collections of) propositions containing linguistic variables. A is called the premise and B is the consequence of the rule. In effect, the use of linguistic variables and fuzzy IF-THEN- rules exploits the tolerance for imprecision and uncertainty.

Besides the investigation of air-water two phase flow in vertical pipes, the vapor-liquid two phase flow in the pulsating heat pipes has been investigated in the present study.

Thermal management is quickly becoming a limiting factor for the advancement in many fields. Electronics are rapidly decreasing in size while simultaneously increasing in power, resulting in high power densities with limited space to dissipate the heat [27]. Even

at larger scales, power density has become a major challenge. The latest push for a rapid fire electromagnetic rail gun launcher has brought forth a plethora of issues, many of which are due to the extreme thermal loads from both the inductance heating of the rail as well as armature to rail contact heating [28]. Developing a miniature, low cost and high efficient heat transfer device is becoming more and more important due to the rapid development of electronics and computer industries. The conventional heat pipes such as copper grooved heat pipes and sintered particle heat pipes have played an important role in the heat dissipation in the laptop computers. Starting in 2004, more than 100 million desktop computers sold annually could potentially use the heat pipe technology. Today, many computer manufacturers are employing heat pipe thermal solutions in their desktop, notebook and server computers, which have opened a greater market to the heat pipe with a greater demand. With the continuous increase of power density in the electronic equipment and computers, it requires that the thermal engineers or researchers develop the advanced heat pipe technology or other innovative cooling technologies.

Akachi [29] presented a novel concept of heat and mass transfer device named as pulsating heat pipe. Owing to its potential heat transport capability, simple structure and low cost of construction, a lot of researchers have investigated it experimentally and theoretically. The heat pipe is filled with a working fluid to form vapor bubbles and liquid plugs (a liquid-vapor mixture) dependent on the filled ratio. When the heat pipe is in operation, the saturated pressure of the liquid-vapor mixture varies from the evaporator section, adiabatic section to condenser section depending on the operating temperature. Obviously, when the evaporator section is heated, the vapor pressure at this end increases. And liquid at this end is superheated before vaporization takes place at the wall surface.

Once the vapor bubble is formed in the superheated liquid, its growth rate is very rapid especially in a small limited space. This explosive formation of vapor is often a source of instability since it is accompanied by a sharp local increase in static pressure which may reduce, stop, or even reverse the flow in the upstream section of the channel. At another cooling end of the heat pipe, when the vapor bubbles are cooled, the bubbles collapse and the condensing liquid film is formed inside the channel. The temperature of the vapor-liquid mixture is determined by the cooling surface area, wall temperature and heat transfer coefficient in the condenser section. The pressure in the condenser is dependent on the temperature of the vapor-liquid mixture. If liquid in the condenser section is cooled further, a subcooled liquid will appear in this area. Once the vapor bubbles and liquid plugs travel to the adiabatic section, where no heat addition or rejection occurs, a mass-spring model may be used to describe the oscillating motions of vapor bubbles and liquid slugs inside this section. When the liquid-vapor mixture of working fluid flows through the evaporator and condenser repeatedly, an enhanced heat/mass transfer process occurs due to the phase-change heat transfer and forced convection.

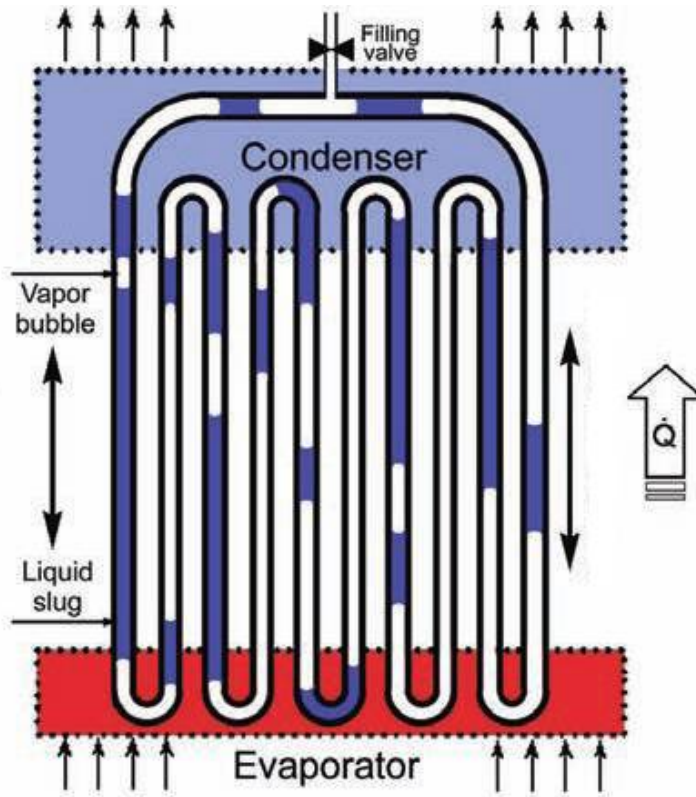


Figure 1.2. Schematic closed loop pulsating heat pipe [30]

A typical oscillating heat pipe is illustrated in Figure 1.2. As heat is added to the evaporating section, vaporization occurs. When heat is removed from the condensing section, the vapor condensation takes place. The volume expansion due to the liquid vaporization and contraction due to the vapor condensation cause an oscillating motion of the liquid slugs and vapor bubbles delivering vapor to the condenser and returning liquid to the evaporator [30-35]. The oscillatory motion of liquid slugs and vapor bubbles is self-

sustaining as long as heating and cooling conditions are maintained. These statements provide a very general description of mechanisms of oscillating heat pipe.

The pipe is first evacuated and then filled partially with a working fluid. If the diameters of Close Loop Pulsating heat pipe is not too large, the fluid distributes itself into an arrangement of liquid slugs separated by vapor bubbles. One end of this tube bundle receives heat transferring it to the other end by a pulsating action of the liquid–vapor/slug-bubble system. The liquid and vapor slug/bubble transport is caused by the thermally induced pressure pulsations inside the device and no external mechanical power is required. The type of fluid and the operating pressure inside the pulsating heat pipe depend on the operating temperature of the heat pipe. The region between evaporator and condenser is adiabatic. The heat is transfer from evaporator to condenser by the means of pulsating action of vapor slug and liquid slug. This pulsation appears as a non-equilibrium chaotic process, whose continuous operation requires non-equilibrium conditions inside the tube in some of the parallel channels. For Close Loop Pulsating heat pipes (CLPHPs), no external power source is needed to either initiate or sustain the fluid motion or the transfer of heat. The purpose of this project is to understand how CLPHPs operate and to be able to understand how various parameters (geometry, fill ratio, materials, working fluid, etc.) affect its performance. Understanding its operation is further complicated by the non-equilibrium nature of the evaporation and condensation process, bubble growth and collapse and the coupled response of the multiphase fluid dynamics among the different channels.

Although a variety of designs are in use, understanding of the fundamental processes and parameters affecting the PHP operation still need more investigation. Various experimental and theoretical investigations are being carried out to achieve this task. Shafii et al. [36, 37] presented analytical models for both open and closed-loop pulsating heat pipes with multiple liquid slugs and vapor plugs. They performed an explicit finite difference scheme for solving the governing equations to predict the behavior of vapor plugs and liquid slugs. Zhang and Faghri [38, 39] investigated heat transfer process in evaporator and condenser sections of the PHP. They studied frequency and amplitude behavior of the oscillations versus surface tension, diameter and wall temperature of the heating section. In addition, they reviewed and released advances and unsolved issues on the mechanism of PHP operation, modeling, and application [40].

Shao and Zhang [41] studied thermally-induced oscillatory flow and heat transfer in a U-shaped minichannel. Effects of axial variation of surface temperature on sensible heat transfer between the liquid slug and the minichannel wall, as well as initial temperature and pressure loss at the bend on the heat transfer performance were investigated. Kim et al. [42] analyzed entropy generation for a pulsating heat pipe. They also studied the effects of fluctuations of heating and cooling section temperatures on performance of a PHP [43]. The fluctuations of wall temperatures included a periodic component and a random component. The periodic component was characterized by the amplitude and frequency, while the random component was described by the standard deviations. Ma et al. [44] used a mathematical model predicting the oscillating motion in an oscillating heat pipe. The model considered the vapor bubble as the gas spring for the

oscillating motions including effects of operating temperature, nonlinear vapor bulk modulus, and temperature difference between the evaporator and the condenser.

Tong et al. [45] applied flow visualization technic for the closed-loop pulsating heat pipe (PHP) using a charge coupled device (CCD). It was observed that during the start-up period, the working fluid oscillated with large amplitude, however, at steady operating state, the working fluid circulated. Borgmeyer and Ma [46] conducted an experimental investigation to evaluate the motion of vapor bubbles and liquid plugs within a flat-plate pulsating heat pipe to determine the effects of working fluids, power input, filling ratio, and angle of orientation on the pulsating fluid flow. Qu et al. [47] performed an experimental study on the thermal performance of an oscillating heat pipe (OHP) charged with water and spherical Al₂O₃ particles of 56 nm in diameter. The effects of filling ratios, mass fractions of alumina particles, and power inputs on the total thermal resistance of the OHP were investigated. Dobson and Harms [48] analyzed lumped parameter of closed and open oscillatory heat pipe. Khandekar et al. [49, 50] reported an experimental study to understand operational regimes of closed loop pulsating heat pipes.

Recently there have been experimental studies which proposed the existence of chaos in PHPs under some operating conditions. The approach in these studies is to analyze the time series of fluctuation of temperature of a specified location on the PHP tube wall (adiabatic section) by power spectrum calculated through FFT. The two dimensional mapping of the strange attractor and the subsequent calculation of the Lyapunov exponent have been done to prove the existence of chaos in PHP system [51]. Dobson [52, 53] theoretically and experimentally investigated an open oscillatory heat pipe

including gravity. The theoretical model used vapor bubble, liquid plug and liquid film control volumes. Experimental model was constructed and tested using water as the working fluid. By calculating Lyapunov exponents it was shown that the theoretical model is able to reflect the characteristic chaotic behavior of experimental devices. Xiao-Ping and Cui [54] studied the dynamic properties for the micro-channel phase change heat transfer system by theoretical method combined with experiment. Liquid–vapor interface dynamic systems were obtained by introducing disjoining pressure produced by three phase molecular interactions and Lie algebra analysis. Experiments for a 0.6mm×2mm rectangular micro-channel were carried out to obtain the pressure time serials. Power spectrum density analysis for these serials showed that the system is in chaotic state if the frequency is above 7.39 Hz.

Song and Xu [55] have run series of experiments to explore chaotic behavior of PHPs. Different number of turns, inclination angles, filling ratios and heating powers were tested. Their study confirmed that PHPs are deterministic chaotic systems. Louisos et al. [56] conducted numerical study of chaotic flow in a 2D natural convection loop with heat flux boundaries. System of governing equations was solved using a finite volume method. Numerical simulations were performed for varying levels of heat flux and varying strengths of gravity to yield Rayleigh numbers ranging from 1.5×10^2 to 2.8×10^7 . Ridouane et al. [57] computationally explored the chaotic flow in a 2D natural convection loop. They set constant temperatures for the boundary conditions in heating and cooling sections. Numerical simulations were applied for water corresponding to $Pr = 5.83$ and Rayleigh number varying from 1000 to 150,000. Results in terms of streamlines, isotherms, and local heat flux distributions along the walls were presented for each flow

regime. Louissos et al. [58] numerically investigated chaotic natural convection in a toroidal thermosyphon with heat flux boundaries. Nonlinear dynamics of unstable convection in a 3D toroidal shaped thermal convection loop was studied. The lower half of the thermosyphon was subjected to a positive heat flux into the system while the upper half was cooled by an equal-but-opposite heat flux out of the system. Delineation of multiple convective flow regimes was achieved through evolution of the bulk-mass-flow time-series and the trajectory of the mass flow attractor.

Although several theoretical and experimental studies have investigated the chaotic behavior of pulsating heat pipes, there has been no detailed numerical simulation for PHPs. Then such a numerical simulation can lead to a better perception and understanding of the process and behavior of PHPs. The objective of this study is to numerically investigate chaotic behavior of flow in a two and three dimensional closed-loop pulsating heat pipe. Constant temperature and heat flux boundary conditions have been used for heating and constant temperature for cooling sections. Water and ethanol were employed as working fluids. Volume of Fluid (VOF) method has been applied for two phase flow simulation. Effects of variation in evaporator temperature and heating power, condenser temperature and filling ratio on chaotic behavior of the pulsating heat pipe will be studied.

Chapter 2

Two phase flow pattern identification and fuzzy logic

Fuzzy logic control is a range-to-point or range-to-range control. The output of a fuzzy controller is derived from fuzzifications of both inputs and outputs using the associated membership functions. A crisp input will be converted to the different members of the associated membership functions based on its value. From this point of view, the output of a fuzzy logic controller is based on its memberships of the different membership functions, which can be considered as a range of inputs [22]. To implement fuzzy logic technique to a real application requires the following three steps:

1- Fuzzification – convert classical data or crisp data into fuzzy data or Membership Functions (MFs)

2- Fuzzy Inference Process – combine membership functions with the control rules to derive the fuzzy output

3- Defuzzification – use different methods to calculate each associated output and put them into a table: the lookup table. Pick up the output from the lookup table based on the current input during an application

For instance, to control an air conditioner system, the input temperature and the output control variables must be converted to the associated linguistic variables such as 'HIGH', 'MEDIUM', 'LOW' and 'FAST', 'MEDIUM' or 'SLOW'. The former is corresponding to the input temperature and the latter is associated with the rotation speed of the operating motor. Besides those conversions, both the input and the output must also be converted from crisp data to fuzzy data. All of these jobs are performed by the first step – fuzzification. In the second step, to begin the fuzzy inference process, one needs to combine the Membership Functions with the control rules to derive the control output, and arrange those outputs into a table called the lookup table. The control rule is the core of the fuzzy inference process, and those rules are directly related to a human being's intuition and feeling. For example, still in the air conditioner control system, if the temperature is too high, the heater should be turned off, or the heat driving motor should be slowed down, which is a human being's intuition or common sense. Finally, different methods are utilized to calculate the associated control output.

In this respect, fuzzy logic mimics the crucial ability of the human mind to summarize data and focus on decision-relevant information. Present study explains how accurate and useful this method can be applied for Gas-Liquid two phase flow pattern recognition.

2.1 Geometry configuration

The two phase water-air mixture flows in a 5-cm diameter and 1-m long vertical pipe. Air and water are mixed in the entrance of the pipe. The grid mesh is depicted in Figure 2.1. There are three inlets for air and three inlets for water (see Figure 2.2). This inlet configuration allows setting a structured mesh for the simulation and water-gas system that can be mixed very well. It is important to set water near the wall. Otherwise air may stick to the wall and this leads to an unstable solution. It should be noted that the entire void fraction figures in this study represent the middle cross sectional area of the 3D pipe.

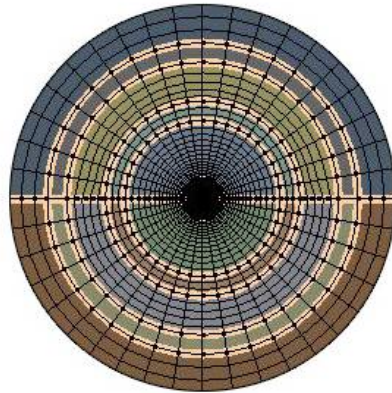


Figure 2.1. Grid mesh used in the study (not in scale)

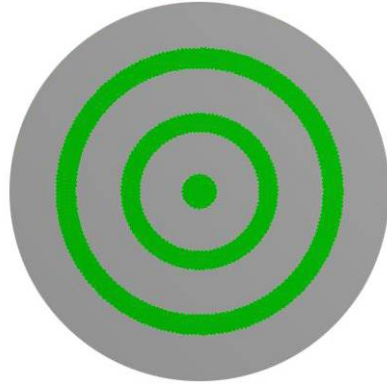


Figure 2.2. Three air and three water inlets (the green color shows the air inlets)

Different area ratios (water area to total area and air area to total area) are considered, i.e. $7/8$ and $1/8$, $3/4$ and $1/4$ and finally $1/2$ and $1/2$ for water and air, respectively. These different ratios are considered and water and air superficial velocity are 0.375 m/s and 0.5 m/s, respectively. The results indicate that as the ratio of air approaches to water ratio, the computational time for solution of the problem decreases; since as the area of the air increases, to keep superficial inlet velocity constant, the fluid velocity decreases which leads to a lesser courant number with larger time steps. Besides, the contours demonstrate that there are great differences between flow patterns. It was found that the ratio of 0.25 for air and 0.75 for water gives better results.

2.2 Governing Equation

Two approaches, the volume of fluid (VOF) and Eulerian model, will be used for the numerical simulation of gas-liquid two phase flow. The VOF model is applicable for modeling of two or more immiscible fluids by solving a single set of momentum equations and tracking the volume fraction of each of the fluids throughout the domain. Prediction of motion of large bubbles in a liquid and the steady or transient tracking of any gas-liquid interface are the main applications of VOF. The VOF formulation depends on the fact that two or more fluids (or phases) are not interpenetrating. In the computational cell of each control volume for each additional phase is added to the model, the volume fraction of the phase is introduced. The volume fractions of all phases sum to unity. Volume-averaged values represent that the fields for all variables and properties are shared by the phases as long as the volume fraction of each phase is known at each location. Therefore, the variables and properties in any given cell by considering the volume fraction values can either purely represent one of the phases or a mixture of the phases. The appropriate properties and variables will be assigned to each control volume within the domain by considering the local value of volume fractions.

The Eulerian model is used to model droplets or bubbles of secondary phase or phases dispersed in continuous fluid phase (primary phase) [59]. For each phase, the Eulerian modeling system is based on ensemble-averaged mass and momentum transport equations. Eulerian model solves momentum, enthalpy, and continuity equations for each phase and tracks volume fractions. It uses a single pressure field for all phases and allows for virtual mass effect and lift forces. Multiple species and homogeneous reactions are in

each phase and allows for heat and mass transfer between phases. In the present study, both models were examined and the VOF model was used for further investigation. The continuity equations for both Eulerian and VOF models are the same.

2.2.1 Continuity equation

The continuity for the q^{th} phase is expressed as the following form:

$$\frac{1}{\rho_q} \left[\frac{\partial(\alpha_q \rho_q)}{\partial t} + \nabla \cdot (\alpha_q \rho_q \mathbf{v}_q) \right] = \sum_{p=1}^n (\dot{m}_{pq} - \dot{m}_{qp}) + S \quad (2.1)$$

where α_q , \mathbf{v}_q and ρ_q are the void fraction, velocity and density of phase q , respectively. It is assumed that mass transfer between air and water is zero ($\dot{m}_{pq} = \dot{m}_{qp} = 0$), and the source term on the right-hand side of Equation (1), S , is zero. Then for the water-air two phase system ($n=2$) the right hand side of Equation (1) becomes zero. The volume fraction equation will not be solved for the primary phase and the primary-phase volume fraction will be calculated based on the following constraint:

$$\sum_{q=1}^n \alpha_q = 1 \quad (2.2)$$

2.2.2 Momentum equation for VOF model

A single momentum equation is solved throughout the domain, and then the computed velocity field is shared among the phases. The momentum equation, which relies on the volume fractions of all phases, is:

$$\frac{\partial}{\partial t} (\rho \mathbf{v}) + \nabla \cdot (\rho \mathbf{v} \mathbf{v}) = -\nabla p + \nabla \cdot [\mu (\nabla \mathbf{v} + \nabla \mathbf{v}^T)] + \rho \mathbf{g} + \mathbf{F} \quad (2.3)$$

The surface tension can be expressed in terms of the pressure jump across the surface. The force at the surface can be defined as a volume force using the divergence theorem. The simplified equation of the volume force that is the source term which is added to the momentum equation is shown below:

$$F_{st} = \sigma_{ij} \frac{\rho k_i \nabla \alpha_i}{\frac{1}{2}(\rho_i + \rho_j)} \quad (2.4)$$

where the properties μ is viscosity and ρ is the volume averaged density defined as below.

$$\alpha_G \rho_G + \alpha_L \rho_L = \rho \quad (2.5)$$

The curvature, K , is expressed in terms of the divergence of the unit normal, \mathbf{n} and calculated from local gradients in the surface normal at the interface.

$$K = \nabla \cdot \mathbf{n} = \frac{1}{|n|} \left[\left(\frac{n}{|n|} \cdot \nabla \right) |n| - (\nabla \cdot n) \right] \quad (2.6)$$

$$\mathbf{n} = \frac{n}{|n|} \quad (2.7)$$

where n is the surface normal and is defined as the gradient of α_q , the volume fraction of the q^{th} phase.

$$n = \nabla \alpha_q \quad (2.8)$$

2.2.3 Turbulence model

Four different turbulence models, k - ε RNG, k - ε standard, Reynolds stress and k - ε realizable model were examined. As it will be evidenced later, the k - ε RNG model leads to a more stable and accurate results and therefore it was used for further investigations. The governing equations for the turbulent kinetic energy k and turbulent dissipation ε are presented below:

$$\frac{\partial}{\partial t} (\rho k) + \frac{\partial}{\partial x_i} (\rho k u_i) = \frac{\partial}{\partial x_i} \left[\left(\mu + \frac{\mu_t}{\sigma_k} \right) \frac{\partial k}{\partial x_i} \right] + G_k - \rho \varepsilon \quad (2.9)$$

$$\frac{\partial}{\partial t} (\rho \varepsilon) + \frac{\partial}{\partial x_i} (\rho \varepsilon u_i) = \frac{\partial}{\partial x_j} \left[\left(\mu + \frac{\mu_t}{\sigma_\varepsilon} \right) \frac{\partial \varepsilon}{\partial x_j} \right] + G_{1\varepsilon} \frac{\varepsilon}{k} G_k - C_{2\varepsilon} * \rho \frac{\varepsilon^2}{k} \quad (2.10)$$

The terms $C_{2\varepsilon}^*$ and η equal to:

$$C_{2\varepsilon}^* = C_{2\varepsilon} + \frac{C_\mu \eta^3 \left(1 - \frac{\eta}{\eta_0} \right)}{1 + \beta \eta^3} \quad (2.11)$$

$$\eta = \frac{SK}{\varepsilon} \quad (2.12)$$

S is strain rate tensor which is defined as:

$$S = \frac{1}{2} \left(\frac{\partial u_j}{\partial x_i} + \frac{\partial u_i}{\partial x_j} \right) \quad (2.13)$$

The turbulence viscosity of this model is given below:

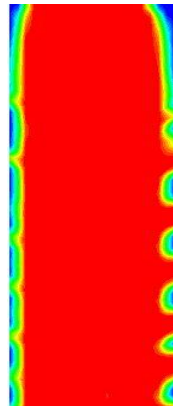
$$C_\mu = 0.0845 \quad C_{1\varepsilon} = 1.42 \quad \eta_o = 4.38$$

$$\sigma_k = 0.7194 \quad \sigma_\varepsilon = 0.7149 \quad \beta = 0.012$$

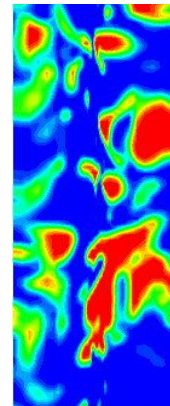
2.3 Results and Discussions

2.3.1 Turbulence modeling and grid independence test

In this part, the results of different turbulence modeling are compared and the best model will be chosen to continue the simulation. To this aim, slug and annular flow patterns are investigated using different turbulence models. Figures 2.3 to 2.6 show the void fraction results for these turbulence modeling. For the $K-\varepsilon$ Standard model it is evident that the slug flow has been simulated well. But for the annular flow, it can be seen that air has been stuck to the wall that signifies an inappropriate solution.



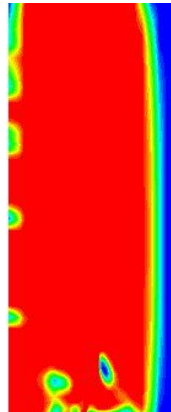
Annular flow pattern



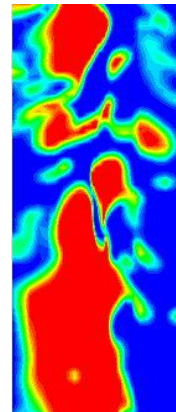
Slug flow pattern

Figure 2.3. $K-\varepsilon$ Standard turbulence modeling

The $K-\varepsilon$ realizable model even gives better result comparing the $K-\varepsilon$ Standard for the slug flow pattern. It is obvious that this model does not predict well the annular flow like the $K-\varepsilon$ Standard. Besides the inaccuracy in solution for the annular flow, the simulation time for this model increases due to the higher turbulence viscosity and courant number.



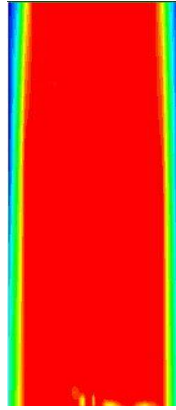
Annular flow pattern



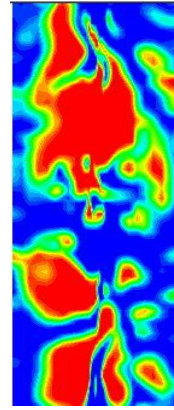
Slug flow pattern

Figure 2.4. $K-\varepsilon$ realizable turbulence modeling

It can be seen that the $K-\varepsilon$ RNG for turbulence modeling predicts both annular and slug flow patterns very well. The near-wall liquid film and the gas core in the annular flow look perfect. Times step for this simulation is 0.0001 s and courant number is less than one.



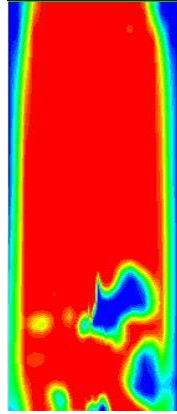
Annular flow pattern



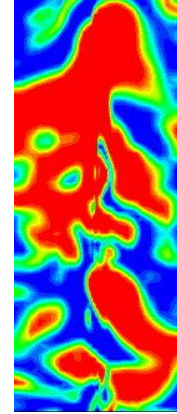
ow patternSlug fl

Figure 2.5. $K-\epsilon$ RNG turbulence modeling

The Reynolds stress model gives good result for both annular and slug flow patterns. But at some parts air has been stuck to the wall in the slug flow. Considering time step of 0.0001 s for transient process, the Reynolds stress takes more time than the $K-\epsilon$ RNG model.



Annular flow pattern



Slug flow pattern

Figure 2.6. Reynolds stress turbulence modeling

By comparing all mentioned models, it can be concluded that the $K-\varepsilon$ RNG is better for turbulence modeling to simulate the two phase flow of water-air in a vertical pipe in terms of accuracy and computational time. So, $K-\varepsilon$ RNG will be considered as turbulence modeling to continue the simulation afterwards.

In order to investigate grid independency of the problem, eight different grids were considered. Figure 2.7 shows the pressure drop in the pipe versus number of meshes. It is obvious that grid with 300,000 meshes is suitable for further investigations.

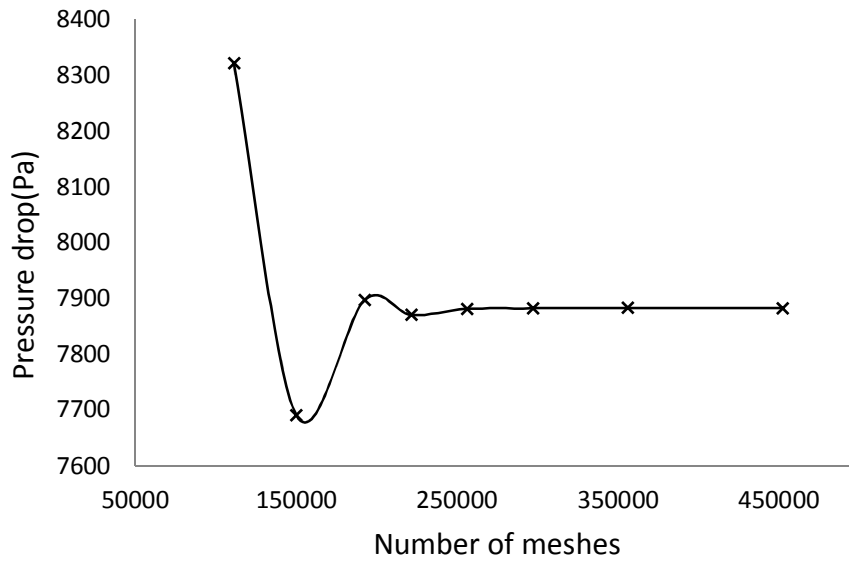
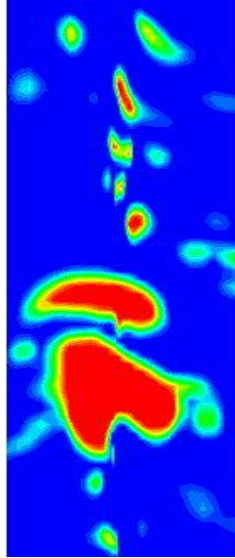


Figure 2.7. Grid independency investigation

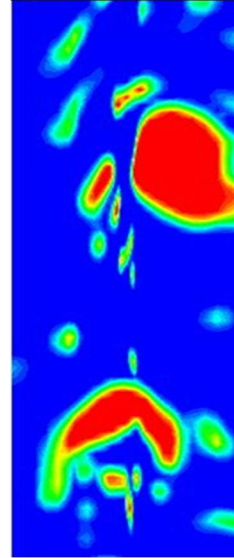
2.3.2 Flow patterns simulation

Hewitt map for two phase flow pattern in a vertical pipe is based on both phases' superficial velocity. Since in the present work water inlet area is three times as air inlet area, to get the superficial velocity for each phase, water inlet velocity and air inlet velocity should be multiplied by 0.25 and 0.75, respectively. Figure 2.8 shows void fraction contours for bubbly flow pattern with different water and air inlet velocities. It is obvious that bubbles are scattered widely in the pipes. It can be seen that as the ratio of water inlet velocity to air inlet velocity increases, more bubbles form and flow get closer to the bubbly pattern.



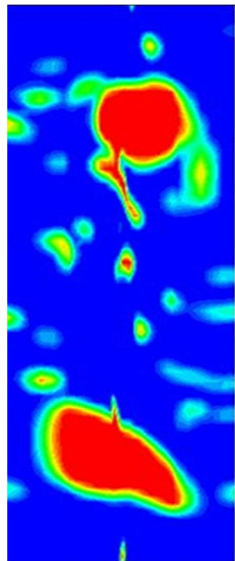
(a) Water inlet velocity 0.3 m/s

Air inlet velocity 0.4 m/s



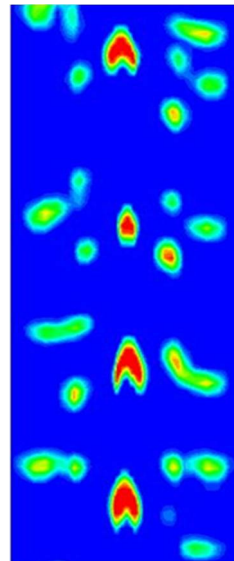
(b) Water inlet velocity 0.5 m/s

Air inlet velocity 0.5 m/s



(c) Water inlet velocity 0.2 m/s

Air inlet velocity 0.2 m/s

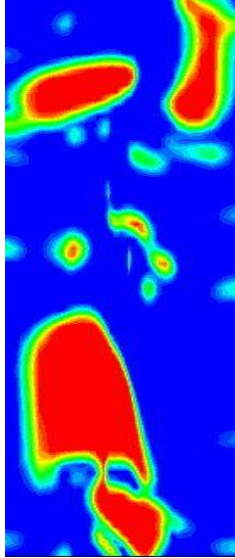


(d) Water inlet velocity 2.6 m/s

Air inlet velocity 0.8 m/s

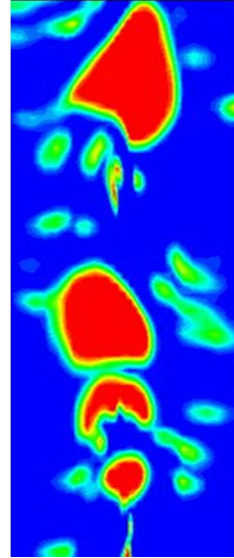
Figure 2.8. Void fraction contours for bubbly flow

Figure 2.9 shows void fraction contours for bubbly-slug flow pattern with different water and air inlet velocities. This flow pattern is like the bubbly flow but bubbles are not scattered that much in the pipes. By decreasing the ratio of water inlet velocity to air inlet velocity, less bubbles forms and flow get closer to the slug pattern.



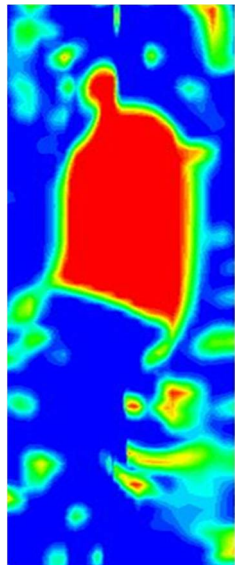
(a) Water inlet velocity 0.4 m/s

Air inlet velocity 0.8 m/s



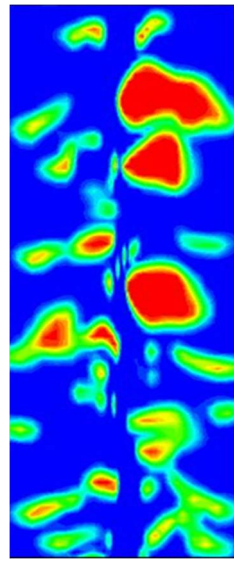
(b) Water inlet velocity 1 m/s

Air inlet velocity 1 m/s



(c) Water inlet velocity 0.133 m/s

Air inlet velocity 0.4 m/s

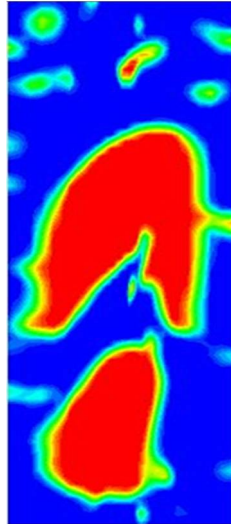


(d) Water inlet velocity 2 m/s

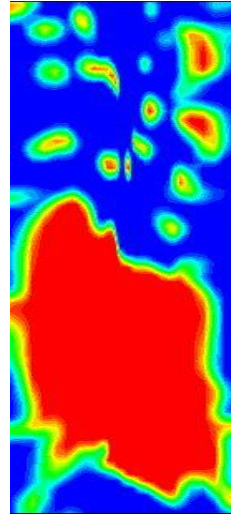
Air inlet velocity 2 m/s

Figure 2.9. Void fraction contours for bubbly- slug flow

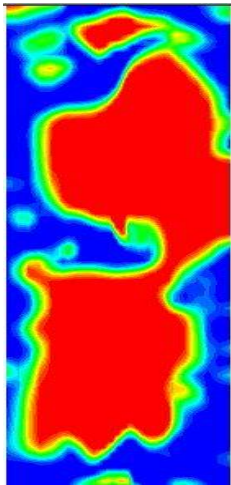
Figure 2.10 shows void fraction contours for slug flow pattern with different water and air inlet velocities. It is evidence that by increasing the ratio of air inlet velocity to water inlet velocity, the sizes of the bubbles increase and flow becomes closer to the churn pattern; by decreasing this ratio, size of the bubbles decreases and flow is closer to the bubbly pattern.



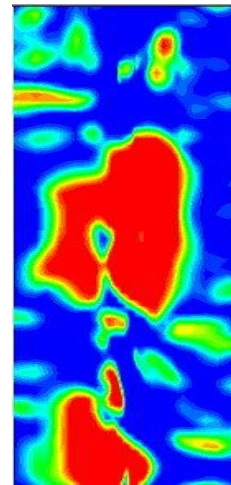
(a) Water inlet velocity 0.6 m/s
Air inlet velocity 1 m/s



(b) Water inlet velocity 0.5 m/s
Air inlet velocity 2 m/s



(c) Water inlet velocity 0.5 m/s
Air inlet velocity 3 m/s

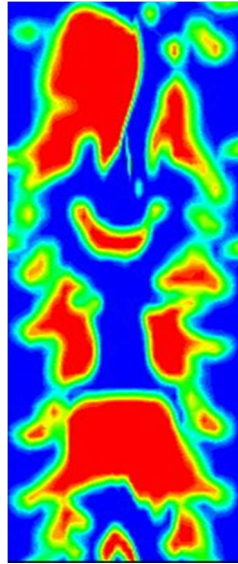


(d) Water inlet velocity 0.4 m/s
Air inlet velocity 2 m/s

Figure 2.10. Void fraction contours for slug flow

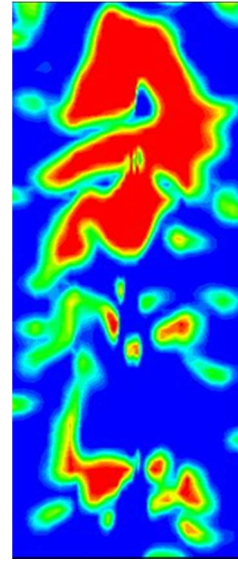
Figure 2.11 shows void fraction contours for slug-churn flow pattern with different water and air inlet velocities. Flow patterns showed the behaviors of both churn and slug

flows at air inlet velocity of 3.6 m/s. When air inlet velocity becomes 3 m/s, bubbly flow prevails which this can be verified by the Hewitt map.



(a) Water inlet velocity 2 m/s

Air inlet velocity 3.6 m/s

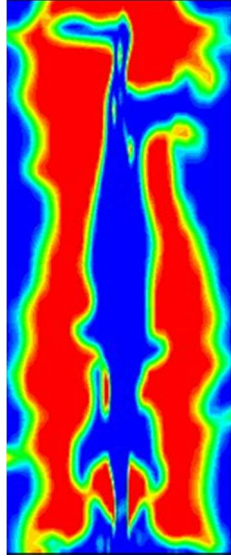


(b) Water inlet velocity 2 m/s

Air inlet velocity 3 m/s

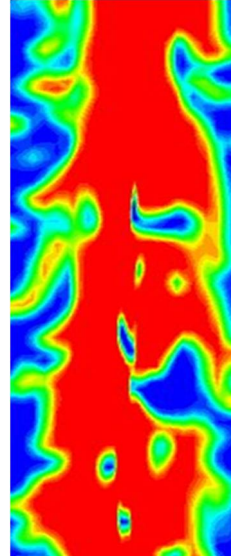
Figure 2.11. Void fraction contours for slug- churn flow

Figure 2.12 shows void fraction contours for churn flow pattern with different water and air inlet velocities. By increasing the ratio of air inlet velocity to water inlet velocity, size of the bubbles increases and flow get closer to the annular pattern. By decreasing this ratio, less bubbles form and flow get closer to the slug pattern.



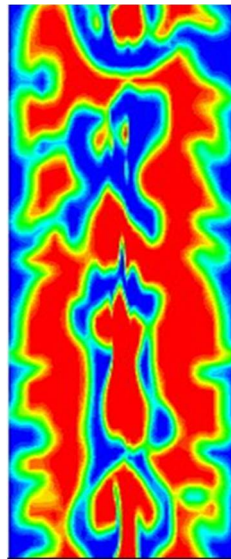
(a) Water inlet velocity 2.67 m/s

Air inlet velocity 8 m/s



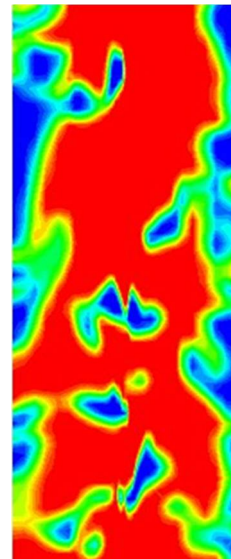
(b) Water inlet velocity 2.67 m/s

Air inlet velocity 24 m/s



(c) Water inlet velocity 5.33 m/s

Air inlet velocity 32 m/s



(d) Water inlet velocity 1 m/s

Air inlet velocity 15 m/s

Figure 2.12. Void fraction contours for churn flow

Figure 2.13 shows void fraction contours for annular flow pattern with different water and air inlet velocities. It is obvious that gas flow is continuous in the pipe and there is no particular bubble. These contours show the annular flow.

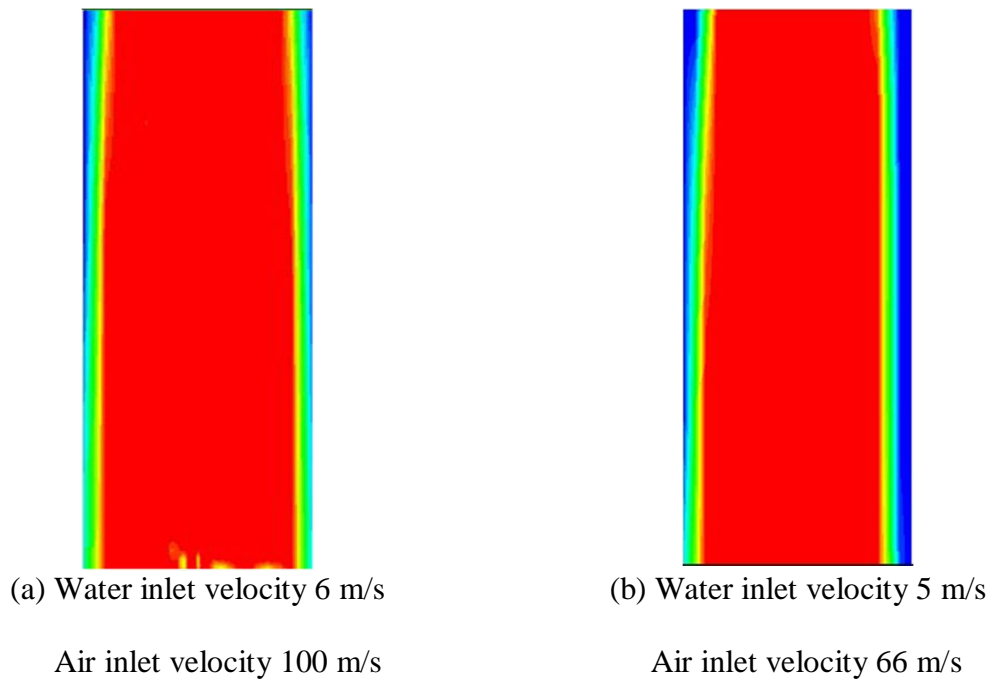


Figure 2.13. Void fraction contours for annular flow

2.3.3 Image Processing

In this part image processing is utilized to obtain results like total area of air bubbles, the largest area of air bubbles, and number of bubbles and so on. Background

subtraction (BS) method was performed for image processing. Background subtraction is a major preprocessing step in many vision based applications. The method operates entirely using 2D image measurements without requiring an explicit 3D reconstruction of the scene. Background subtraction, also known as Foreground Detection, is a technique in the fields of image processing and computer vision wherein an image's foreground is extracted for further processing. An image-subtracted algorithm was applied to reduce the background noise by subtracting the background image from each dynamic image. In order to smooth the image border, a median filter was also used. To this goal, a MATLAB code was developed to prepare each picture by some simple image processing procedures. The procedure of image processing includes converting images to RGB and then to gray scale ones and the background of images are omitted by a specific algorithm and the noises are reduced by a filter. Then, images become binary and corners of images are fixed by a series of morphological processes and the inessential holes are filled. After processing images, their characteristics are obtained and the number of bubbles or particles in the gas phase, their area and perimeter are elicited. An image processing sample is illustrated in Fig. 2.14.

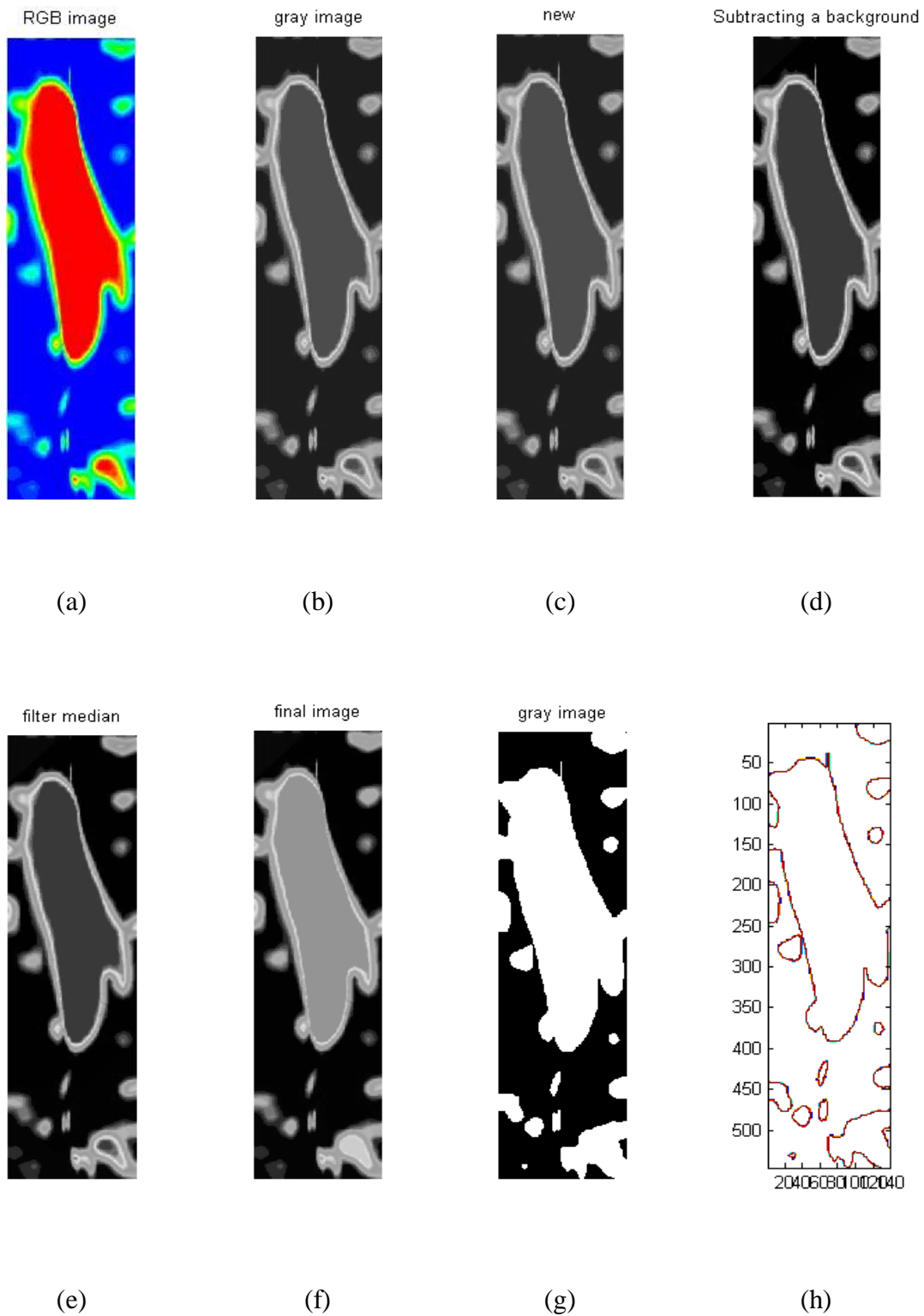


Figure 2.14. Image processing on an image obtained from simulation

Some different flow patterns are shown in Tables 2.1 and 2.2. Table 2.1 shows that by decreasing the inlet water velocity and increasing the inlet air velocity, the flow pattern goes from bubbly flow to slug flow and more bubbles stick together. Then, image processing will result in lower number of bubbles with greater areas. It can be seen that the number of bubbles in bubbly flow pattern changes from 19 and 21 to 11 in slug flow pattern and the area of the biggest bubble changes from 1000 to 30000 when the flow pattern goes from bubbly to slug.

Table 2.1. Results obtained from image processing for bubbly and slug flow patterns

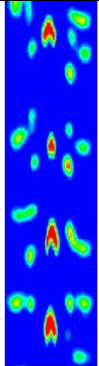
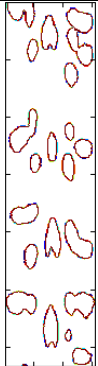
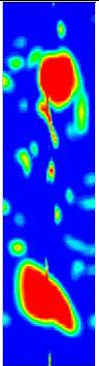
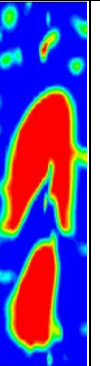
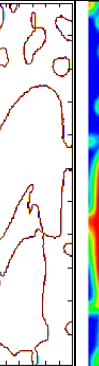
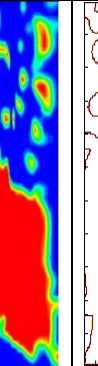
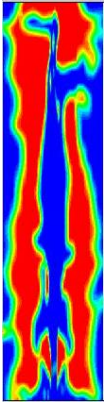
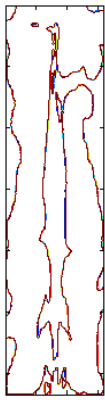
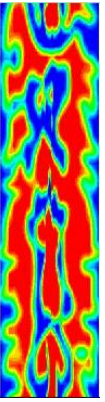
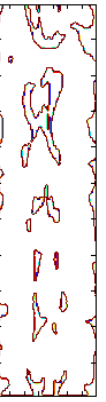
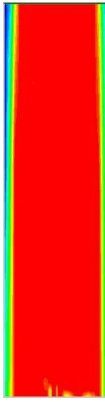
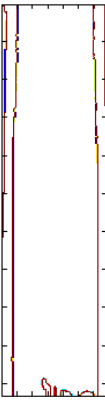
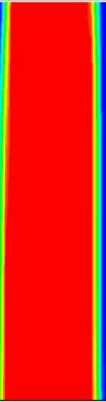
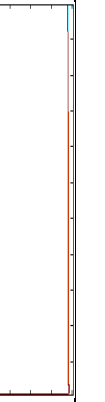
Contour of void fraction of phases before and after image processing								
Water superficial velocity(m/s)	2	0.15	0.45	0.375				
Air superficial velocity(m/s)	0.2	0.075	0.25	0.5				
Flow pattern based on Hewitt map	Bubbly	Bubbly	Slug	Slug				
Number of bubbles	21	19	11	11				
Area of the largest bubble(pixel)	2667	10078	33173	36993				
Number of large bubbles	19	2	2	2				
Average area of bubbles(pixel)	1021.9	1344.2	3513.2	3584.3				
Bubble area to total area	0.2119	0.3383	0.5092	0.6648				

Table 2.2 shows that by decreasing the inlet water velocity and increasing the inlet air velocity, the flow pattern changes from churn to annular. Comparing Tables 2.1 and 2.2 indicates that this behavior applies from slug to churn flow pattern. It is evident that by changing the flow pattern from slug to churn and from churn to annular, the number of

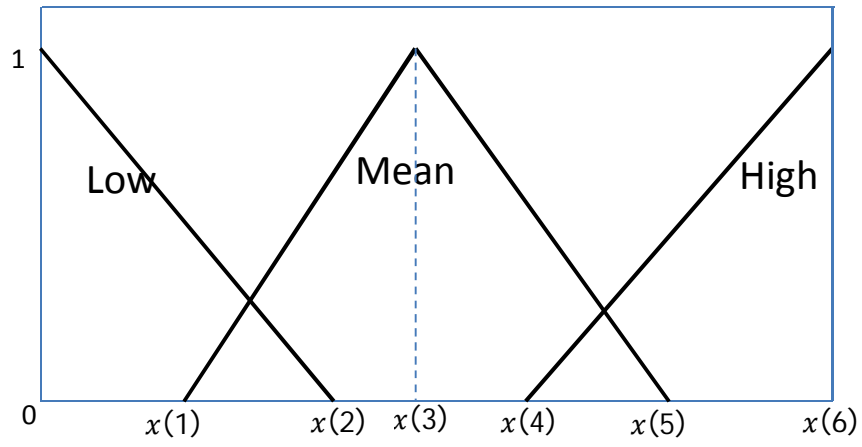
bubbles decreases and their area increases. So, it can be concluded that by increasing the air velocity and decreasing the water velocity, less number of bubbles will form with greater areas.

Table 2.2. Results obtained from image processing for churn and annular flow pattern

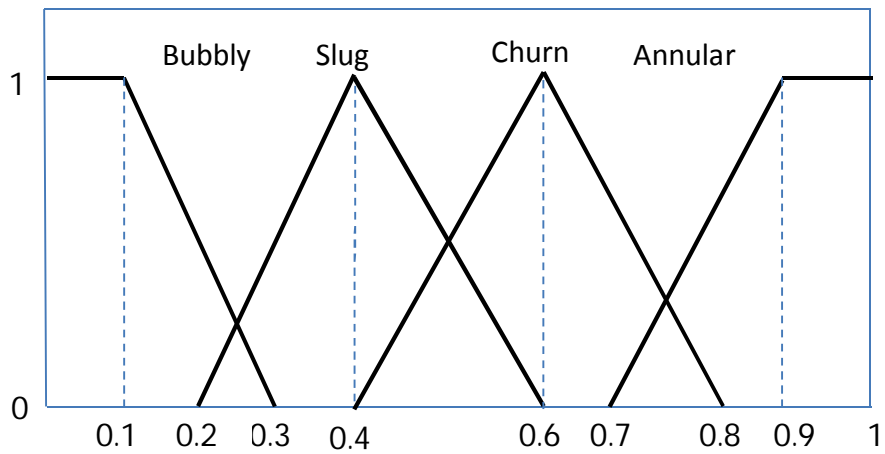
Contour of void fraction of phases before and after image processing								
Water superficial velocity(m/s)	2	4	4	3.75				
Air superficial velocity(m/s)	2	8	25	16.5				
Flow pattern based on Hewitt map	Churn	Churn	Annular	Annular				
Number of bubbles	6	3	1	1				
Area of the largest bubble(pixel)	54943	64955	70153	69352				
Number of large bubbles	1	1	1	1				
Average area of bubbles(pixel)	9186	21672	70153	69352				
Bubble area to total area	0.7243	0.8367	0.9268	0.9187				

2.3.4 Fuzzy Logic and Genetic Algorithm

Fuzzy logic was used in this study to identify of two-phase water-air flow patterns. Fuzzy logic has two different meanings. In a narrow sense, fuzzy logic is a logical system, which is an extension of multi value logic. However, in a wider sense fuzzy logic is almost synonymous with the theory of fuzzy sets, a theory which relates to classes of objects with non-distinct boundaries in which membership is a matter of degree. Even in its more narrow definition, fuzzy logic differs both in concept and substance from traditional multivalued logic systems. One of the most important and basic concepts underlying fuzzy logic (FL) is linguistic variable, that is, a variable whose values are words rather than numbers. In fact, much of FL may be viewed as a methodology for computing with words rather than numbers. Although words are inherently less precise than numbers, their use is closer to human intuition and cheaper. So in the cases that precision is the first priority, it is not logical to use words variables for computing. Genetic algorithm optimizes the results and it actually finds the best result by probing in the given range.



(a)



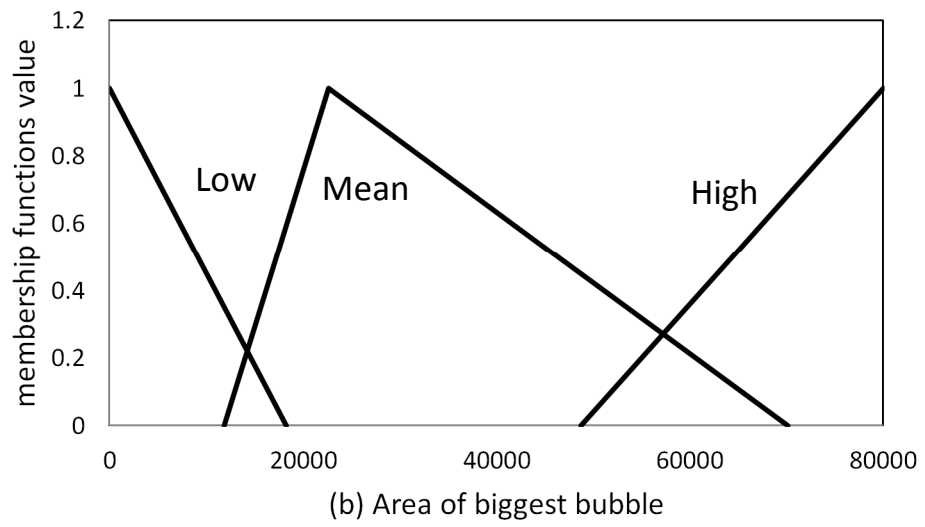
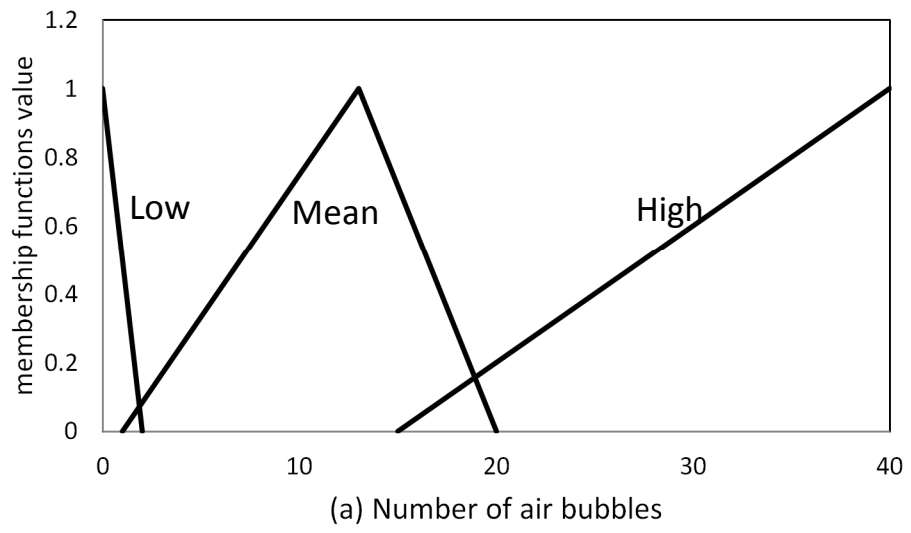
(b)

Figure 2.15. Input (a) and Output (b) membership functions

Regarding to the obtained results of image processing, it can be concluded that four inputs, i.e. number of air bubbles, area of biggest bubble, average area of bubbles and ratio of bubble area to total area as well as three triangular membership function of low, mean and high for each input are considered (see Fig. 2.15a). Now genetic algorithm should find $x(1)$ to $x(6)$ for each input, i.e., 24 unknowns for four inputs.

Since fuzzy logic should recognize flow pattern and the possibility of four flow patterns, i.e. churn, annular, slug and bubbly are the same, therefore their fuzzy functions are specified and divided equally for four flow patterns (see Fig. 2.15b). Similar to input membership functions, fuzzy logics should be obtained through optimization with genetic algorithm. To this aim, at least four rules should be considered. In this way the fuzzy set can determine all four flow patterns. These rules of fuzzy logic are summarized as follows:

- **R1:** If number of bubbles is $x(1)$ and biggest area of bubbles is $x(2)$ and bubbles mean area is $x(3)$ and void fraction is $x(4)$ then the flow pattern is $x(5)$.
- **R2:** If number of bubbles is $x(6)$ and biggest area of bubbles is $x(7)$ and bubbles mean area is $x(8)$ and void fraction is $x(9)$ then the flow pattern is $x(10)$.
- **R3:** If number of bubbles is $x(11)$ and biggest area of bubbles is $x(12)$ and bubbles mean area is $x(13)$ and void fraction is $x(14)$ then the flow pattern is $x(15)$.
- **R4:** If number of bubbles is $x(16)$ and biggest area of bubbles is $x(17)$ and bubbles mean area is $x(18)$ and void fraction is $x(19)$ then the flow pattern is $x(20)$.



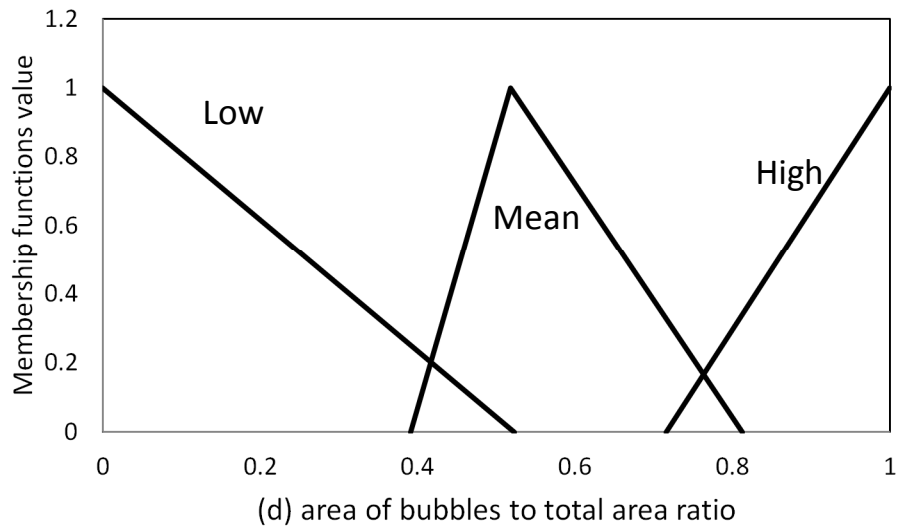
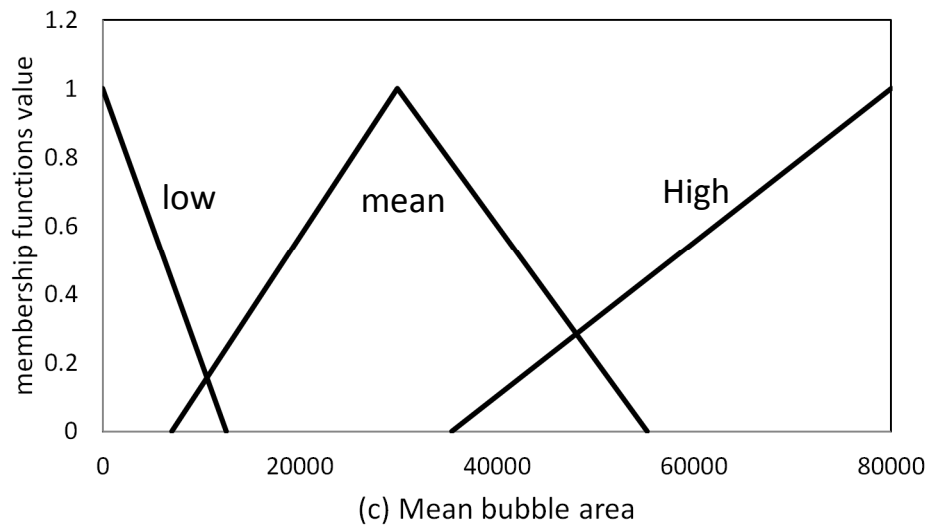


Figure 2.16. First (a), Second (b), Third (c) and Forth (d) input membership functions

By using the genetic algorithm code the following results were obtained. Membership functions of first input are depicted in Fig. 2.16a. Membership value is

depicted versus number of air bubbles. It can be seen that the genetic algorithm considers low membership functions very small and high membership values very large. In Fig. 2.16b the membership value is depicted versus the area of the biggest bubble as second input. Low values are taken up to 17,000 and high values greater than 60,000. In Fig. 2.16c the genetic algorithm considers low values approximately between 0 to 10000, mean values from 10000 to 40000 and high values greater than 40000 for the mean bubble area as the third input. Finally, in Fig. 2.16d it can be seen that genetic algorithm has considered the range of low membership functions greater. As it can be seen, low membership functions are in the range of 0 to 0.5, mean ones in the range of 0.5 to 0.75 and high ones in the range of 0.75 to 1. After investigation of membership function, it is aimed to study fuzzy rules. The fuzzy rules are expressed in table 2.3.

Table 2.3. Rules of fuzzy algorithm

Rule	Conditions	Flow pattern
R1	<ul style="list-style-type: none"> • Number of bubbles belongs to low membership functions • Biggest area of bubbles belongs to high membership functions • Average area of bubbles belongs to high membership functions • Ratio of bubble area to total area belongs to high membership functions 	Annular
R2	<ul style="list-style-type: none"> • Number of bubbles belongs to mean membership functions • Biggest area of bubbles belongs to high membership functions • Average area of bubbles belongs to mean membership functions • Ratio of bubbles area to total area belongs to high membership functions 	Churn
R3	<ul style="list-style-type: none"> • Number of bubbles belongs to high membership functions • Biggest area of bubbles belongs to low membership functions • Average area of bubbles belongs to low membership functions • Ratio of bubbles area to total area belongs to low membership functions 	Bubbly
R4	<ul style="list-style-type: none"> • Number of bubbles belongs to mean membership functions • Biggest area of bubbles belongs to mean membership functions • Average area of bubbles belongs to low membership functions • Ratio of bubbles area to total area belongs to mean membership functions 	Slug

Flow pattern recognition results from fuzzy logic code and Hewitt map are followed as below.

Table 2.4. Flow pattern identification by fuzzy logic and Hewitt map for Bubbly and Slug

Flow pattern from fuzzy logic	Flow pattern from Hewitt map	Fuzzy logic output	Ratio of bubbles area to total area	Average area of the bubbles	Biggest area of the bubbles	Number of the bubbles	Air superficial velocity	Water superficial velocity
Bubbly	Bubbly	0.14	0.2818	1121.4	14778	19	0.1	0.225
Bubbly	Bubbly	0.13	0.3264	1024.9	8954	24	0.125	0.375
Bubbly	Bubbly	0.136	0.2119	1021.9	2668	21	0.2	2
Bubbly	Bubbly	0.14	0.3383	1344.2	10078	19	0.075	0.15
Slug	Bubbly-	0.4	0.4043	2027.2	13081	15	0.25	0.75

	Slug							
Slug	Bubbly-Slug	0.345	0.4179	1838.9	15068	17	0.2	0.3
Slug-Churn	Bubbly-Slug	0.5	0.5672	1422	35874	30	0.1	0.1
Slug	Bubbly-Slug	0.374	0.4637	2944.4	14583	16	0.5	1.5
Slug	Slug	0.4	0.5092	3510	33173	11	0.25	0.45
Slug	Slug	0.4	0.6648	3585	36996	14	0.5	0.375
Slug	Slug	0.4	0.4647	2367.9	27395	15	0.5	0.75
Slug	Slug	0.4	0.5863	2626.9	22967	17	0.5	0.3
Slug	Slug	0.408	0.7556	7232.8	56944	8	0.75	0.375
Slug	Slug	0.4	0.5645	4096.6	48750	14	0.75	1.5

Table 2.5. Flow pattern identification by fuzzy logic and Hewitt map for Churn and
Annular

Flow pattern from fuzzy logic	Flow pattern from Hewitt map	Fuzzy logic output	Ratio of bubbles area to total area	Average area of the bubbles	Biggest area of the bubbles	Number of the bubbles	Air superficial velocity	Water superficial velocity
Slug-Churn	Slug	0.5	0.7602	11496	51550	5	0.75	0.225
Slug-Churn	Slug-Churn	0.5	0.7423	11496	54641	5	1.5	1
Slug-Churn	Slug-Churn	0.5	0.7079	13239	49626	4	0.9	1.5
Churn	Churn	0.6	0.8962	9629.1	67391	7	6	2
Churn	Churn	0.6	0.8567	21672	64955	3	8	4

Churn	Churn	0.6	0.9279	18569	69452	3	3.75	0.75
Churn	Churn	0.6	0.7243	15186	54943	6	2	2
Churn	Churn	0.6	0.8786	16582	69960	4	3	0.9
Churn	Churn	0.6	0.8811	39560	67052	2	4	1
Annular	Churn- Annular	0.876	0.9326	69846	69846	1	15	1
Annular	Annular	0.8944	0.9268	70153	70153	1	25	4.5
Annular	Annular	0.8944	0.9245	69765	69765	1	16	1
Annular	Annular	0.8944	0.9178	69352	69352	1	17	3.75
Annular	Annular	0.8944	0.9028	68458	68452	1	25	1

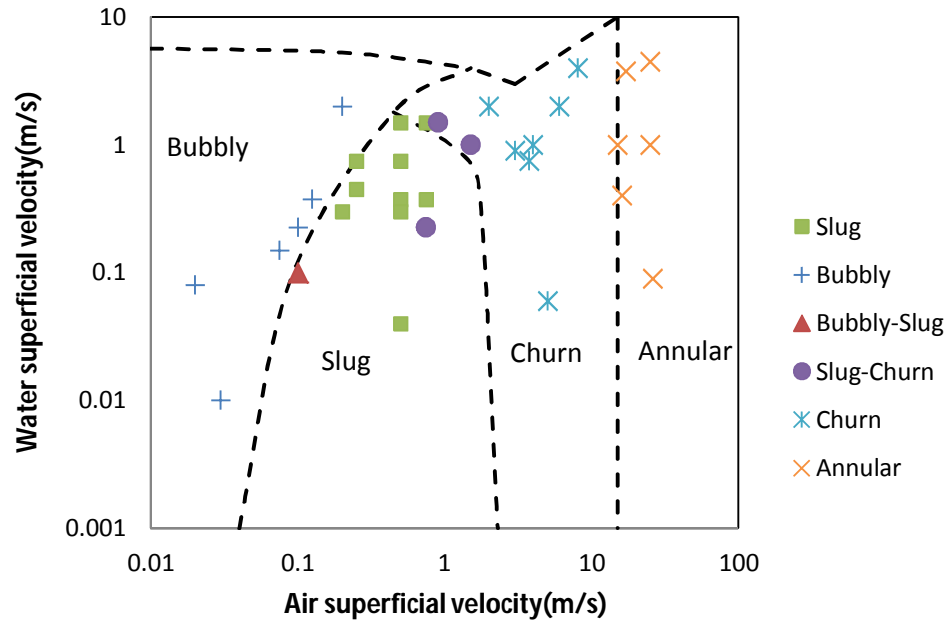


Figure 2.17. Comparison of Hewitt map with fuzzy logic results

Tables 2.4, 2.5 and Figure 2.17 show the flow pattern results from fuzzy logic and Hewitt map. It can be seen that the fuzzy logic code predicts the flow pattern very well. But its only deficiency is that it cannot recognize flow patterns at boundaries. Mostly, fuzzy logic has predicted only one of the flow patterns at the boundaries except two cases. For the first case, it has predicted a bubbly-slug flow pattern, slug-churn wrongly. In the second one, it has predicted the slug-churn flow pattern exactly at the boundary of slug-churn.

2.4 Conclusion

The results of this section can be summarized as below:

- Investigations of different types of turbulence models, i.e. k- ϵ realizable, k- ϵ standard, k- ϵ RNG and Reynolds stress shows that k- ϵ standard model needs less computational time and is more accurate compared to other turbulence models for the two phase water-gas flow in the vertical pipe.
- Ration of 0.75 for inlet water area and 0.25 for inlet air area was found perfect in terms of computational time and solution accuracy.
- It can be concluded that as number of bubbles increases, area of biggest bubble decreases and average area of bubbles decreases, then the flow pattern approaches to bubbly.
- It was concluded that as the number of bubbles decreases and fewer bubbles with larger area exists, the flow pattern becomes slug.
- If the number of bubbles decreases more and more, the flow pattern approaches to churn flow.
- If there is one large bubble occupying the whole pipe, the flow can be considered as annular.

Chapter 3

Numerical simulation of flow in a 2D pulsating heat pipe

3.1 Physical Modeling and Governing equations

The pulsating heat pipe structure consists of three sections; heating section (evaporator), cooling section (condenser) and adiabatic section. Figure 3.1 illustrates a schematic configuration of the PHP which has been used in this study. The three different sections have been distinguished by two consistent lines. The width of the tube is 3 mm. The structure and dimension of the PHP were the same for all different operating conditions. But different evaporator temperatures, condenser temperatures and filling ratios were tested for the numerical simulation. Water was the only working fluid. Figure 3.2 shows meshing configuration used in this study. To have enough space only condenser section has been depicted to show the quadrilaterals mesh which were employed for simulation. The quadrilaterals mesh was used for the whole pulsating heat pipe. In this specific test case, surface tension plays a key role in the performance of the pulsating heat pipe. It should be noted that the calculation of surface tension effects on triangular and tetrahedral meshes is not as accurate as on quadrilateral and hexahedral meshes. The region where surface tension effects are most important should therefore be meshed with quadrilaterals or hexahedra.

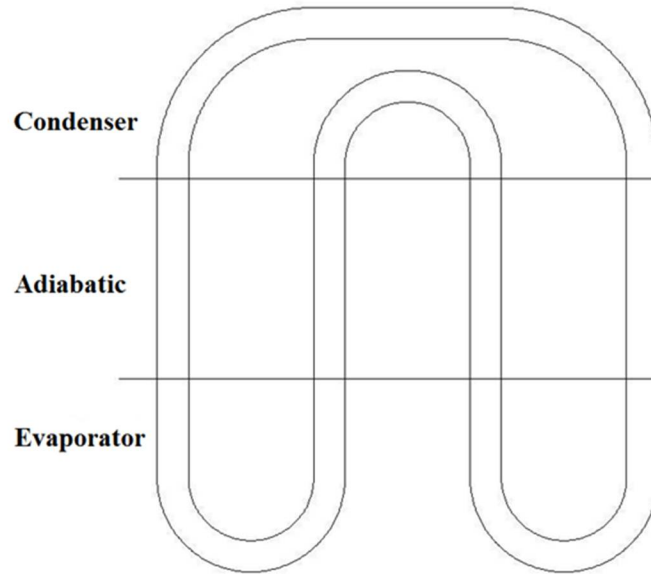


Figure 3.1. Pulsating heat pipe structure

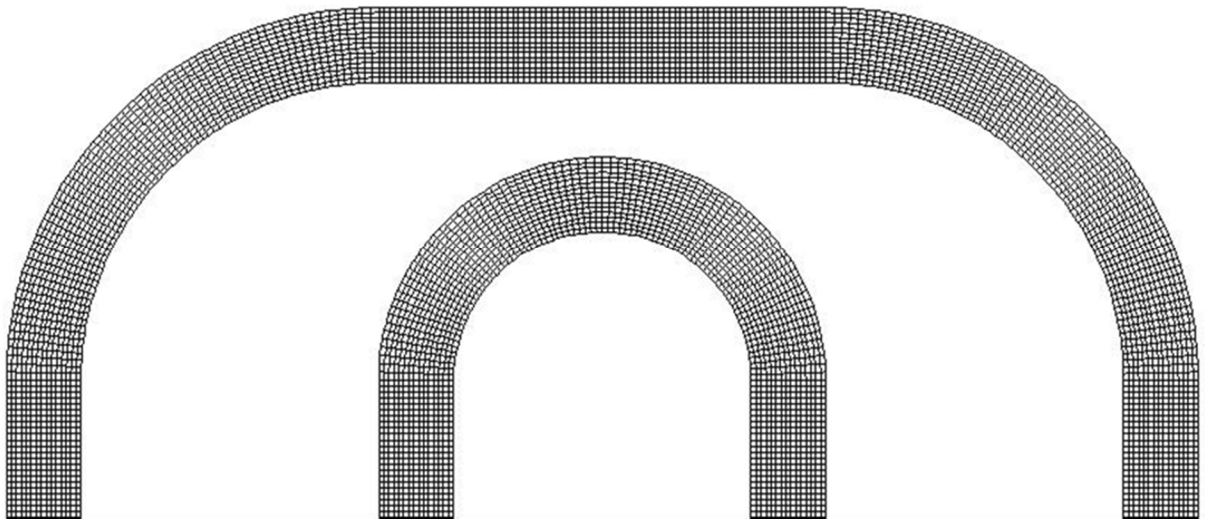


Figure 3.2. Meshing configuration (not in scale)

A large number of flows encountered in nature and technology are a mixture of phases. Physical phases of matter are gas, liquid, and solid, but the concept of phase in a multiphase flow system is applied in a broader sense. In multiphase flow, a phase can be defined as an identifiable class of material that has a particular inertial response to and interaction with the flow and the potential field in which it is immersed. For example, different-sized solid particles of the same material can be treated as different phases because each collection of particles with the same size will have a similar dynamical response to the flow field.

3.1.1 The VOF Model

The VOF model is a surface-tracking technique applied to a fixed Eulerian mesh. It is designed for two or more immiscible fluids where the position of the interface between the fluids is of interest. In the VOF model, a single set of momentum equations is shared by the fluids, and the volume fraction of each of the fluids in each computational cell is tracked throughout the domain. Applications of the VOF model include stratified flows, free-surface flows, filling, sloshing, the motion of large bubbles in a liquid, the motion of liquid after a dam break, the prediction of jet breakup (surface tension), and the steady or transient tracking of any liquid-gas interface.

We have discussed governing equations for the VOF model in chapter 2.

But two phase flow in the pulsating heat pipe includes heat transfer and phase change so that the Energy Equation is involved as part of the governing equations.

Besides, the effect of surface tension and wall adhesion are more significant in the pulsating heat pipe.

3.1.2 Energy Equation

The energy equation, also shared among the phases, is shown below.

$$\frac{\partial}{\partial t} (\rho E) + \nabla \cdot (\mathbf{v}(\rho E + p)) = \nabla \cdot (k_{eff} \nabla T) + S_h \quad (3.1)$$

The VOF model treats energy, E, and temperature, T, as mass-averaged variables:

$$E = \frac{\sum_{q=1}^n \alpha_q \rho_q E_q}{\sum_{q=1}^n \alpha_q \rho_q} \quad (3.2)$$

where E_q for each phase is based on the specific heat of that phase and the shared temperature. The properties ρ and k_{eff} (effective thermal conductivity) are shared by the phases and the source term, S_h is equal to zero.

3.1.3 Wall Adhesion

To model the wall adhesion angle in conjunction with the surface tension model, the contact angle that the fluid is assumed to make with the wall is used to adjust the surface normal in cells near the wall. This so-called dynamic boundary condition results in the adjustment of the curvature of the surface near the wall. If θ_w is the contact angle at the wall, then the surface normal at the live cell next to the wall is

$$\hat{\mathbf{n}} = \hat{\mathbf{n}}_w \cos\theta_w + \hat{\mathbf{t}}_w \sin\theta_w \quad (3.3)$$

where $\hat{\mathbf{n}}_w$ and $\hat{\mathbf{t}}_w$ are the unit vectors normal and tangential to the wall, respectively. The combination of this contact angle with the normally calculated surface normal one cell away from the wall determine the local curvature of the surface, and this curvature is used to adjust the body force term in the surface tension calculation.

3.2 Chaos

Isaac Newton brought to the world the idea of modeling the motion of physical systems with equations. It was necessary to invent calculus along the way, since fundamental equations of motion involve velocities and accelerations, which are derivatives of position. His greatest single success was his discovery that the motion of the planets and moons of the solar system resulted from a single fundamental source: the gravitational attraction of the bodies. He demonstrated that the observed motion of the planets could be explained by assuming that there is a gravitational attraction between any two objects, a force that is proportional to the product of masses and inversely proportional to the square of the distance between them. The circular, elliptical, and parabolic orbits of astronomy were no longer fundamental determinants of motion, but were approximations of laws specified with differential equations. His methods are now used in modeling motion and change in all areas of science. Subsequent generations of scientists extended the method of using differential equations to describe how physical systems evolve. But the method had a limitation. While the differential equations were sufficient to determine the behavior in the sense that solutions of the equations did exist, it was frequently difficult to figure out what that behavior would be. It was often impossible to write down solutions in relatively simple algebraic expressions using a finite number of terms. Series solutions involving infinite sums often would not converge beyond some finite time.

When solutions could be found, they described very regular motion. Generations of young scientists learned the sciences from textbooks filled with examples of differential equations with regular solutions. If the solutions remained in a bounded region of space,

they settled down to either (A) a steady state, often due to energy loss by friction, or (B) an oscillation that was either periodic or quasiperiodic, akin to the clocklike motion of the moon and planets. (In the solar system, there were obviously many different periods. The moon traveled around the earth in a month, the earth around the sun in about a year, and Jupiter around the sun in about 11.867 years. Such systems with multiple incommensurable periods came to be called quasiperiodic.)

Scientists knew of systems which had more complicated behavior, such as a pot of boiling water, or the molecules of air colliding in a room. However, since these systems were composed of an immense number of interacting particles, the complexity of their motions was not held to be surprising.

Around 1975, after three centuries of study, scientists in large numbers around the world suddenly became aware that there is a third kind of motion, a type (C) motion, that we now call “chaos”. The new motion is erratic, but not simply quasiperiodic with a large number of periods, and not necessarily due to a large number of interacting particles. It is a type of behavior that is possible in very simple systems [48].

3.2.1 Example of Chaos application

3.2.1.1 Double Pendulum

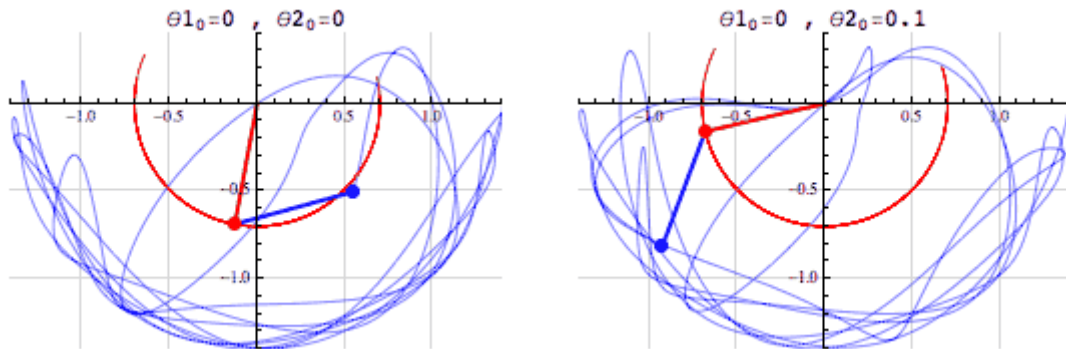


Figure 3.3. Double Pendulum Motion

The double pendulum is a simple and elegant demonstration of a complex system. A single pendulum consists of a weight that is free to rotate about a fixed axis. Pendulums have been used since the 1600s in clocks. Pendulums swing back and forth with a constant time between each swing that depends of the length of the pendulum, making them useful in time keeping. A double pendulum is a system in which a single pendulum has a second single pendulum attached at the end of the first. Under certain conditions, such as small oscillations, the double pendulum can be just as consistent as the single pendulum, however under more extreme cases the double pendulum can behave erratically. What is

interesting about the double pendulum is that it is a system of deterministic chaos. That is, for a given starting position, you can predict where the pendulum will be at some point in the future. However, even incredibly slight variations in the starting location can lead to very different positions only a short time later. The planar double pendulum serves as a paradigm for chaotic dynamics in classical mechanics. The character of its motion changes dramatically as the energy is increased from zero to infinity. At low energies, the system represents a typical case of coupled harmonic oscillators, and therefore, can be treated as an integrable system. At very high energies, the system is again integrable because the total angular momentum is a second conserved quantity besides energy. At intermediate energies, however, it exhibits more or less chaotic features.

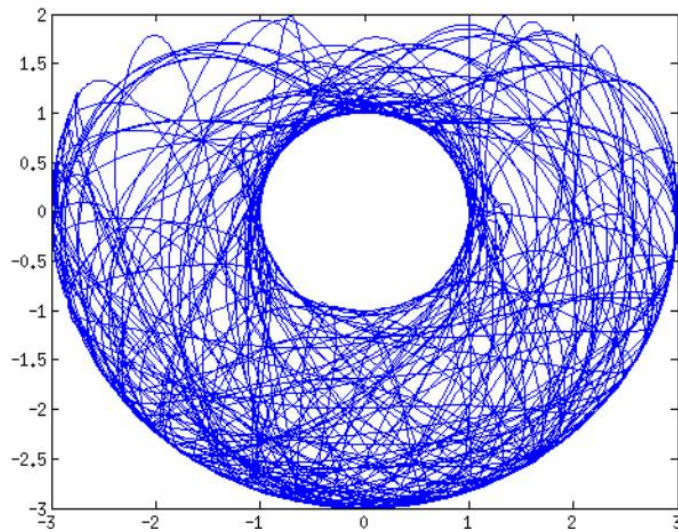


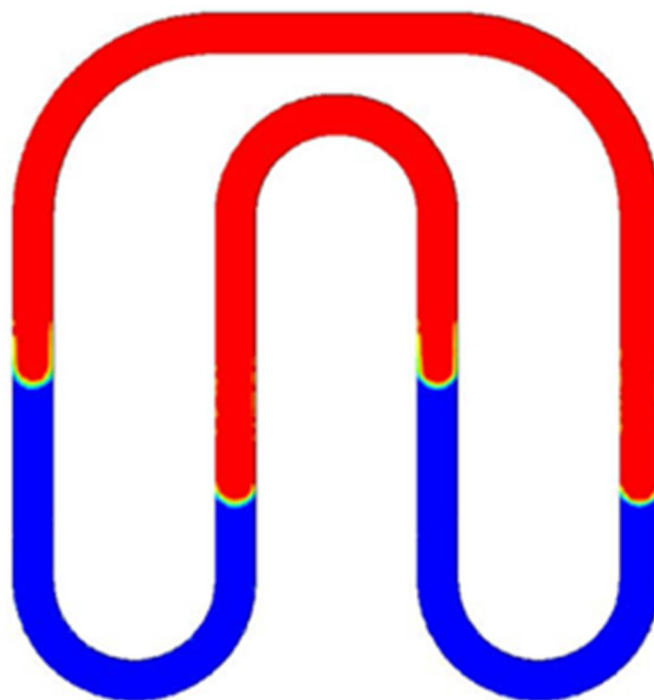
Figure 3.4. Location plot of the pendulum motion

3.3 Results and Discussion

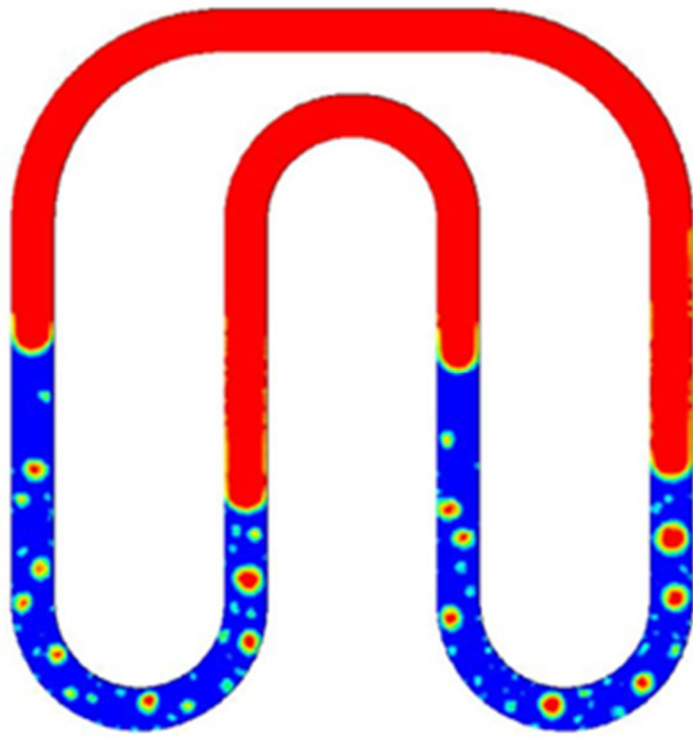
3.3.1 Volume fractions and Time series Analysis

Volume fraction contours at different points in time have been brought for two different operating conditions in this section (Red color represent the vapor and Blue color represent the liquid). The first four figures in figure 3.5 show the evolution process for the flow in PHP. The last four figures in figure 3.5 show the volume fraction contours after the fluid flow has been formed. Different structures, filling ratios, evaporator temperatures and condenser temperatures were investigated to form flow with perfect liquid and vapor plugs in PHP. It is obvious in figure 3.5 that liquid and vapor plugs are formed perfectly instead of stratified flow in PHP. The results showed that the fluid flow finally circulates in one direction (clockwise or counterclockwise) at the pulsating heat pipe. This direction is based on a random process and could be different even in the same operating and boundary conditions [51]. The liquid and vapor plug transport is due to the pressure pulsation in the system. Since the pressure pulsations are fully thermally driven, there is no external mechanical power source required for the fluid transport. Difference in temperatures for evaporator and condenser and fluid flow in the system cause temperature gradients inside the PHP. The net effect of all these temperature gradients within the system is to cause non equilibrium pressure condition which, as mentioned earlier is the primary driven force for thermo-fluidic transport. One of the most important advantages of current numerical simulation comparing to the other experimental and theoretical studies for PHPs is that it's easier to set and test many different operating conditions. But for such an experimental

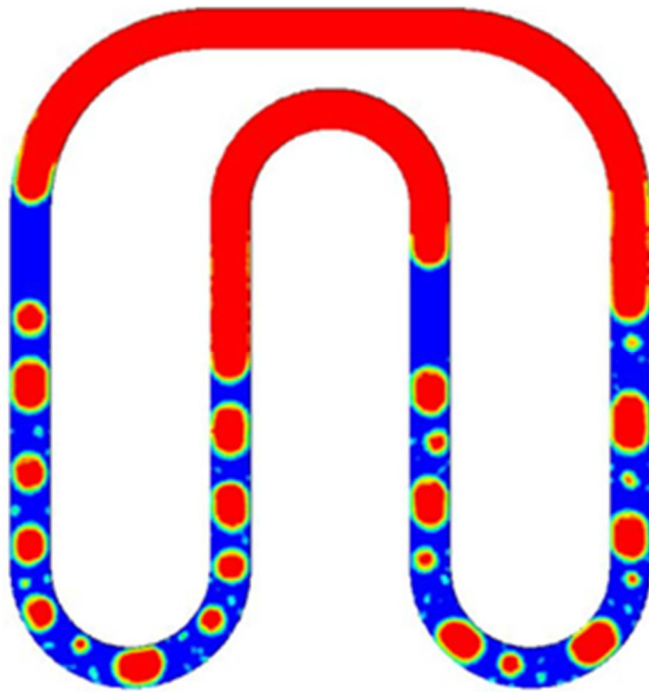
investigation it may need some equipment that could be expensive and difficult to prepare and set up in a proper way which may cause many difficulties and limitations.



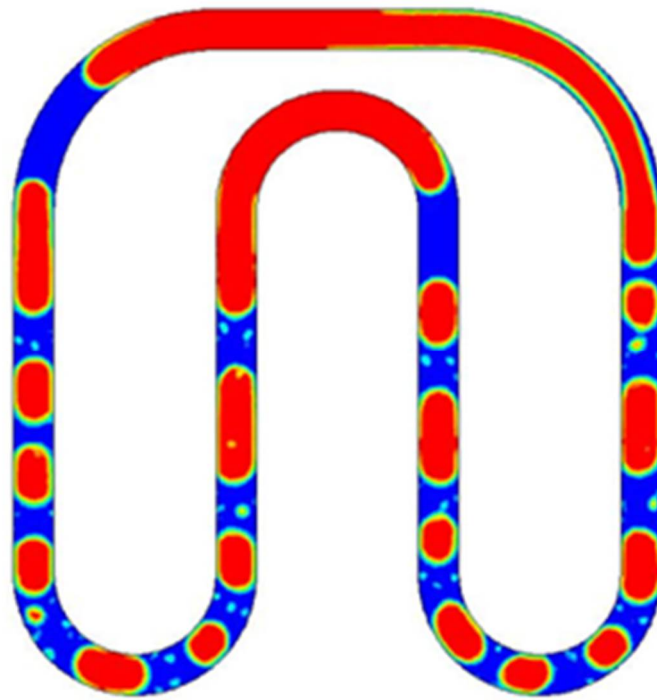
$t=0.8$ s



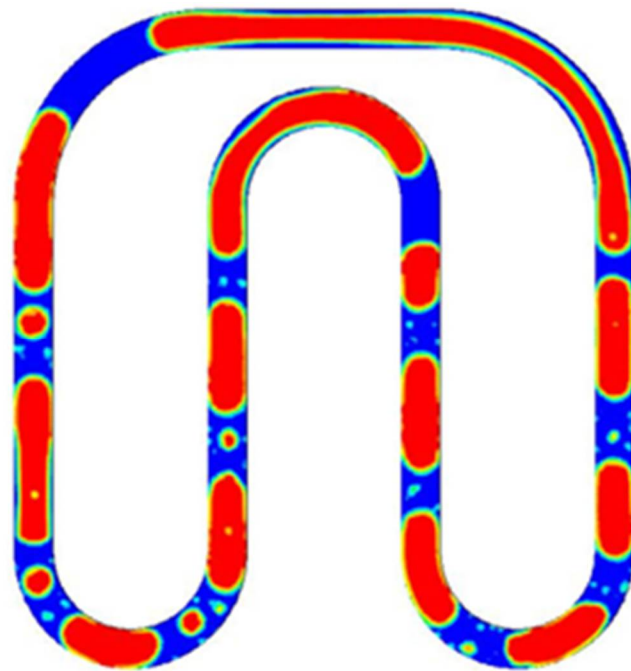
$t=2.5$ s



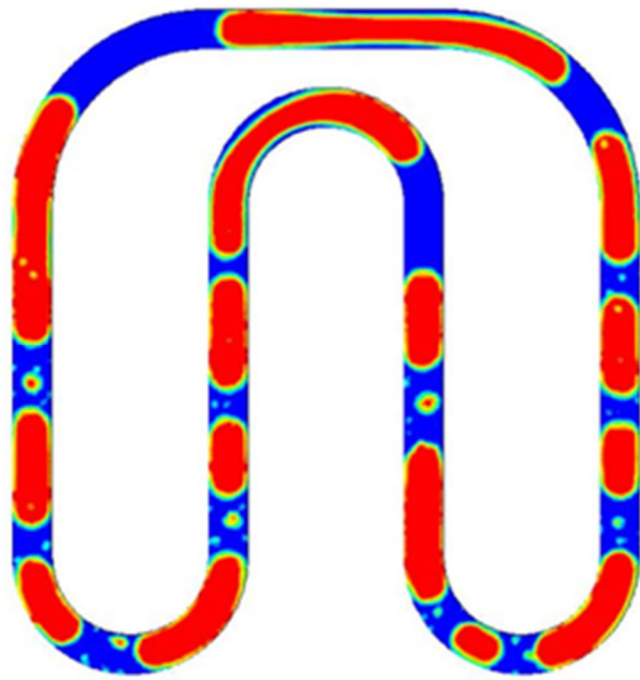
$t=3.8$ s



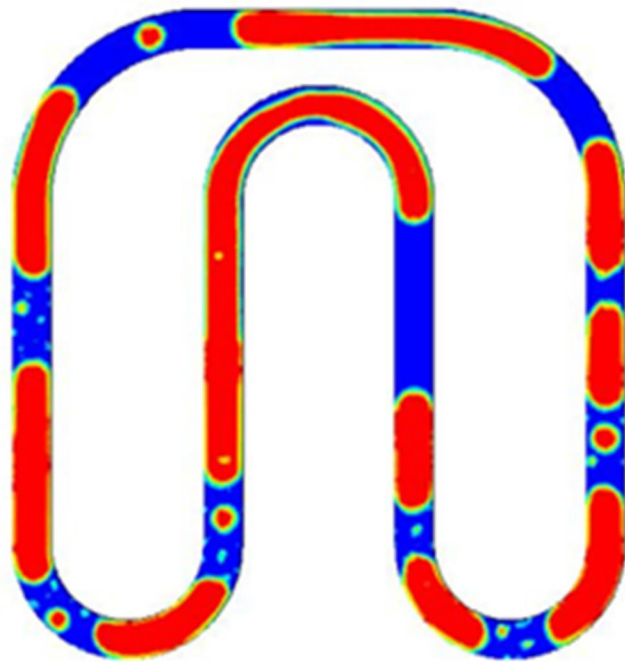
t=4.8 s



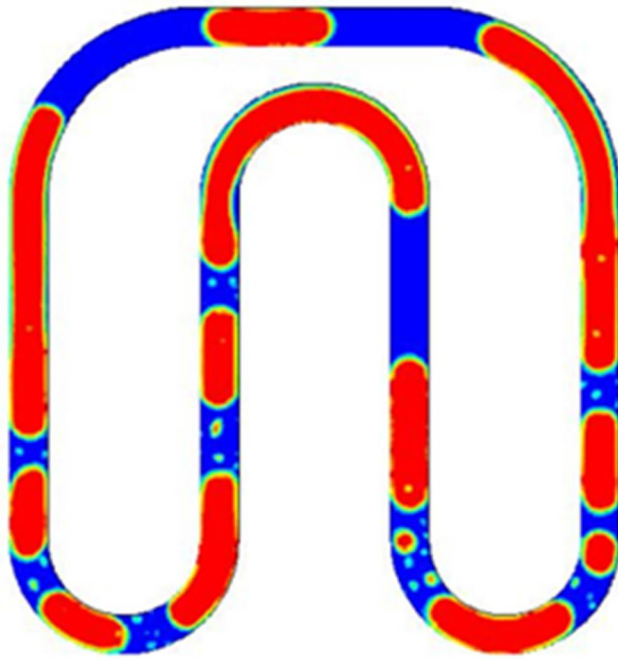
t=5.5 s



$t=8.5$ s

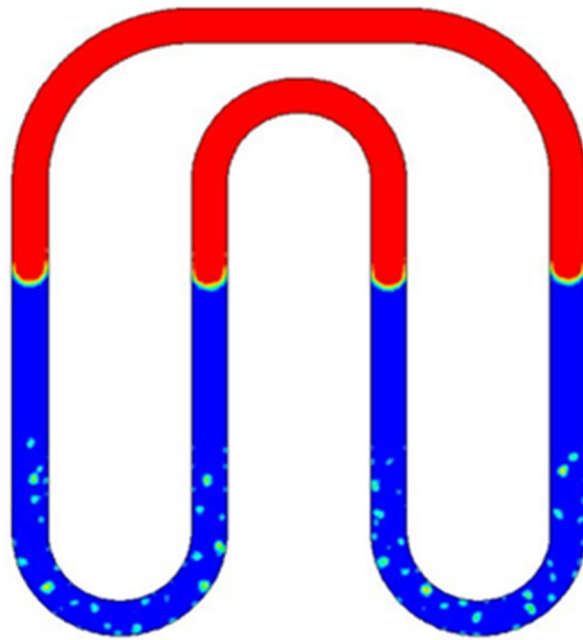


$t=13$ s

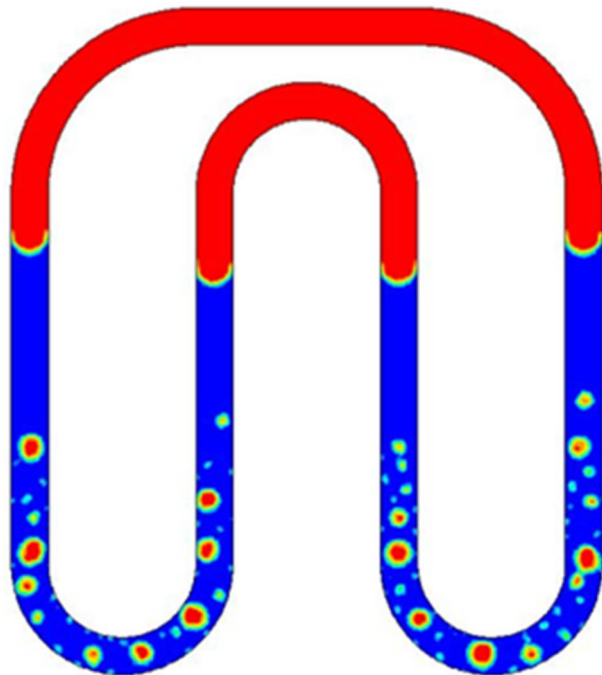


t=18 s

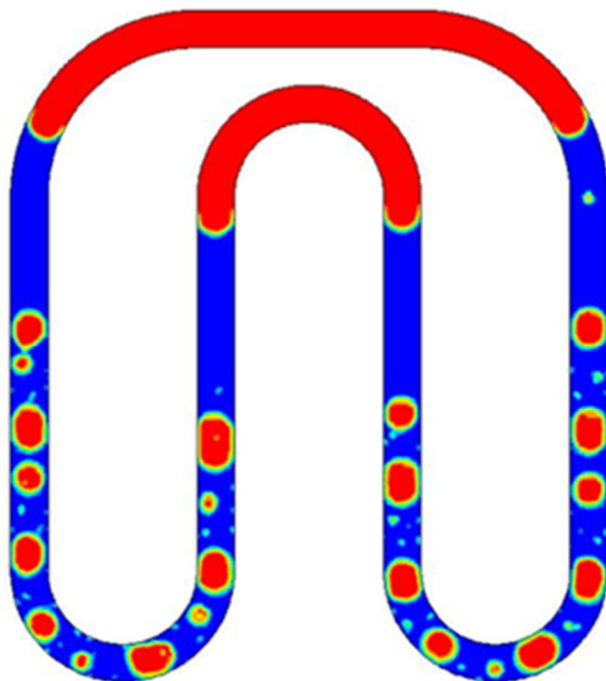
Figure 3.5. Volume fractions for $T_h=145\text{ }^\circ\text{C}$, $T_c=35\text{ }^\circ\text{C}$ and filling ratio of 30%



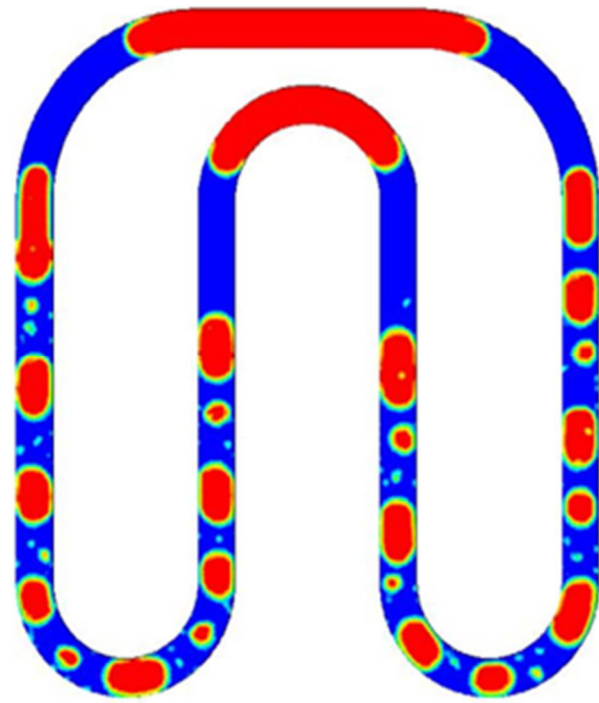
t=2.2 s



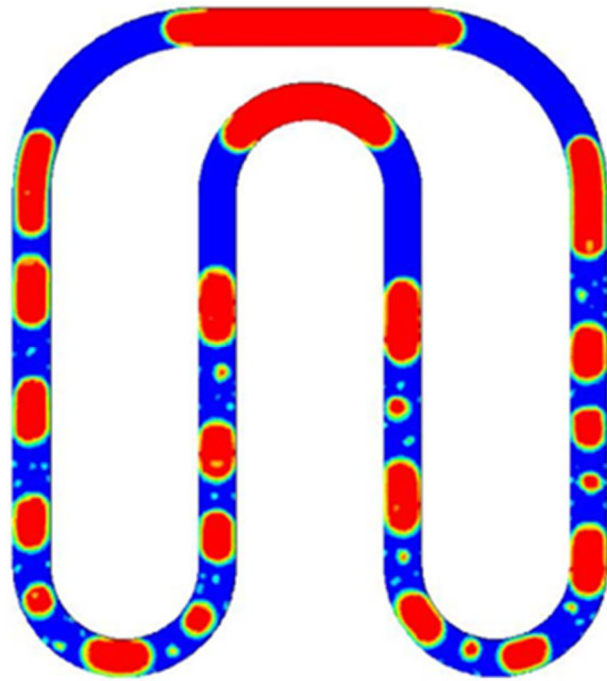
$t=3.8 \text{ s}$



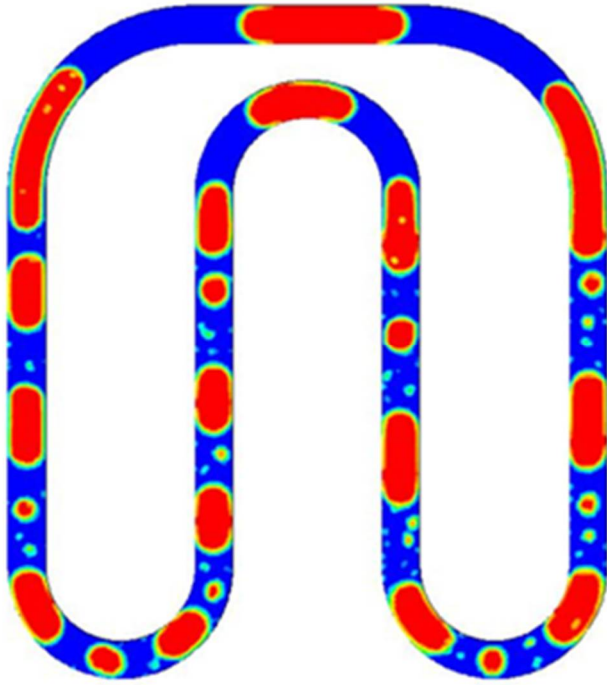
$t=5.8 \text{ s}$



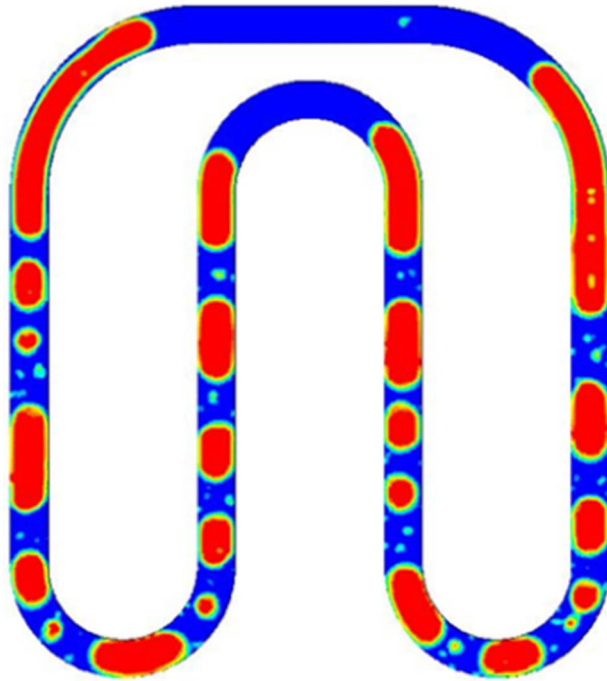
t=8.2 s



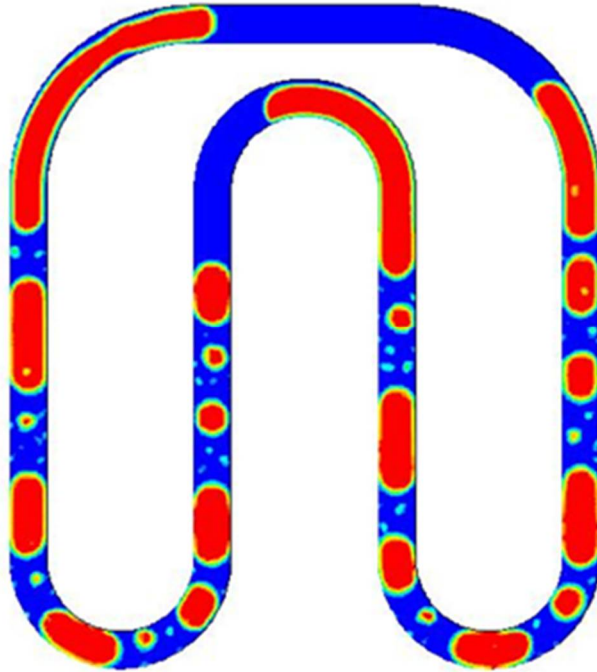
t=10 s



t=12.4 s



t=16.5 s



t=18.6 s

Figure 3.6. Volume fractions for $T_h=150$ °C, $T_c=35$ °C and filling ratio of 60%

Figure 3.7 shows a picture of liquid-vapor plugs as result of simulation in vertical part of the system. The flow pattern in the PHP is categorized as capillary slug flow. Because of the capillary structure of the PHP, liquid plugs having menisci on the plug edge are formed due to surface tension forces.

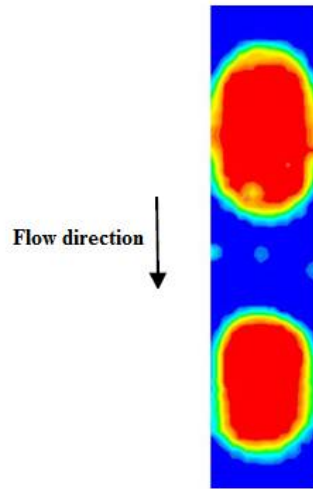


Figure 3.7. Liquid and vapor plugs in the vertical tube of the PHP

Liquid thin film exists around the vapor plug. The thickness of the liquid film may vary depend on some boundary conditions. One of the most important parameters affecting the liquid film is the wall temperature in the PHP. Since evaporator, condenser and adiabatic sections have different working temperatures liquid film with different thickness may form in these regions. Figure 3.8 shows three different liquid films surrounding the vapor plugs with different thicknesses as result of simulation.

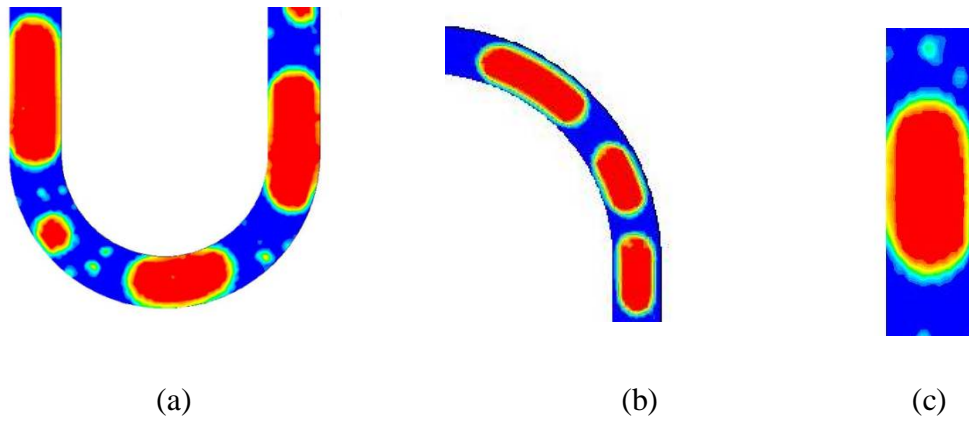


Figure 3.8. Liquid film around the vapor plugs at evaporator, condenser and adiabatic sections

Figure 3.8 illustrates vapor plugs in the evaporator, condenser and adiabatic sections respectively. It can be seen that by increasing the wall temperature, the liquid film thickness decreases.

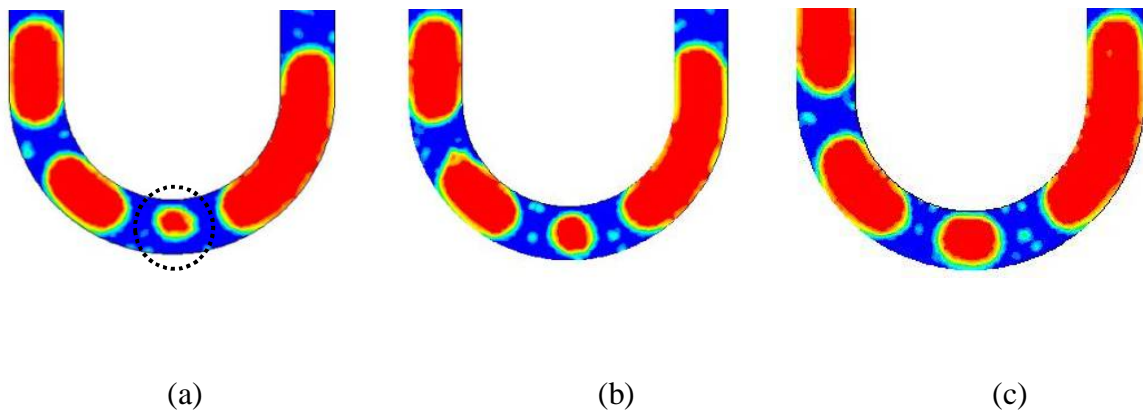


Figure 3.9. Formation and growing of the vapor bubble inside the liquid plug

In evaporator section the temperature of the liquid plugs increases which is followed by evaporation mass transfer to the adjoining vapor plug or splitting the liquid plug by formation of new bubbles inside due to the nucleate boiling in the slug flow regime. Such a process is shown in figure. 3.9. It is obvious that by creation and growing the vapor bubble (at the bottom of the evaporator), the liquid plug is breaking up. Sometimes two vapor bubbles combine together and form a larger vapor slug. Such a combination process in evaporator is illustrated in figure 3.10 as a result of simulation. But this phenomenon mostly was observed in the adiabatic section. Figure 3.11 shows vapor bubbles combination in adiabatic section. This type of behavior was observed rarely in the condenser.

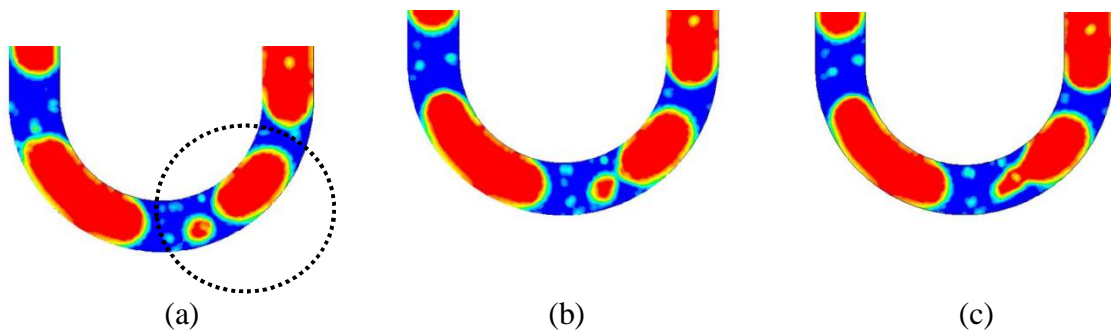


Figure 3.10. Vapor bubbles combination in evaporator



Figure 3.11. Vapor bubbles combination in adiabatic section

Liquid accumulation as a result of vapor condensation occurred on the condenser surface. This condensation process was more visible on the bending parts due to the surface tension. Figure 3.12 shows liquid accumulation on the condenser surfaces. Sometimes the condenser surfaces can be distinguished from the adiabatic surfaces by observing and tracking the thick liquid films which form on the condenser surfaces. Sometimes the gravity acceleration causes the liquid film sliding down and forming small droplets at the bottom of the condenser surface.

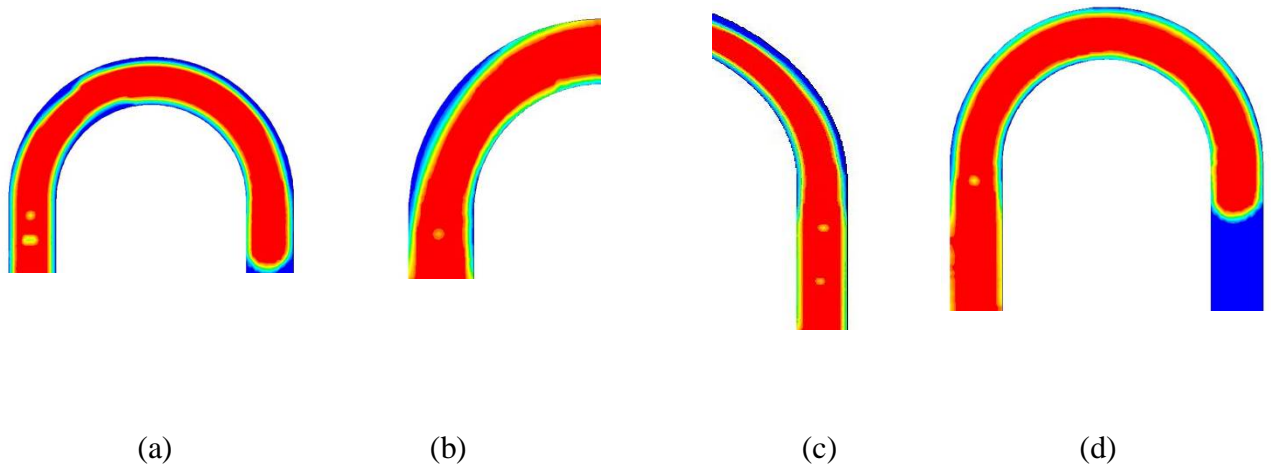


Figure 3.12. Vapor condensation and liquid accumulation on the condenser surfaces

Figure 3.12a shows vapor condensation and liquid film formation on the condenser surface. Figure 3.12b shows liquid accumulation on the bending part. Figures 3.12c & 3.12d show how the condenser section could be distinguished from the adiabatic section by tracking the liquid films thickness.

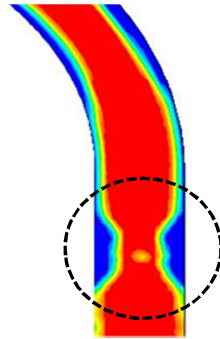
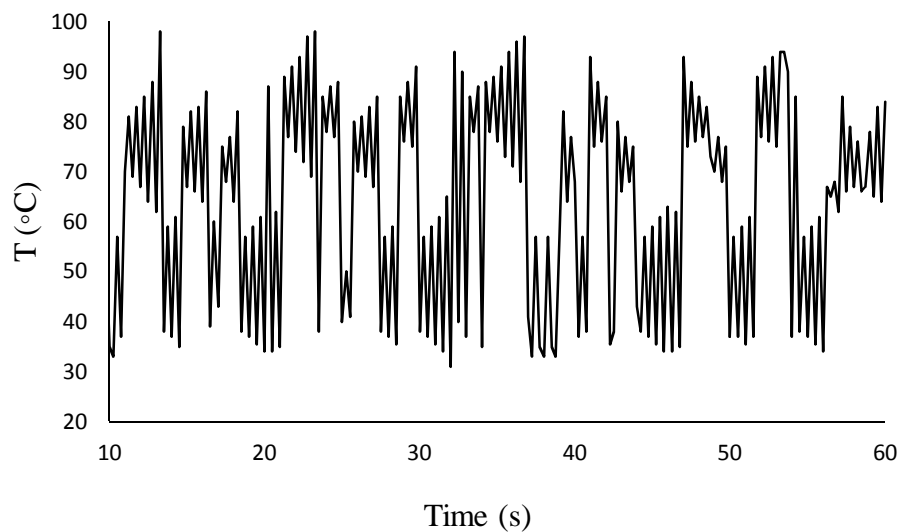


Figure 3.13. Liquid droplet formation at the bottom of the condenser

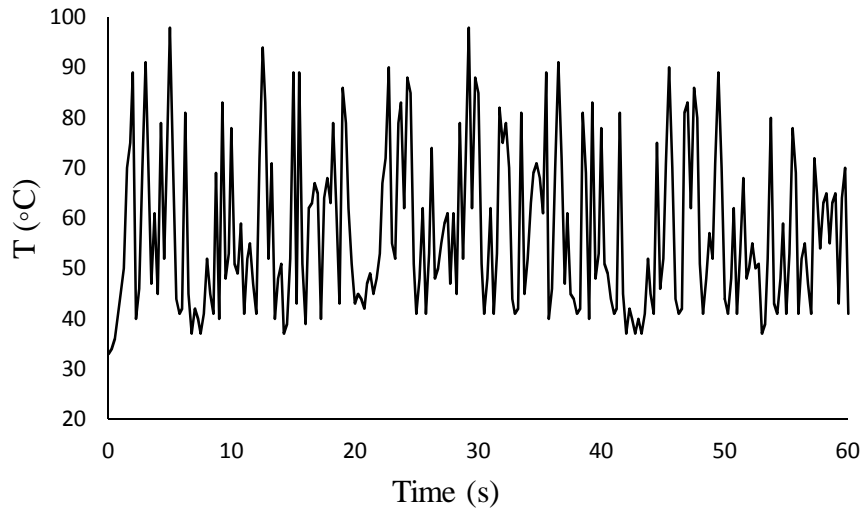
Figure 3.13. shows liquid droplet formation at the bottom of the condenser because of the liquid sliding due to the gravity acceleration.

The investigated temperature range for the evaporator and condenser in this study were 100 to 180 °C and 20 to 50 °C respectively. The range of filling ratio was 30 to 80%. It was observed that many of the simulation results failed to get a successful performance for the pulsating heat pipe because of the operating condition. The volume fraction contours of vapor and liquid plugs in a time series were the most important and visible

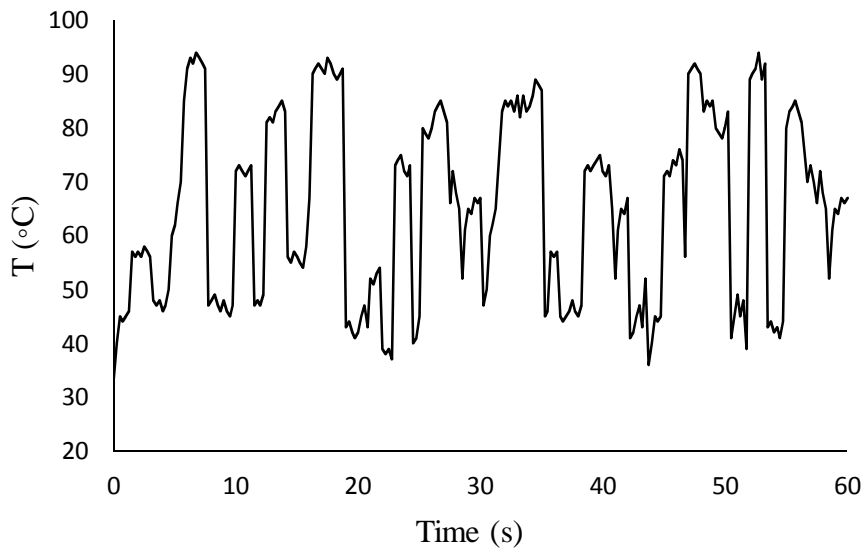
evident to recognize the flow behavior in this numerical simulation. The primary step to investigate the chaotic flow was to observe this vapor and liquid plugs in a time interval. Temperature of the adiabatic section was one of the other criteria that have been investigated to identify the chaos in PHP. Time series of temperature for different operating conditions were tested. Aperiodic, irregular, nonlinear and complex time series of temperature were obtained for those simulations that had successful performance on volume fraction contours for PHP. After observing results of simulations for time series and volume fraction contours, many of them were discarded and those that seem to have proper behavior used for further investigation of chaotic flow.



(a)



(b)



(c)

Figure 3.14. Time series of temperature for the adiabatic walls; (a): wall #1, (b): wall #4,
(c): wall #8

The analysis of data set that has been observed at different points in time leads to specific issues in statistical modeling and its interpretation. There are several objectives in analyzing a time series. The objectives may be classified as description, explanation, prediction and control. The nonlinear time series methods are based on the theory of dynamical systems which says the time evolution is defined in some phase space. Considering the importance of phase space for the study of systems with deterministic properties, it is notable that to analyze a data set, usually there is not a phase space object but a time series, most likely a sequence of scalar values. So the time series observation should be converted to the phase space. This issue of phase space reconstruction is mostly solved by the delay method [60]. In a Pulsating Heat pipe, the time series is usually a sequence of temperature values which depends on the current phase space, taken at different points in time:

$$S_n = S(T(n\Delta t)) \quad (3.4)$$

The delay reconstruction in m dimensions will be formed by the vectors \mathbf{S}_n :

$$\mathbf{S}_n = (S_{n-(m-1)\tau}, S_{n-(m-2)\tau}, \dots, S_{n-\tau}, S_n) \quad (3.5)$$

where τ is the lag or delay time which refers to time difference in number of samples between adjacent components of the delay vectors (in times units, $\tau\Delta t$).

The vector time series could be defined as:

$$\mathcal{X}(t)=[T(t), T(t+\tau), T(t+2\tau), \dots, T(t+(m-1)\tau)] \quad (3.6)$$

It is important for the dimension m of the system to be large enough. Then there is a defined number which is called true dimension of the system or fractal dimension of the system D . The reconstruction space and state space trajectories are guaranteed to be equivalent if $m \geq 2D+1$.

During the simulation, different operating conditions were tested including different evaporator and condenser temperature and different filling ratio. Water was the only working fluid that was employed for simulation. Figure 3.14 shows the time series of fluctuation of temperature on the walls of the adiabatic section. Assume numbers of 1 to 8 are assigned to the walls of the adiabatic section from left to the right. Locations for measuring the temperatures are at the middle of the adiabatic walls of the PHP. Evaporation temperature of 135 °C, condenser temperature of 30 °C and filling ratio of 70% are the operating conditions. Figures 3-14a, 3-14b and 3-14c illustrate the

temperatures for the walls number 1, 4 and 8 respectively. It is obvious in Figure 3.14 that the temperature behavior for the adiabatic wall under mentioned operating conditions is totally irregular and aperiodic. As mentioned earlier, the chaotic behavior for PHPs appears only under some operating conditions. In many of the simulation results, irregularity and aperiodic behavior were not observed due to its operating condition. For example, in some cases the temperature of the adiabatic section was almost constant and close to one of the evaporator or condenser sections. In some cases, the fluid was stuck in the condenser section due to the low filling ratio and low temperature of the condenser section which leads to higher surface tension for that part. In some cases, high temperature of the evaporator surface led to form abnormal vapor plugs in this section. Figure 3.15 illustrates forming abnormal vapor plugs due to the high temperature of the evaporator.

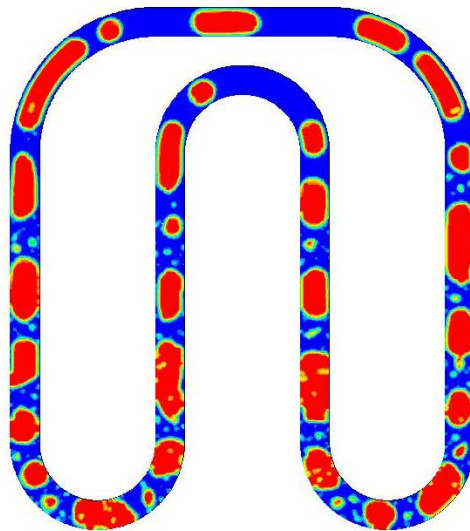


Figure 3.15. Formation of abnormal vapor plugs in evaporator

The first step to obtain and confirm chaos in a PHP was to observe irregular and aperiodic behavior in PHP. Since in this study numerical simulations were employed to investigate the flow in PHP, numerical results were used to observe this behavior. Some important approaches such Correlation Dimension, Power Spectrum Density, Lyapunov Exponents and Autocorrelation Function were employed to investigate the chaotic flow afterwards. More details of the calculations in the mentioned approaches can be found in the references [60-62].

3.3.1.1. Correlation Dimension Analysis

Finding the correlation dimension for a chaotic process from the time series data set is usually applied for getting information about the nature of the dynamical system. Correlation dimension is popular because of its simplicity and flexibility data storage requirements. It is an alternate definition for true dimension or fractal dimension. As discussed in previous section, the time series data set can reconstruct phase space formed by the trajectories of the system, the attractor. Suppose that our attractor consists of N data points obtained numerically or experimentally. Correlation sum is defined [60]:

$$C(r) = \lim_{N \rightarrow \infty} \left(\frac{\text{number of pairs of points within a sphere of radius } r}{N^2} \right) \quad (3.7)$$

In practice, we increase N until $C(r)$ is independent of N . The correlation sum typically scales as:

$$C(r) \approx \alpha r^{D_c} \tag{3.8}$$

Where D_c is the correlation dimension and r is chosen to be smaller than the size of attractor and larger than the smallest spacing between the points. In practice, we plot $\ln C(r)$ as a function of $\ln r$ and obtain the dimension D_c from the slope of the curve. The above definition of the correlation sum and dimension involve phase space vectors as the locations of points on an attractor. Thus given a scalar time series, we first have to reconstruct a phase space by an embedding procedure. Most popular method for this purpose is the delay embedding method which we mentioned earlier. In fact, the reconstruction procedure involves the choice of a delay time τ . We have to insist that the results are invariant under reasonable changes to the embedding procedure.

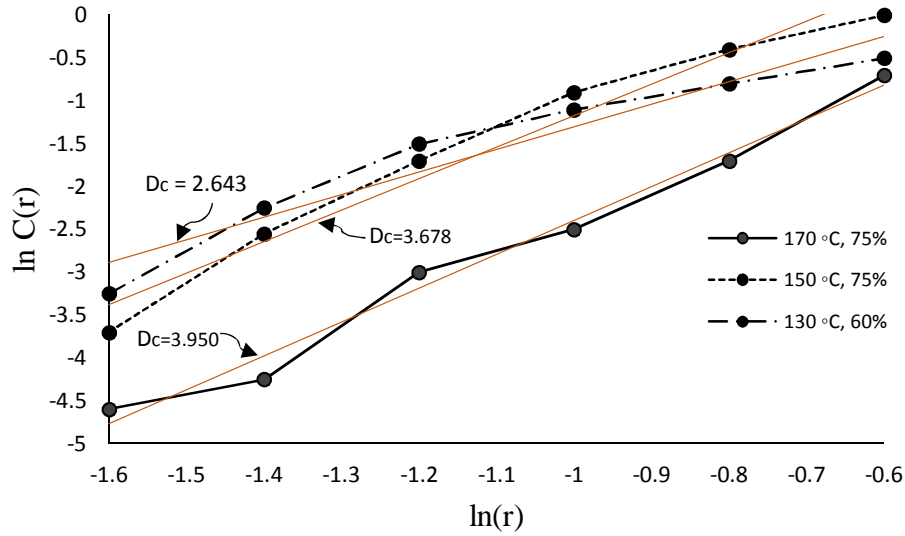


Figure 3.16. Correlation dimension values (D_c)

Figure 3.16 shows the relationship between the correlation sum as a function of radius of hyper sphere or the scale in the phase space based on the time series of temperature. Figure 3.16 illustrates the correlation dimension for three evaporation temperatures of 130, 150, 170 °C and correspondents filling ratio of 60%, 75% and 75% respectively. It is notable that the correlation dimension value is the slope of the curves. It can be seen that by increasing the evaporator temperature and filling ration, the slope of the curves, correlation dimension, increases. High values of correlation dimension refers to high frequency, small scale temperature oscillations, caused by miniature bubbles or short vapor plugs dynamically flowing in PHP tubes [51]. The lower correlation dimension corresponds to low frequency of temperature oscillations and large amplitude caused by large bubbles in the PHP. By measuring the slope of the tangent lines, correlation

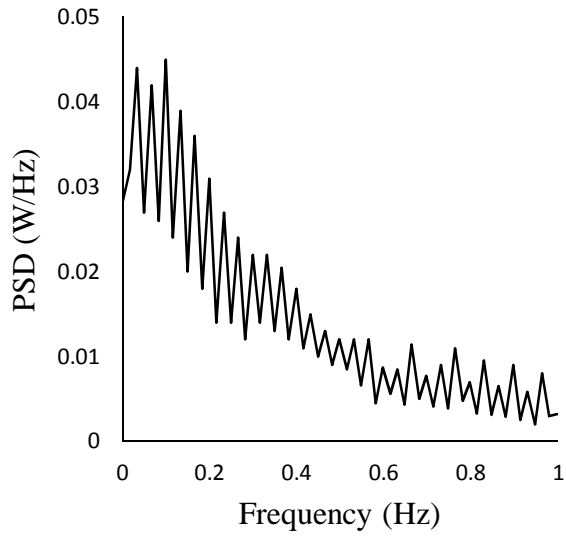
dimension values are 2.643, 3.678 and 3.95 for the evaporation temperatures of 130, 150 and 170 °C respectively.

3.3.1.2. Power spectrum Density Analysis

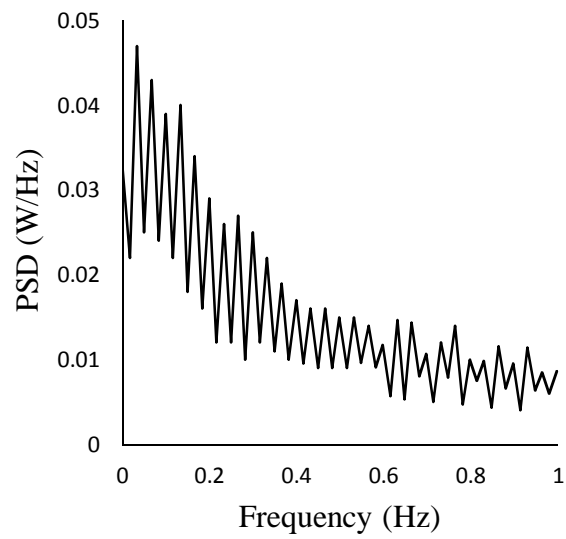
Power spectrum density (PSD) describes how the power of a signal or time series is distributed over the different frequencies. In fact, PSD is the frequency response of a random or periodic signal. It tells us where the average power is distributed as a function of frequency. The PSD is the average of the Fourier transform magnitude squared, over a large time interval. Then it can be defined as:

$$S_x(f) = \lim_{T \rightarrow \infty} E \left\{ \frac{1}{2T} \left| \int_{-T}^T x(t) e^{-j2\pi f t} dt \right|^2 \right\} \quad (3.9)$$

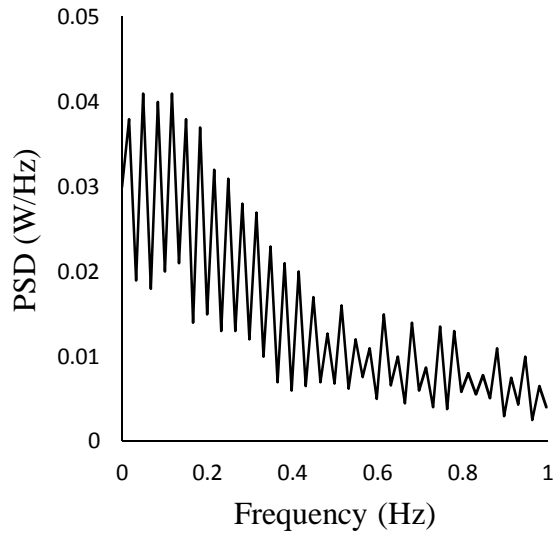
Where $x(t)$ is the random time signal and E is the energy of the signal.



(a)



(b)



(c)

Figure 3.17. Power spectrum density of the times series of temperature for the adiabatic walls; (a): wall #1, (b): wall #4, (c): wall #8

Figure 3.17 shows the power spectrum density of the time series for the temperature on the adiabatic wall by Matlab analysis. It is notable that the time step for the numerical simulation was 10^{-5} seconds. Definitely it does not mean that the data acquisition frequency was capable to achieve the value of 10^5 Hz. Regarding the operating condition and the capability of the numerical simulation for catching the temperature variation on the adiabatic section, it was reasonable to record the temperature values every 0.5 seconds. Then the highest value dedicated to the data acquisition frequency was 2 Hz. So it was possible to plot the power spectrum density diagram up to 1 Hz. Since the proper

frequency interval for investigation of the power spectrum density is equal to the maximum data acquisition frequency divided by the number of data in the related time interval (time interval considered 60 seconds, then the number of the recorded temperature values was 120 for the frequency of 2 Hz), the power spectrum density was plotted with frequency interval of $\frac{1}{60}$ Hz. The absence of dominating peaks in the power spectrum density suggests that the phenomenon is neither periodic nor quasi-periodic. Besides, the power spectrum decays by increasing the frequency. These types of behavior for power spectrum density demonstrate the chaotic state in such operating condition.

3.3.1.3. Lyapunov Exponent Analysis

In order to further prove the behavior of the pulsating heat pipe to be chaotic, Lyapunov exponent will be investigated. Lyapunov exponents are dynamical quantities. Mathematically, the property of sensitive dependence on initial conditions can be characterized by an exponential divergence between nearby trajectories in the phase space. Let $d(0)$ be the small separation between two arbitrary trajectories at time 0, and let $d(t)$ be the separation between them at time t . Then for the chaotic system:

$$d(t) \approx d(0) e^{\lambda t} \tag{3.10}$$

where λ is called the largest positive Lyapunov exponent. In the pulsating heat pipe, let X_p be the position of the liquid plug relative to its initial position. Given some initial condition X_0 , consider a nearby point $X_0+\delta$, where the initial separation δ_0 is extremely small. Let δ_n be the separation after n steps. If $|\delta_n| \approx |\delta_0| e^{n\lambda}$, λ will be the Lyapunov exponent. Here we want to introduce the most important one, the maximal Lyapunov exponent. Let S_{n1} and S_{n2} be two points in state space with distance $\|S_{n1}-S_{n2}\|=\delta_0 \ll 1$. Denote by $\delta_{\Delta n}$ the distance some time Δn ahead between the two trajectories emerging from these points, $\delta_{\Delta n}=\|S_{n1+\Delta n}-S_{n2+\Delta n}\|$. Then λ is determined by $\delta_{\Delta n} \approx \delta_0 e^{\lambda \Delta n}$, $\delta_{\Delta n} \ll 1$, $\Delta n \gg 1$. A positive λ means an exponential divergence of nearby trajectories which is a signature of chaos. A negative λ corresponds to stable fixed point and if $\lambda=0$, this means stable limit cycle. A more precise and computationally useful formula for λ with the logistic map of $f(x)$ is derived by Strogatz [61]:

$$\lambda = \lim_{n \rightarrow \infty} \left[\frac{1}{n} \sum_{i=0}^{n-1} \ln |f'(x_i)| \right] \quad (3.11)$$

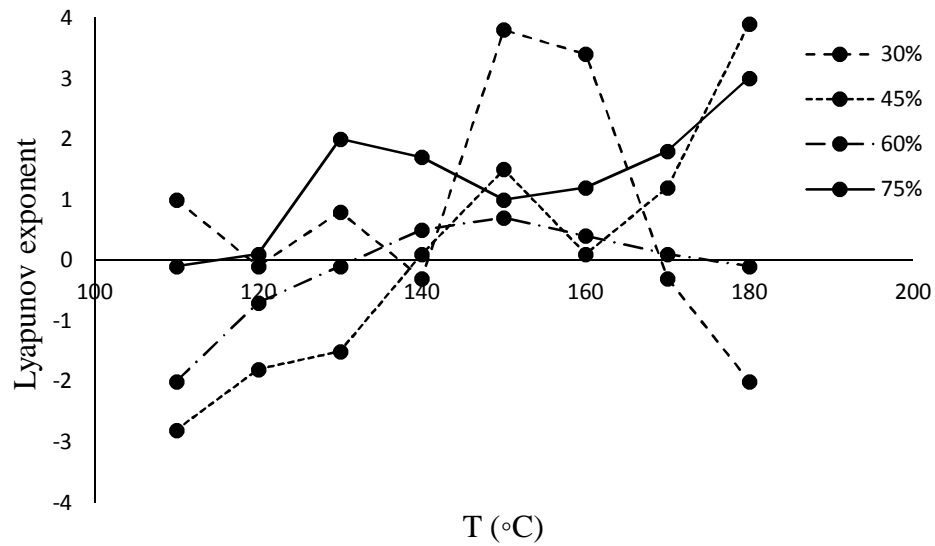


Figure 3.18. Lyapunov exponents as a function of evaporator temperature at different filling ratios

Figure 3.18 shows the Lyapunov exponents versus evaporator temperature at four filling ratio of 30%, 45%, 60% and 75%. It can be seen that for filling ratio of 30% the Lyapunov exponent mostly increases by increasing the temperature except near the temperature of 150 °C. Positive values of Lyapunov exponent can be observed for temperatures between 140 to 180 °C. At filling ratio of 45% the Lyapunov exponent increases firstly then decreases by increasing the temperature. Lyapunov exponents are positive for temperatures between 130 to 175 °C. Lyapunov exponent values are mostly positive for filling ratios of 60% and 75%. Only one negative value of Lyapunov exponent is visible for filling ratio of 75%. This signifies the chaotic state in this filling ratio for temperature values higher than 110 °C and less than 180 °C.

3.3.1.4. Autocorrelation function Analysis

Time domain analysis is the approach based on the autocorrelation functions to make inference from an observed time series to estimate the model. The theoretical autocorrelation function is an important tool to describe the properties of a stochastic process. An important guide to the persistence in a time series is given by the series of quantities called the sample autocorrelation coefficients, which measure the correlation between observations at different times. The set of autocorrelation coefficients arranged as a function of separation in time is the sample autocorrelation function, or the ACF. ACF helps to determine how quickly signals or process change with respect to time and whether a process has a periodic component [55]. The autocorrelation function will have its largest value of ACF=1 at $\tau=0$. Figure 3.19 illustrates the autocorrelation function (ACF) of time series at filling ratio of 75% and three temperature differences between evaporator and condenser. Autocorrelation function of the time series are computed as [62]:

$$ACF(\tau) = \frac{\sum_{i=1}^N (T_{i+\tau} - \bar{T})(T_i - \bar{T})}{\sum_{i=1}^N (T_i - \bar{T})^2} \quad (3.12)$$

Where T_i and $T_{i+\tau}$ are the temperature observations at the time domain, \bar{T} is the overall mean temperature and τ is the lag.

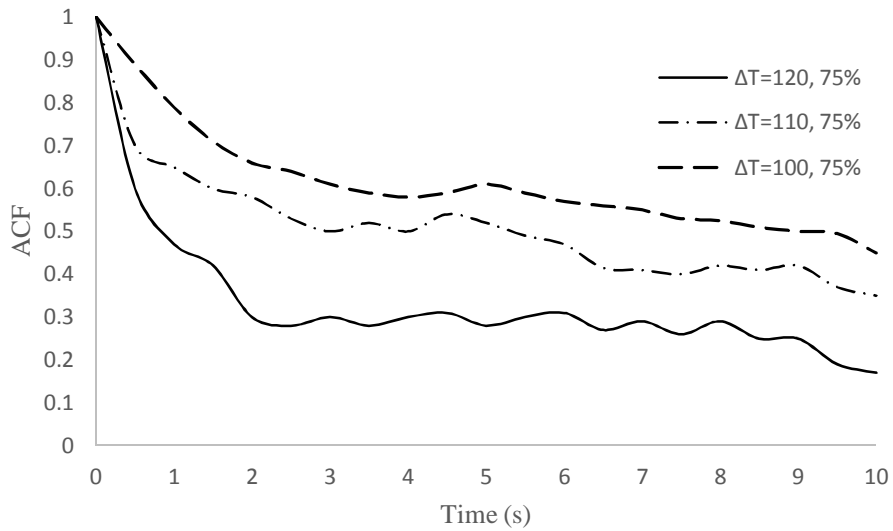


Figure 3.19. Autocorrelation function versus time

It is evident in Figure 3.19, the autocorrelation function decreases versus time. Behavior of ACF indicates the prediction ability of the system. Decreasing of the ACF shows that the prediction ability is finite. This signifies the chaotic state in the PHP. As shown in Figure 3.19 by increasing the temperature difference between the evaporator and condenser, ACF decreases. In addition, the ACF values decrease faster in higher values of temperature difference.

3.4 Conclusions

Numerical simulation was carried out to investigate the chaotic behavior of the pulsating heat pipe. Volume fractions of liquid and vapor for the working fluid were obtained in different operating conditions. Perfect vapor and liquid plugs were formed in the PHP. Liquid plugs having menisci on the plug edge were formed due to surface tension forces. It was seen that by increasing the wall temperature, the liquid film thickness around the vapor plug decreases. Splitting the liquid plugs by formation and growing of new bubbles inside was observed particularly in the evaporator. Combination of two vapor plugs and formation of a larger plug was seen in the evaporator and adiabatic section. This combination rarely occurred in the condenser. Vapor condensation and liquid accumulation were more visible on the bending parts of the condenser due to the surface tension. Liquid droplet formation at the bottom of the condenser surface was obvious due to the gravity acceleration. Time series of the adiabatic section temperature was found as proper criteria to study the chaotic state. In addition, Correlation dimension, Power spectrum density, Lyapunov exponent and Autocorrelation function approaches were conducted afterwards. It was found that the time series has complicated, irregular and aperiodic behavior in several operating conditions. Decreasing the power spectrum density of the time series with respect to frequency and absence of dominating peaks in the related curves denoted the existence of chaos in the pulsating heat pipe. It was observed that by increasing the filling ratio and evaporator temperature the correlation dimension increases. Values of 2.643, 3.678 and 3.95 were obtained for the evaporator temperatures of 130, 150 and 170 C respectively. Lyapunov exponent mostly was increased by increasing the temperature for the low filling ratio. Positive values of Lyapunov exponent were obtained for

temperatures between 140 to 180 C at filling ratio of 30%. At filling ratio of 75%, all of the Lyapunov exponents were positive for the temperature interval between 120 to 180 C which was a signature of chaos in these operating conditions. Autocorrelation function was decreased with respect to time indicating finite prediction ability of the system. Besides, by increasing the temperature difference between the evaporator and condenser, ACF was decreased. Taking everything into account, it should be mentioned that the flow behavior in the pulsating heat pipe can be classified as chaotic state under several operating conditions. This chaotic behavior can be verified and confirmed using different approaches.

Chapter 4

Numerical simulation of flow in a 2D multi-turn pulsating heat pipe

Numerical study has been conducted for the chaotic flow in a multi-turn closed-loop pulsating heat pipe (PHP). Heat flux and constant temperature boundary conditions have been applied for heating and cooling sections respectively. Water was used as working fluid. Volume of Fluid (VOF) method has been employed for two-phase flow simulation. Volume fraction results showed formation of perfect vapor and liquid plugs in the fluid flow of PHP. Non-linear time series analysis, power spectrum density, correlation dimension and autocorrelation function were used to investigate the chaos. Absence of dominating peaks in the power spectrum density was a signature of chaos in the pulsating heat pipe. It was found that by increasing the filling ratio and evaporator heating power the correlation dimension increases. Decreasing of the autocorrelation function with respect to time showed the prediction ability is finite as a result of chaotic state. An optimal filling ratio of 60% and minimum thermal resistance of $1.62 \text{ }^{\circ}\text{C}/\text{W}$ were found for better thermal performance of the pulsating heat pipe.

4.1 Physical modeling

The two dimensional structure of the PHP were the same for all different operating conditions in this work and water was the only working fluid. Different evaporator heating powers, condenser temperatures and filling ratios were tested for the numerical simulation. The pulsating heat pipe structure consists of three sections: heating section (evaporator), cooling section (condenser), and adiabatic section. Figure 4.1 illustrates a schematic configuration of the PHP which has been used in this study. The three different sections have been distinguished by two horizontal lines. The length and width of the tube are 870 mm and 3 mm respectively. The span of the PHP was considered 1 m as a 2D simulation. Figure 4.2 shows meshing configuration used in this study. Only a part of evaporator section has been depicted to show the quadrilaterals mesh which were employed for simulation. The quadrilaterals mesh was used for the entire pulsating heat pipe.

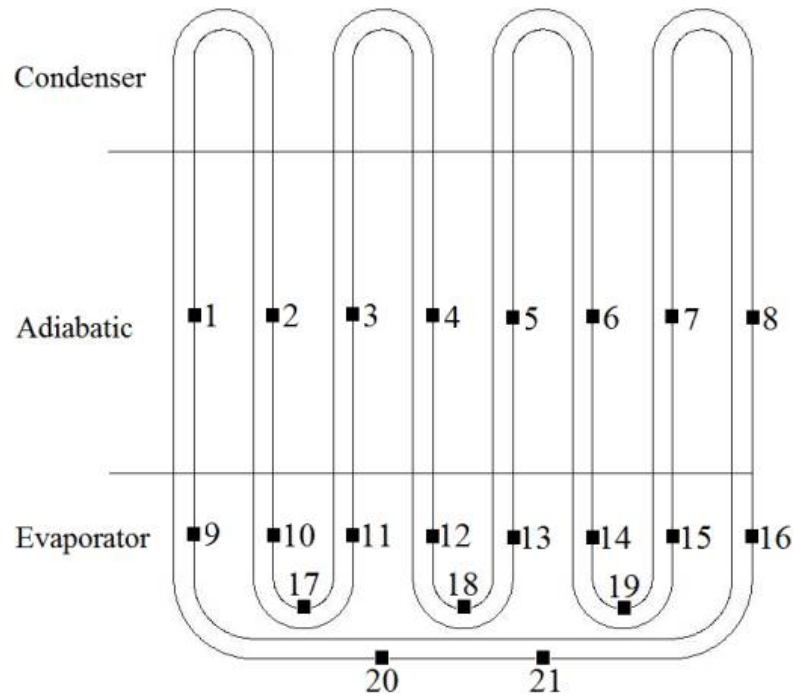


Figure 4.1. Pulsating heat pipe structure

Volume of Fluid (VOF) method has been applied for two phase flow simulation. The VOF model is a surface-tracking technique applied to a fixed Eulerian mesh. It is designed for two or more immiscible fluids where the position of the interface between the fluids is of interest. In the VOF model, a single set of momentum equations is shared by the fluids, and the volume fraction of each of the fluids in each computational cell is tracked throughout the computational domain.

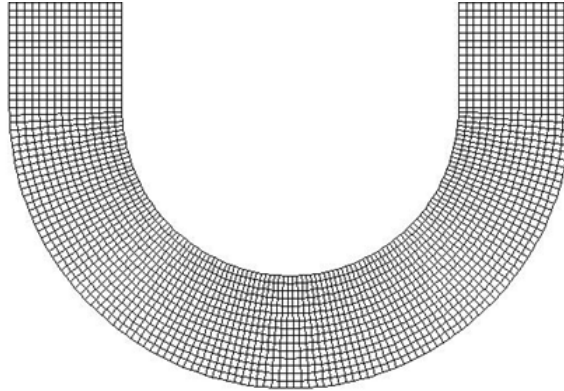


Figure 4.2. Meshing configuration

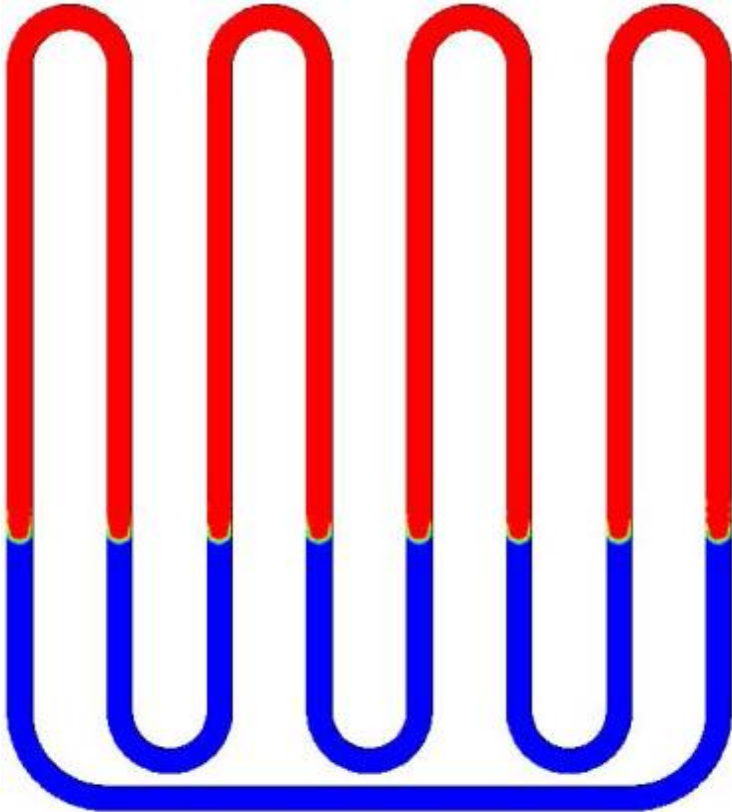
Applications of the VOF model include stratified flows, free-surface flows, filling, sloshing, the motion of large bubbles in a liquid, the motion of liquid after a dam break, the prediction of jet breakup (surface tension), and the steady or transient tracking of any liquid-gas interface. The VOF formulation relies on the fact that two or more fluids (or phases) are not interpenetrating. For each additional phase added to the model, the volume fraction of the phase in the computational cell is introduced. In each control volume, the volume fractions of all phases sum to unity. The fields for all variables and properties are shared by the phases and represent volume-averaged values, as long as the volume fraction of each of the phases is known at each location. Thus the variables and properties in any given cell are either purely representative of one of the phases, or representative of a mixture of the phases, depending on the volume fraction values. Then the q^{th} fluid's volume fraction in the cell is denoted as α_q . Based on the local value of α_q , the appropriate

properties and variables will be assigned to each control volume within the domain. The related governing equations have been discussed in chapters 2 and 3.

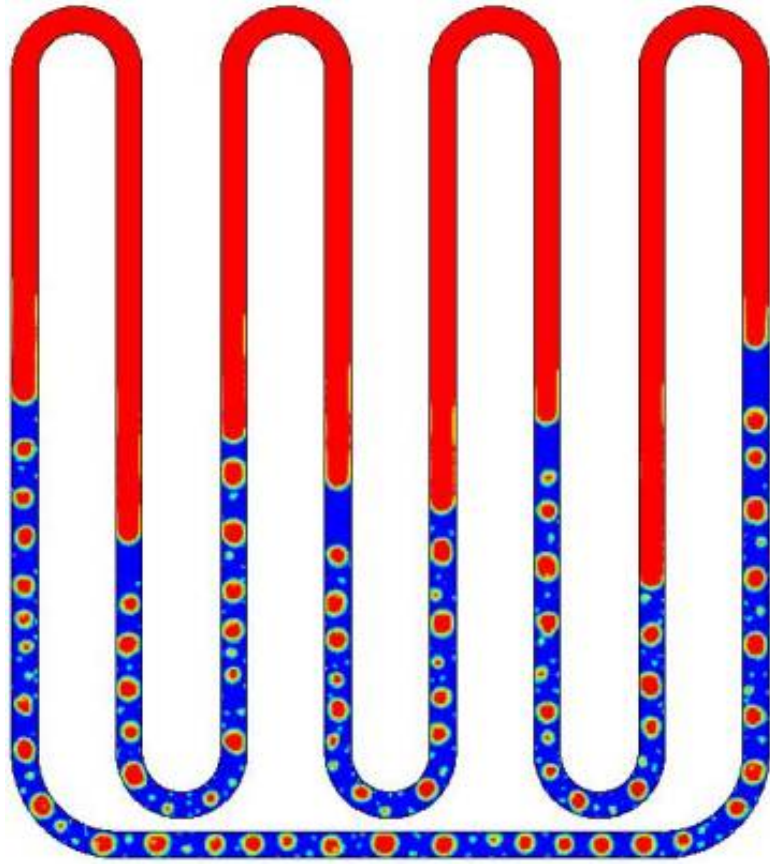
4.2 Results and discussion

Figure 4.3 illustrates volume fractions of liquid and vapor at different times (Red color represents the vapor and Blue color represents the liquid). Figure 4.3a shows almost the initial condition of the PHP. Figure 4.3b explains formation of vapor bubbles and fluid flow development in the PHP. Figure 4.3c depicts the volume fractions of liquid and vapor in the PHP after the fluid flow has been established. Mostly a similar process occurs in the PHP with filling ratio of 60% (Figure 4.4). One of the most significant effects due to the increasing the filling ratio is pressure increment in the PHP which lead to a longer time duration for boiling start (because of increasing the saturated temperature) and slower flow motion in the PHP. The effect of change in filling ratio on the chaotic and thermal behavior of the PHP will be investigated in the next sections afterwards. It is evident liquid plugs having menisci on the plug edges are formed due to surface tension forces. A liquid thin film also exists surrounding the vapor plug. The angle of contact of the menisci, the liquid thin film stability and its thickness depends on the fluid-solid combination and the operating parameters which are selected. If a liquid plug is moving or tends to move in a specific direction then the leading contact angle (advancing) and the lagging contact angle (receding) may be different. This happens because the leading edge of the plug moves on a dry surface (depending on the liquid thin film stability and existence) while the lagging

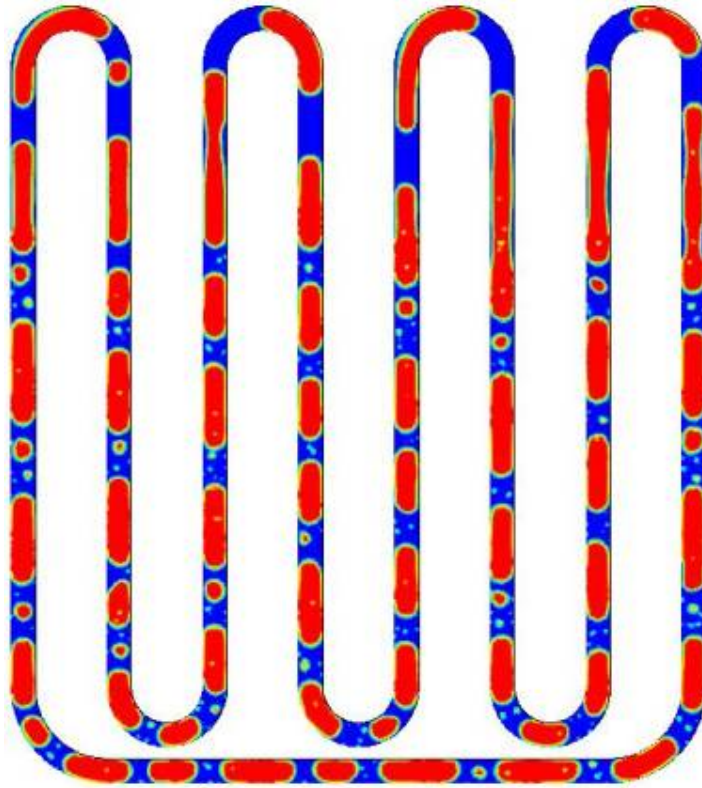
edge moves on the just wetted surface. These characteristics can be observed in Figure 4.5 as result of numerical simulation.



(a)

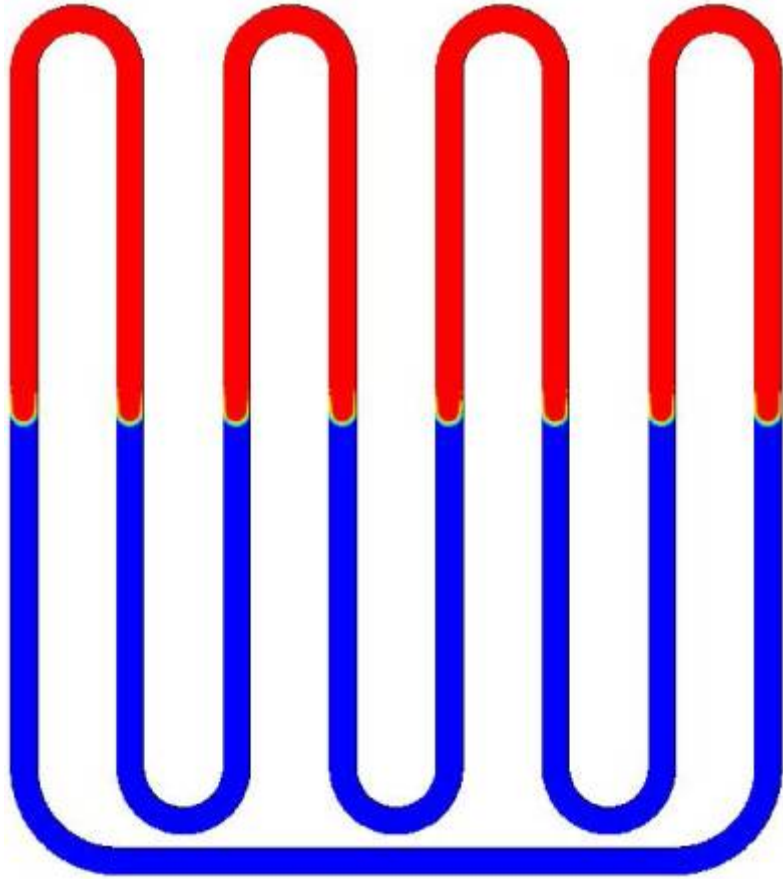


(b)

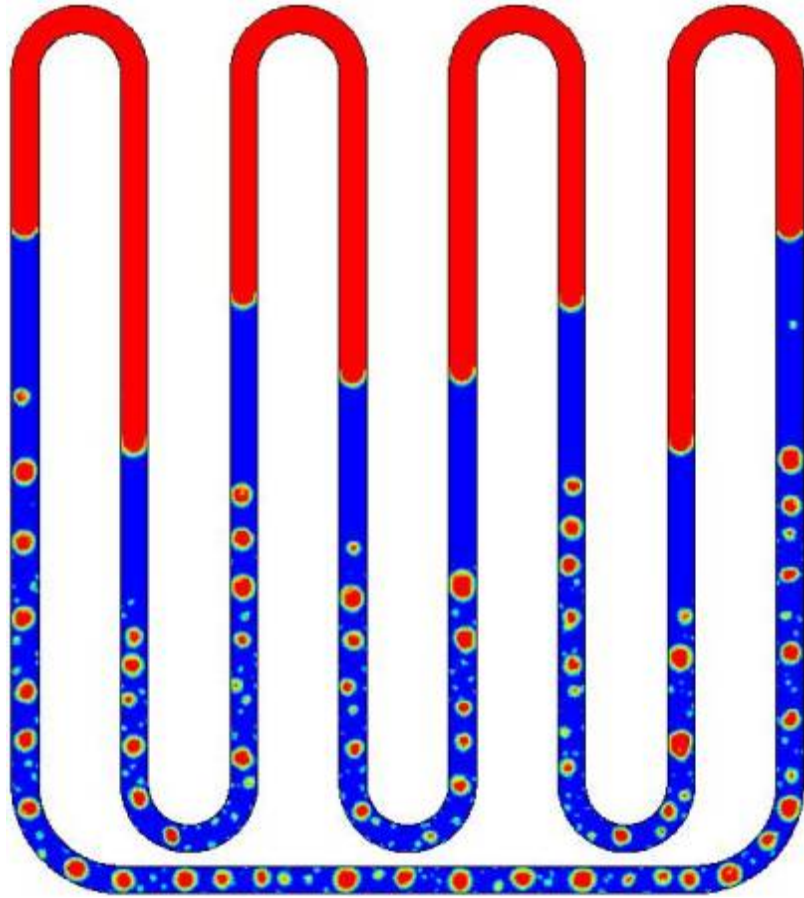


(c)

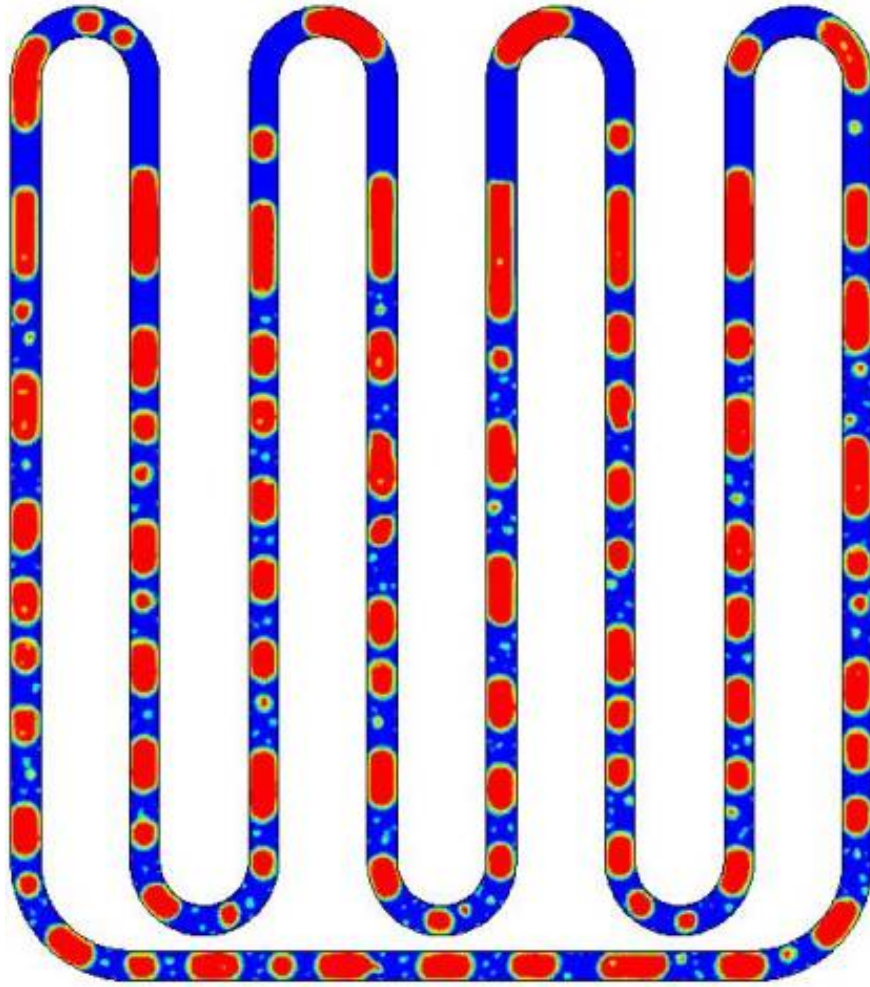
Figure 4.3. Volume fractions of liquid and vapor at different times with $Q=40$ W, $T_c=30$ °C and $FR= 35\%$; (a): $t=0.1$ s, (b): $t=1.7$ s, (c): $t=20$ s.



(a)



(b)



(c)

Figure 4.4. Volume fractions of liquid and vapor at different times with $Q=55$ W, $T_c=25$ °C and $FR= 60\%$; (a): $t=0.1$ s, (b): $t=2.6$ s, (c): $t=20$ s.

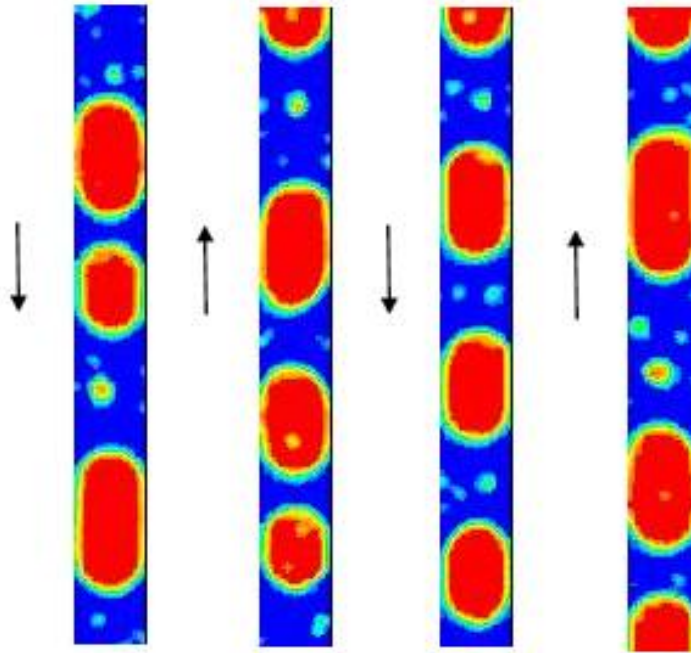
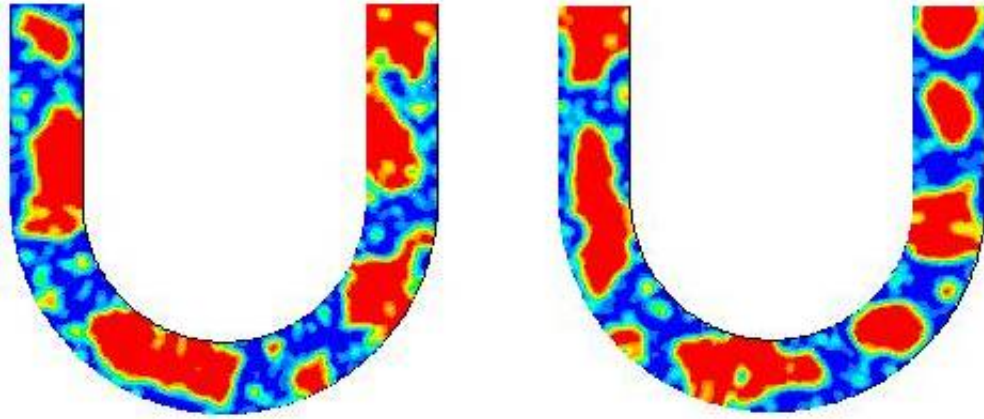


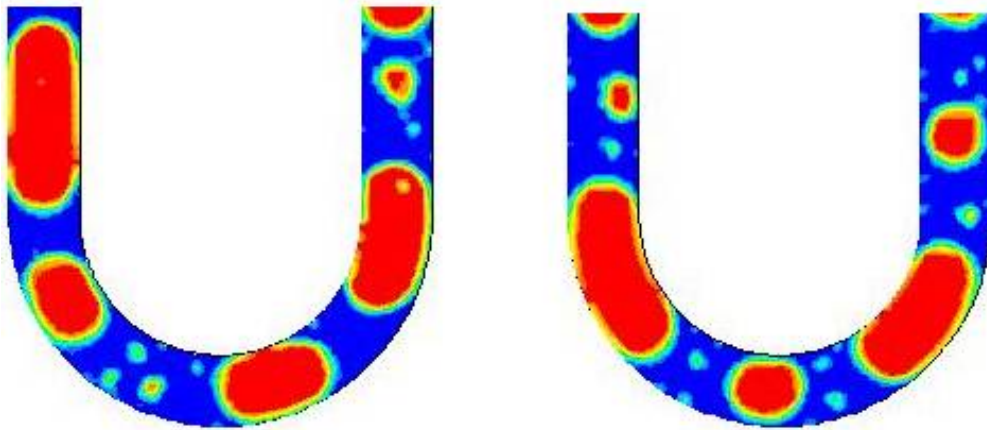
Figure 4.5. Vapor and liquid plugs in the PHP

The results showed that the fluid flow finally circulates in one direction (clockwise or counterclockwise) in the pulsating heat pipe. This direction is based on a random process and could be different even under the same operating and boundary conditions. It is seen that by increasing the wall temperature, the liquid film thickness around the vapor plugs decreases. In evaporator section the temperature of the liquid plugs increases which is followed by evaporation mass transfer to the adjoining vapor plug or splitting the liquid plug by formation of new bubbles inside due to the nucleate boiling in the slug flow regime. Sometimes two vapor bubbles combine together to form a larger vapor slug. This phenomenon was mostly observed in the adiabatic section and rarely was observed in the

condenser. In addition, liquid accumulation as a result of vapor condensation occurred on the condenser surface. This condensation process was more visible on the bending parts due to the surface tension. It was observed that many of the simulation results failed to get a successful performance for the pulsating heat pipe because of the operating condition. In some cases, the fluid was stuck in the condenser section due to the low filling ratio and low temperature of the condenser section which leads to higher surface tension for that part. In some cases, high temperature of the evaporator surface led to form abnormal vapor plugs in this section due to the intensive nucleate boiling and formation of superheated vapor.



(a)



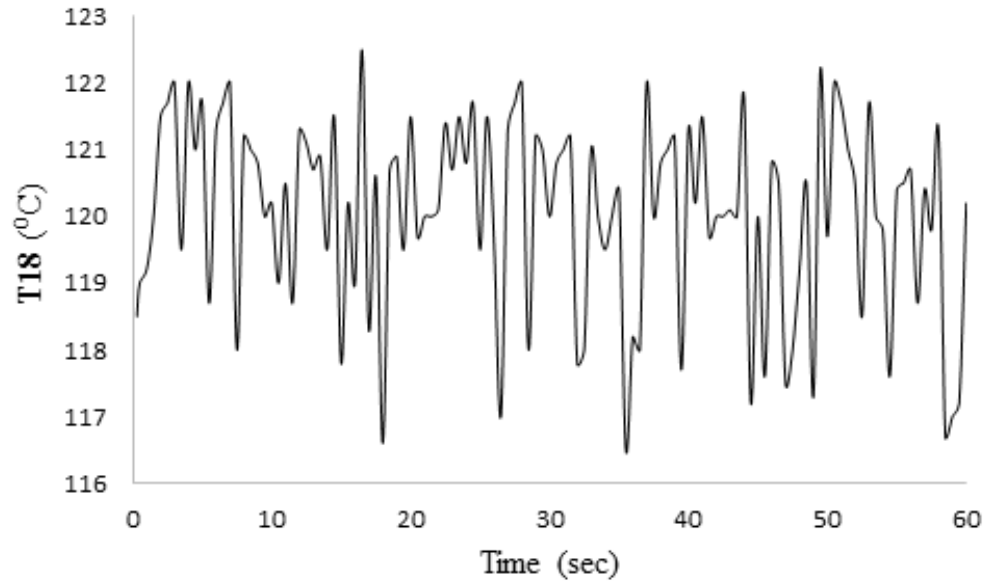
(b)

Figure 4.6. Comparing formation of abnormal vapor plugs (a) with normal vapor plugs (b) at evaporator

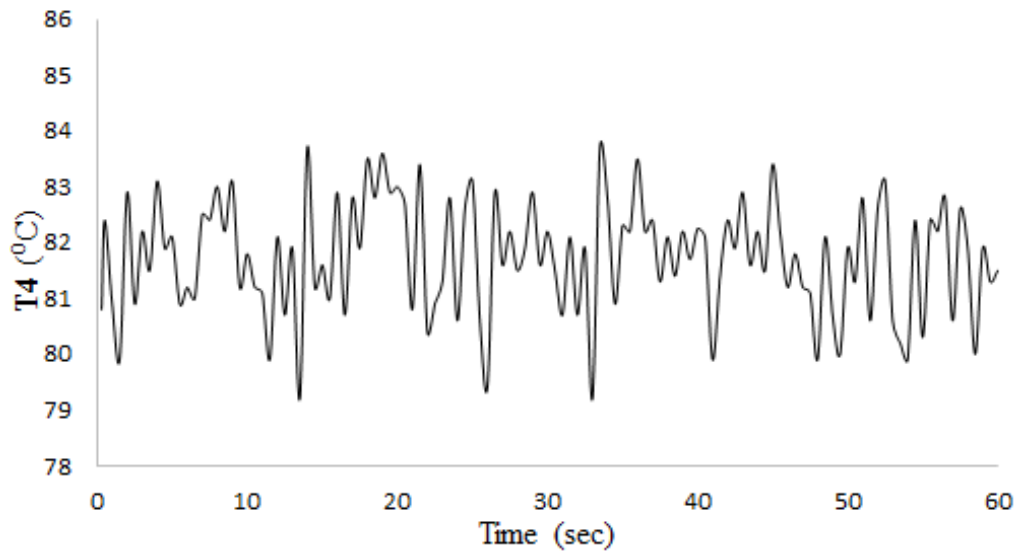
Figure 4.6 compares formation of such abnormal vapor plugs with normal plugs. Formation of abnormal vapor plugs had adverse effect on the fluid flow in the PHP which decreases performance of the PHP. After observing results of simulations for volume fraction contours and temperature time series, many of them were discarded and those that seem to have proper behavior used for further investigation of chaotic flow.

4.2.1 Non-linear temperature oscillations

The non-linear time series analysis is a popular method for investigation of complicated dynamical systems. Different non-linear analytical approaches, including power spectrum density, correlation dimensions, and autocorrelation function have been employed to analyze the temperature time series at adiabatic wall. Temperature behavior of adiabatic wall in a PHP is one of the most important factors to investigate chaos in the PHP. It can be seen in Figure 4.1 that there are 21 points on the wall of the PHP assigned for temperature measurements. Eight points are located at the adiabatic section and thirteen points are located at evaporator. Then, there are eight choices to observe temperature behavior of adiabatic wall. Figure 4.7 illustrates the temperature oscillations of point #4 and #18 on the adiabatic wall and evaporator respectively on the PHP under operating condition mentioned in Figure 4.4. Point selection at adiabatic section and evaporator was done randomly.



(a)



(b)

Figure 4.7. Temperature oscillations at evaporator (a) and adiabatic wall (b)

It is obvious that aperiodic, irregular, non-linear and complex time series of temperature are obtained for both evaporator and adiabatic wall. Evaporator temperature oscillations have higher amplitude and higher mean temperature comparing with adiabatic wall temperature oscillations. As mentioned earlier only adiabatic wall temperature behavior has been considered for chaos investigation purpose. To reach this aim, power spectrum density analysis has been applied to the obtained time series of adiabatic wall temperature. The PSD is the average of the Fourier transform magnitude squared over a large time interval.

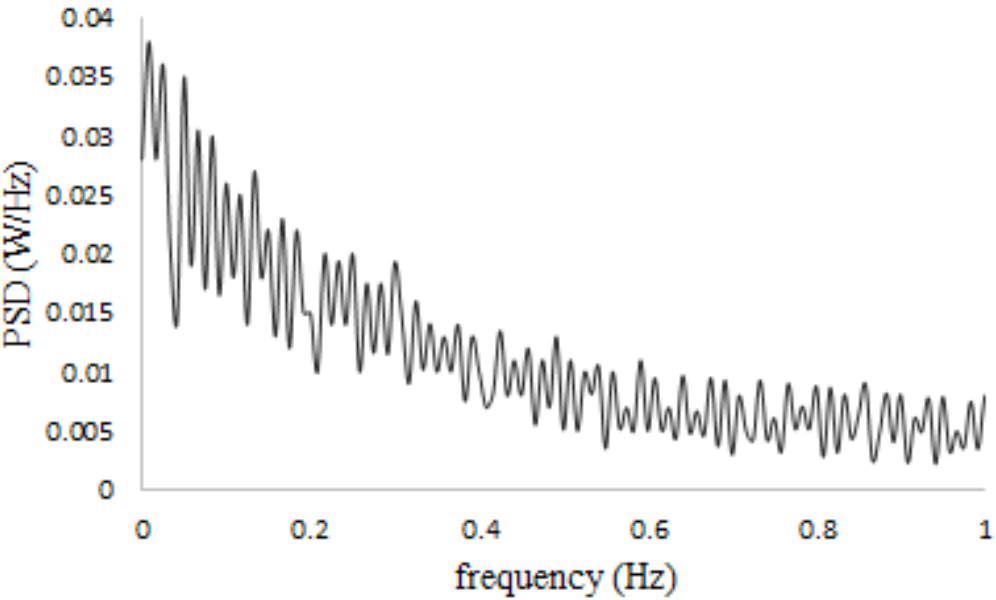


Figure 4.8. Power spectrum density of the adiabatic wall temperature time series (point #4)

Figure 4.8 shows the power spectrum density of the time series for the temperature on the adiabatic wall by Matlab analysis. Absence of dominating peaks in power spectrum density behavior and its decay by increasing the frequency were signatures of chaotic state in the PHP under such operating conditions. Important approaches such correlation dimension and autocorrelation function were employed to investigate the chaotic state afterwards. More details of the calculations in the mentioned approaches can be found in the references [60-62].

4.2.2 Correlation dimension and Autocorrelation function

Finding the correlation dimension for a chaotic process from the time series data set is usually applied for getting information about the nature of the dynamical system. Correlation dimension is popular because of its simplicity and flexibility data storage requirements. It is an alternate definition for true dimension or fractal dimension [61]. Time series data set can reconstruct phase space formed by the trajectories of the system, the attractor.

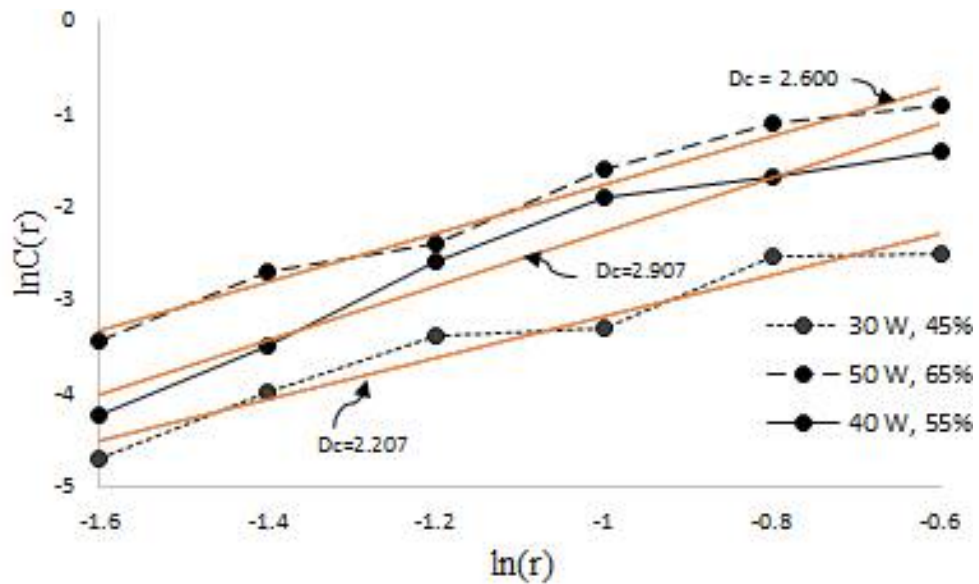


Figure 4.9. Correlation dimension values (D_c)

Figure 4.9 illustrates the correlation dimension for evaporator heating powers of 30 W, 40 W and 50 W with filling ratios of 45%, 55% and 65%, respectively at condenser temperature of 35 °C. Values of 2.207, 2.600 and 2.907 were obtained for correlation dimension. It is evident that by increasing the evaporator heating power and filling ratio, the slope of the curves and correlation dimension increase. High values of correlation dimension refers to high frequency, small scale temperature oscillations, caused by miniature bubbles or short vapor plugs dynamically flowing in PHP tubes [61]. The lower correlation dimension corresponds to low frequency of temperature oscillations and large amplitude caused by large bubbles in the PHP.

The theoretical autocorrelation function is an important tool to describe the properties of a stochastic process. An important guide to the persistence in a time series is given by the series of quantities called the sample autocorrelation coefficients, which measure the correlation between observations at different times. The set of autocorrelation coefficients arranged as a function of separation in time is the sample autocorrelation function, or the ACF. ACF helps to determine how quickly signals or process change with respect to time and whether a process has a periodic component. Figure 4.10 illustrates the autocorrelation function (ACF) of time series at filling ratio of 65% and three evaporator heating powers of 30 W, 45 W and 60 W at condenser temperature of 35 °C.

Behavior of ACF indicates the prediction ability of the system [61]. The autocorrelation function will have its largest value of ACF=1 at $\tau=0$. Figure 10 shows that the autocorrelation function decreases with time. Decreasing of the ACF shows that the prediction ability is finite as a signature of chaos. It is obvious in Figure 4.10 by increasing the evaporator heating power, ACF decreases.

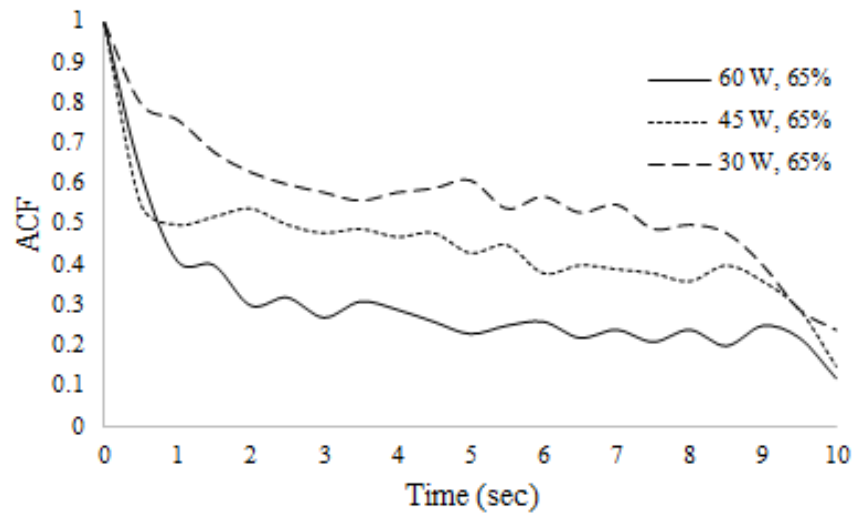
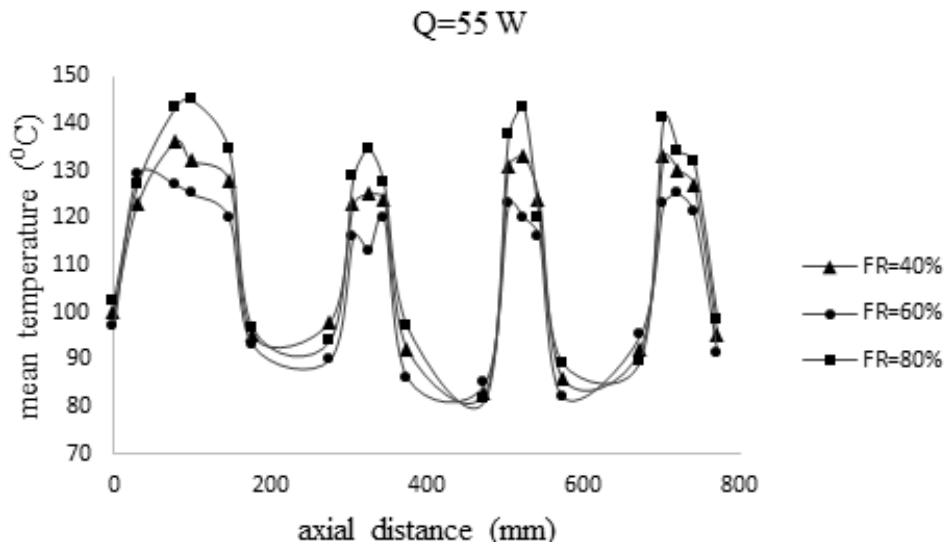
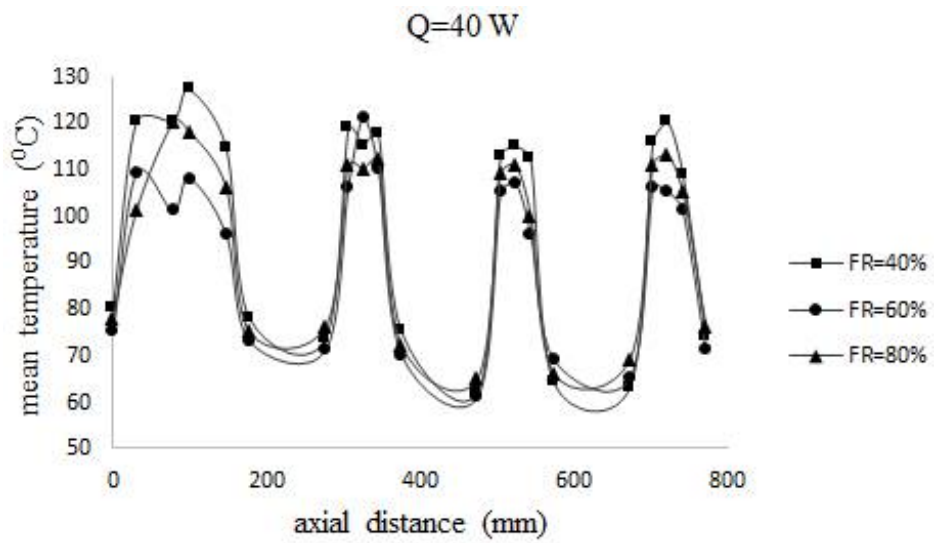


Figure 4.10. Autocorrelation function versus time

4.2.3 Thermal behavior



(a)



(b)

Figure 4.11. Axial mean temperature distribution for heating powers of 55 W (a) and 40 W (b)

For the traditional heat pipes, the filling ratio range of working fluid is lower comparing to the PHPs. Large amount of working fluid inside the channels causes liquid blockage and reduces pressure difference between heating and cooling sections which can stop the oscillation movement. But for the PHPs a higher filling ratio is required than traditional heat pipes. To investigate the effect of filling ration on the performance of PHP, several simulations were carried out under different heating powers, condenser temperatures and filling ratios. Figures 4.11a and 4.11b explain the axial temperature of the wall through the PHP. It should be noted that the relative distance for the point #1 is considered zero as the origin and the distance increases by moving downward from point #1 to #9. In addition, the temperature distributions in these figures do not include the condenser temperature since its value is known and constant. Temperature profiles have been illustrated at three different filling ratios of 40%, 60% and 80% under heating powers of 40 W and 55 W for evaporator and condenser temperature of 25 °C as part of numerical simulations. Mean temperature for each distance is defined as the average of data points from 0 to 60 seconds on that distance.

Generally these temperature distributions were symmetric from point #2 to #3, #4 to #5, #6 to #7 and #20 to #21 for vertical centerlines at #17, #18, #19 and #18 respectively. It was found that for all the heating powers, the mean temperatures in the evaporator had its lowest values at the filling ratio of 60%. It is obvious that at higher filling ratio of 80% and lower filling ratio of 40%, the evaporator mean temperatures have higher values comparing to that of 60%. Then based on the numerical simulation results, filling ratio of 60% was found as optimal filling ratio for the thermal performance of the PHP.

The overall thermal resistance of a PHP is defined as the difference average temperatures between evaporator and condenser divided by the heating power. For evaporator average temperature, thirteen points from #9 to #21 were used to calculate the average temperature. Since condenser has constant temperature, calculation is not necessary to get the average temperature which is equal to that constant value. Equation 4.12 defines the thermal resistance of a PHP.

$$R = \frac{T_e - T_c}{Q} \quad (4.1)$$

where T_e is the evaporator average temperature, T_c is the condenser average temperature and Q is the evaporator heating power.

Figure 4.12 describes behavior of thermal resistance with respect to evaporator heating power at recommended optimal value of 60% for filling ratio and condenser temperature of 25 °C. By increasing the heating power from 10 to 40 W, the thermal resistance decreases sharply. From 40 to 45 W, thermal resistance has slight decrease and remains almost constant about 1.62 °C/W at heating power of 45 W. Then thermal resistance starts to increase by increasing the heating power afterwards. It was seen that the PHP has its lowest thermal resistance of 1.62 °C/W at evaporator heating power of 45 W. It should be noted that the thermal resistance depends on many parameters such as PHP

structure, working fluid and operating conditions. Thus, obtained values in this paper are suitable for the test case in current study. But it can be concluded that there are optimal filling ratios and minimum thermal resistance at any test case which can be obtained by numerical or experimental investigations.

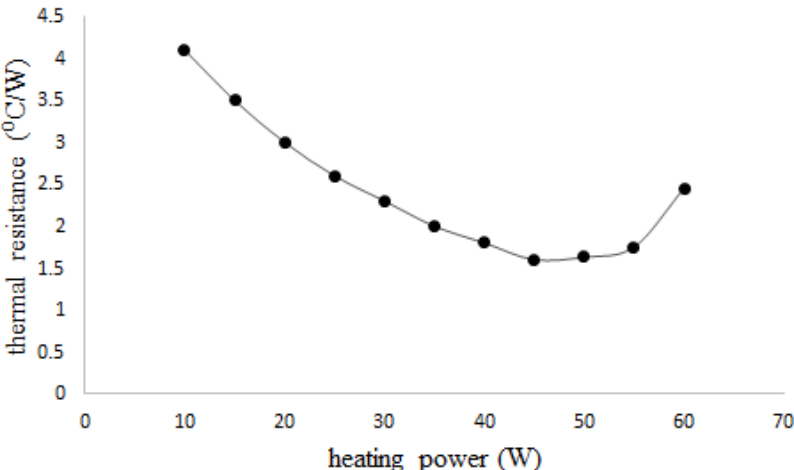


Figure 4.12. Thermal resistance versus heating power

4.3 Conclusion

Numerical simulations have been implemented to investigate the chaotic and thermal behavior of a closed-loop pulsating heat pipe. Heat flux and constant temperature boundary conditions were applied for evaporator and condenser respectively. Investigations have been conducted over several operating conditions. Volume fraction results showed formation of perfect vapor and liquid plugs in the fluid flow of PHP. Non-linear time series analysis, Power spectrum density, Correlation dimension and Autocorrelation were used to investigate chaos. Chaotic behavior was observed under several operating conditions. An optimal filling ratio and minimum thermal resistance were found for better thermal performance of the pulsating heat pipe.

Chapter 5

Nonlinear analysis of chaotic flow in a 3D closed-loop pulsating heat pipe

Numerical simulation has been conducted for the chaotic flow in a 3D closed-loop pulsating heat pipe (PHP). Heat flux and constant temperature boundary conditions have been applied for evaporator and condenser sections, respectively. Water and ethanol were used as working fluids. Volume of Fluid (VOF) method has been employed for two-phase flow simulation. Spectral analysis of temperature time series was carried out using Power Spectrum Density (PSD) method. Existence of dominant peak in PSD diagram indicated periodic or quasi-periodic behavior in temperature oscillations at particular frequencies. Correlation dimension values for ethanol as working fluid was found higher than that for water under the same operating conditions. Similar range of Lyapunov exponent values for the PHP with water and ethanol as working fluids indicated strong dependency of Lyapunov exponent to the structure and dimensions of the PHP. An O-ring structure pattern was obtained for reconstructed 3D attractor at periodic or quasi-periodic behavior of temperature oscillations. Minimum thermal resistance of 0.85 °C/W and 0.88 °C/W were obtained for PHP with water and ethanol as working fluids respectively. Simulation results showed good agreement with experimental results from other work under the same operating conditions.

5.1 Physical Modeling

A schematic cross sectional view of the 3D PHP is shown in Figure 5.1. In order to validate the simulation results of current study with an experimental test case, the structure and dimensions of the pulsating heat pipe in simulation were considered the same as experimental investigation in [64]. The diameter of the tube is 1.8 mm. The lengths of the evaporator, adiabatic and condenser sections are 60 mm, 150 mm and 60 mm, respectively. Water and ethanol were used as working fluids. Different evaporator heating powers and filling ratios were tested for the numerical simulation. There are 25 points in Figure 5.1 highlighted with bold rectangles and these points are assigned for temperature measurement during numerical simulation.

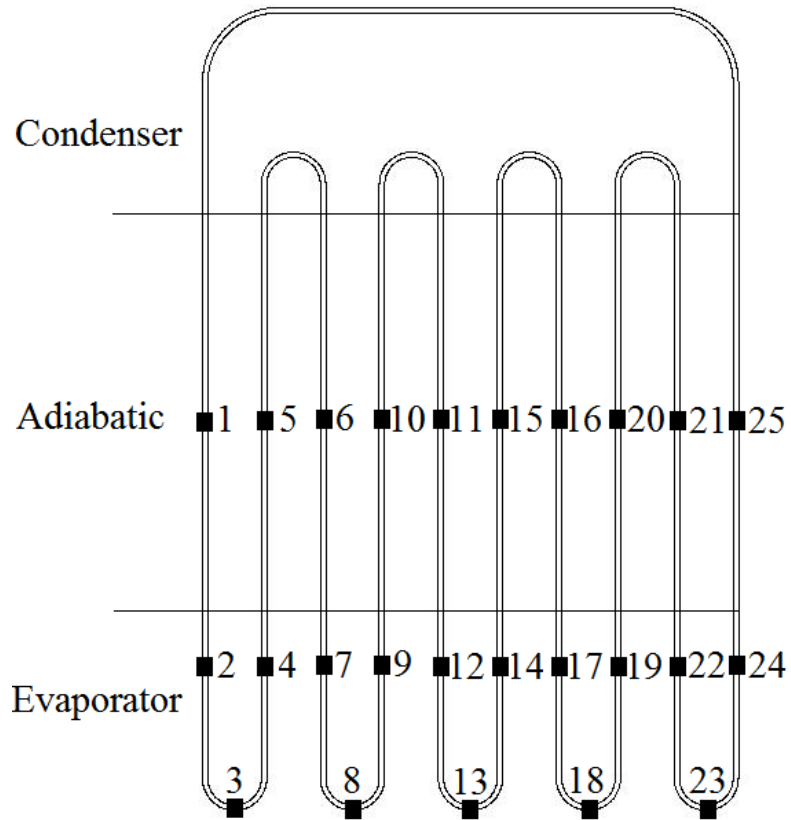


Figure 5.1. Schematic cross sectional view of the 3D PHP

Figure 5.2 shows cross sectional profile of meshing configuration used in the numerical simulation. This profile has been swept through the entire centerline of the PHP led to create hexahedral meshes. Surface tension is an important factor in the performance of the pulsating heat pipe. Employing quadrilaterals or hexahedrals meshes for numerical simulation leads to more accurate results in case of surface tension than those of triangular and tetrahedral. The hexahedral mesh was used for the entire pulsating

heat pipe. It is evident in Figure 5.2 that number of layers are increased near the wall of the PHP to properly capture the flow gradients.

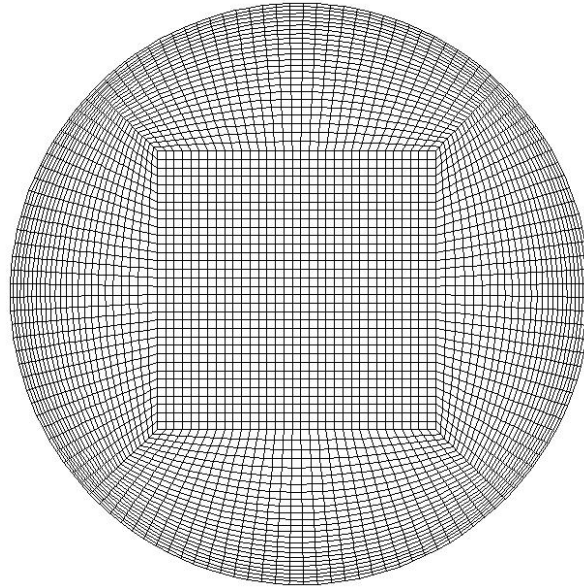


Figure 5.2. Meshing configuration

Volume of Fluid (VOF) method has been applied for two phase flow simulation. The volume of fluid method is a free-surface modelling technique, i.e. a numerical technique for tracking and locating the free surface (or fluid-fluid interface). It belongs to the class of Eulerian methods which are characterized by a mesh that is either stationary or is moving in a certain prescribed manner to accommodate the evolving shape of the interface. VOF is an advection scheme and numerical recipe that allows tracking the shape

and position of the interface, but it is not a standalone flow solving algorithm. The Navier–Stokes equations describing the motion of the flow have to be solved separately. The same applies for all other advection algorithms. Applications of the VOF model include stratified flows, free-surface flows, filling, sloshing, the motion of large bubbles in a liquid, the motion of liquid after a dam break, the prediction of jet breakup (surface tension), and the steady or transient tracking of any liquid-gas interface. The related governing equations have been discussed in chapter 2 and 3.

5.2 Results and Discussions

As mentioned earlier, in order to validate the simulation results of current study with an experimental test case, the structure and dimensions of the pulsating heat pipe in simulation were considered the same as experimental investigation in [64]. In addition, the same working fluids of water and ethanol were employed. It should be noted that due to the experiment limitations as the mentioned investigation, the maximum heating power of 70 W and 60 W were applied for water and ethanol as working fluids respectively in [64]. Besides, constant temperature of 20 °C was used for the condenser boundary condition in the experiment. Figure 5.3 shows comparison of thermal resistance with respect to heating power between simulation results of current study and experimental results of Shafii et al. [64]. Thermal resistance behavior has been illustrated at filling ratios of 40% and 80% for water as working fluid and 40% and 70% for ethanol as working fluid. As seen in Figure 5.3a the thermal resistance obtained from simulation has higher values after heating power

of 10 W comparing with experimental results for water as working fluid and filling ratio of 80%. The maximum error occurs at heating power of 40 W which is almost 13%. The average error is 8.7 % under these operating conditions. At filling ratio of 40%, the maximum error occurs at heating power of 60 W which is almost 15%. The average error is 9.7% under these operating conditions. Figure 5.3b shows that the thermal resistance obtained from simulation has lower values for all heating powers comparing with experimental results for ethanol as working fluid and filling ratio of 70%. The maximum error occurs at heating power of 20 W which is almost 10%. The average error is 6.3 % under these operating conditions. At filling ratio of 40%, the maximum error occurs at heating power of 25 W which is almost 13%. The average error is 7.5% under these operating conditions. Figure 5.3 confirms there is a good agreement between simulation and experimental results. The range of errors percentage is normal for such comparison between simulation and experimental results. There are several source of error in any experiment such as instrument and measurement inaccuracy and uncertainty. One of the most important issues in this particular test case is insulation of evaporator and adiabatic sections which cannot be ideal experimentally. Thus, ideal insulation in numerical simulation is one of the significant reasons which causes differences between simulation and experimental results.

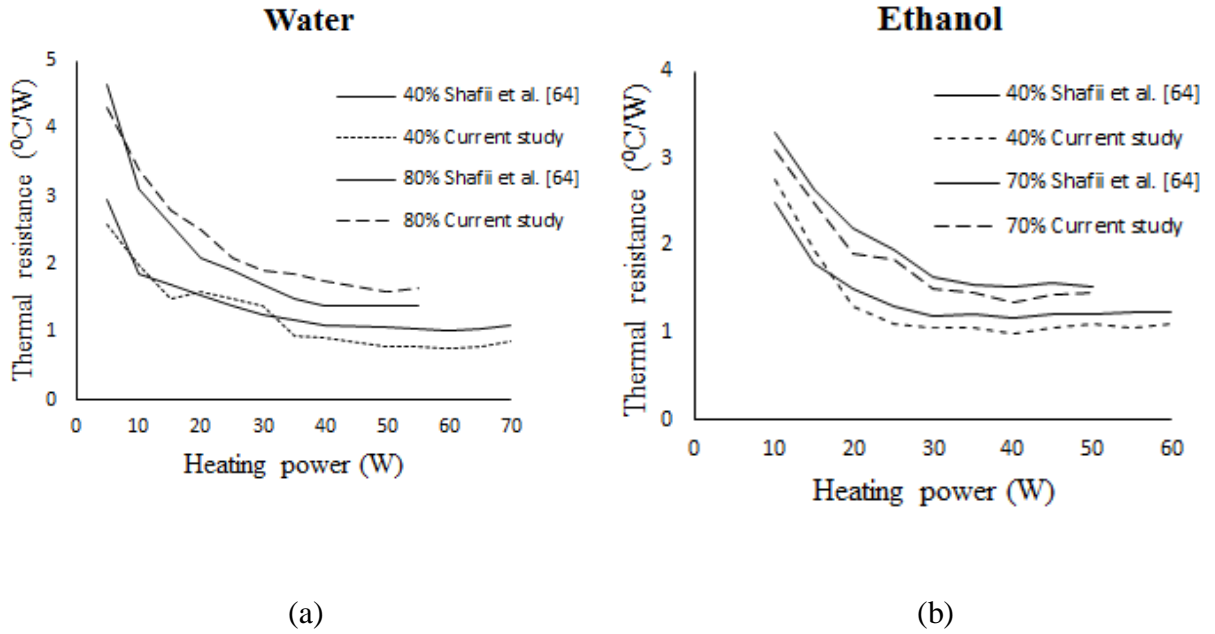


Figure 5.3. Comparison of thermal resistance versus heating power between simulation results of current study and experimental results of reference [64]

5.2.1 Volume Fractions

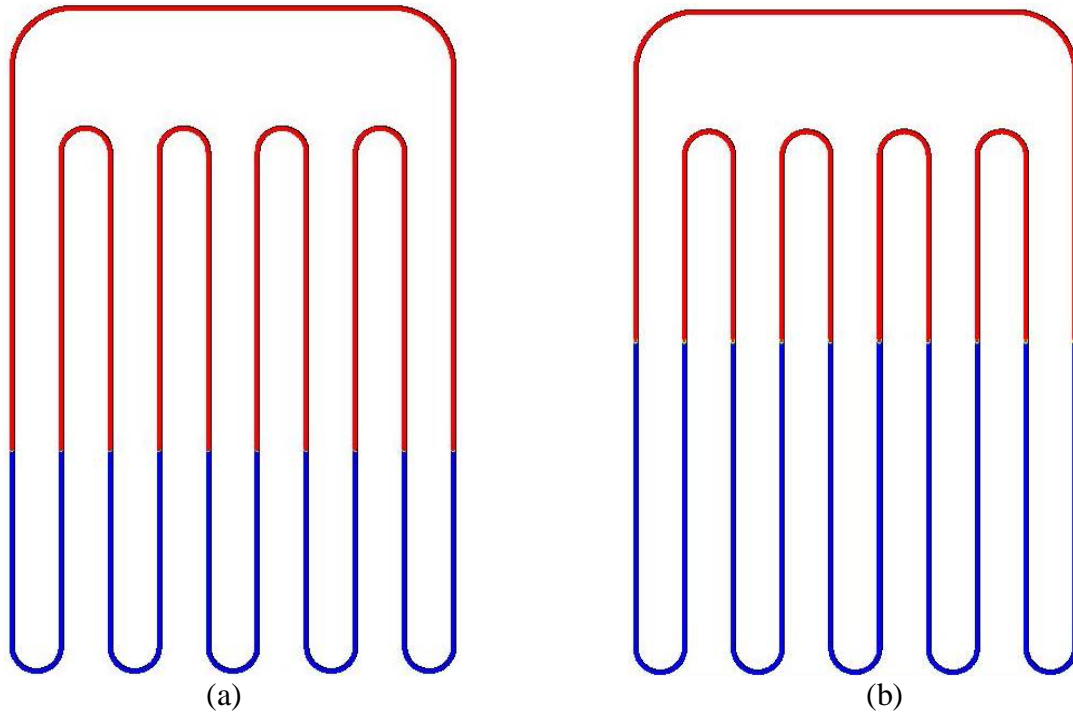


Figure 5.4. Volume fractions of liquid and vapor at $t=0.1$ s under heating power of 70 W and condenser temperature of 20 °C for ethanol, FR of 40% (a) and water, FR of 65% (b)

Figures 5.4 to 5.8 illustrate volume fractions of liquid and vapor at different times (red color represents the vapor and blue color represents the liquid) under different operating conditions. Figure 5.4a shows almost the initial condition of the PHP with

ethanol as working fluid and filling ratio of 40%. Figure 5 demonstrates formation of vapor bubbles and fluid flow development in the PHP. Figure 6 depicts the volume fractions of liquid and vapor in the PHP after the fluid flow has been established. Mostly a similar process occurs in the PHP with water as working fluid and filling ratio of 65% (Figures 5.4b, 5.7 and 5.8). One of the most significant effects due to increasing filling ratio is pressure increase in the PHP which leads to a longer time duration for boiling to start (because of increasing the saturated temperature) and slower flow motion in the PHP. In addition to higher filling ratio, due to higher specific heat and higher saturation temperature for water comparing to ethanol, boiling process starts later for the PHP with water as working fluid than PHP with ethanol as working fluid. The effect of change in filling ratio on the chaotic and thermal behavior of the PHP will be investigated in the next subsections afterwards. It is evident that liquid plugs having menisci on the plug edges are formed due to surface tension forces. A liquid thin film also exists surrounding the vapor plug. The angle of contact of the menisci, the liquid thin film stability and its thickness depends on the fluid-solid combination and the operating parameters which are selected. If a liquid plug is moving or tends to move in a specific direction then the leading contact angle (advancing) and the lagging contact angle (receding) will be different [51]. This happens because the leading edge of the plug moves on a dry surface (depending on the liquid thin film stability and existence) while the lagging edge moves on the just wetted surface. These characteristics can be observed in Figure 5.9, which shows a snapshot of liquid-vapor plugs as result of simulation in the vertical part of the system.

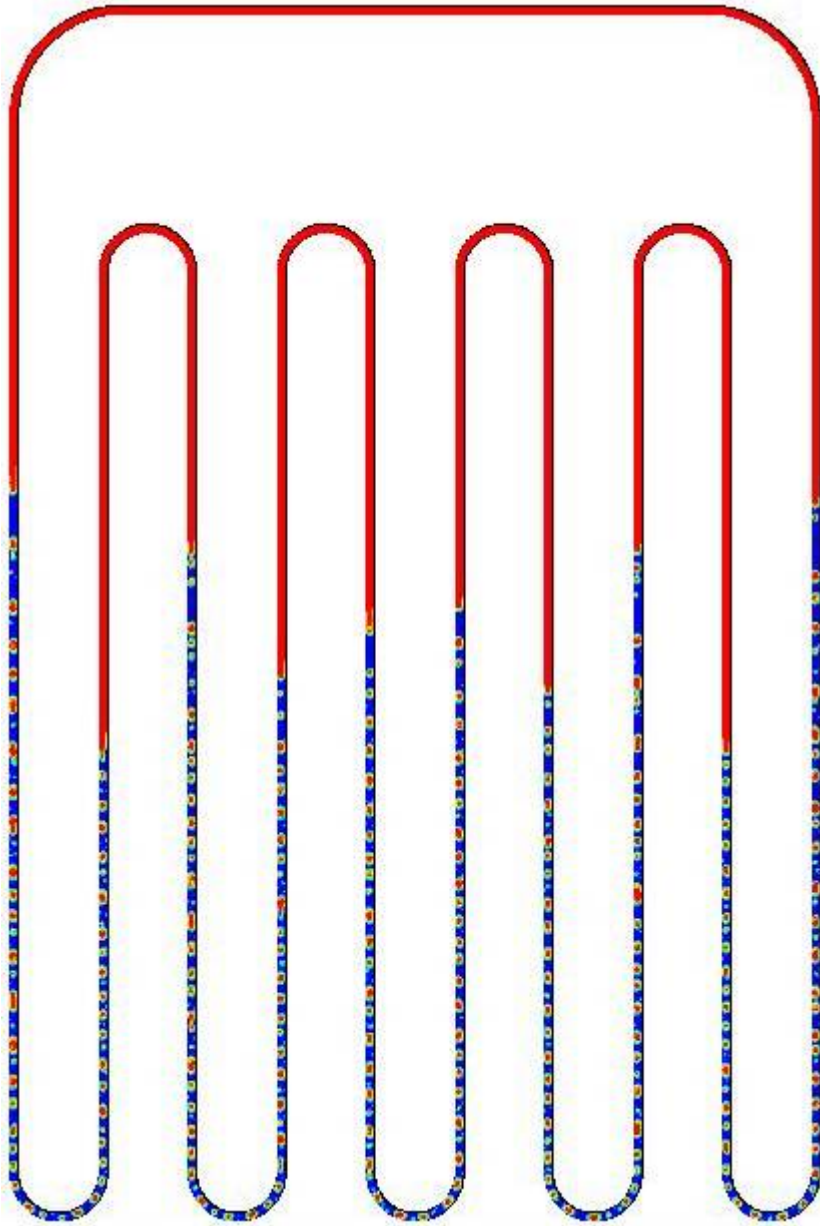


Figure 5.5. Volume fractions of liquid and vapor under heating power of 70 W and condenser temperature of 20 °C for ethanol as working fluid with FR of 40% at $t=0.8$ s

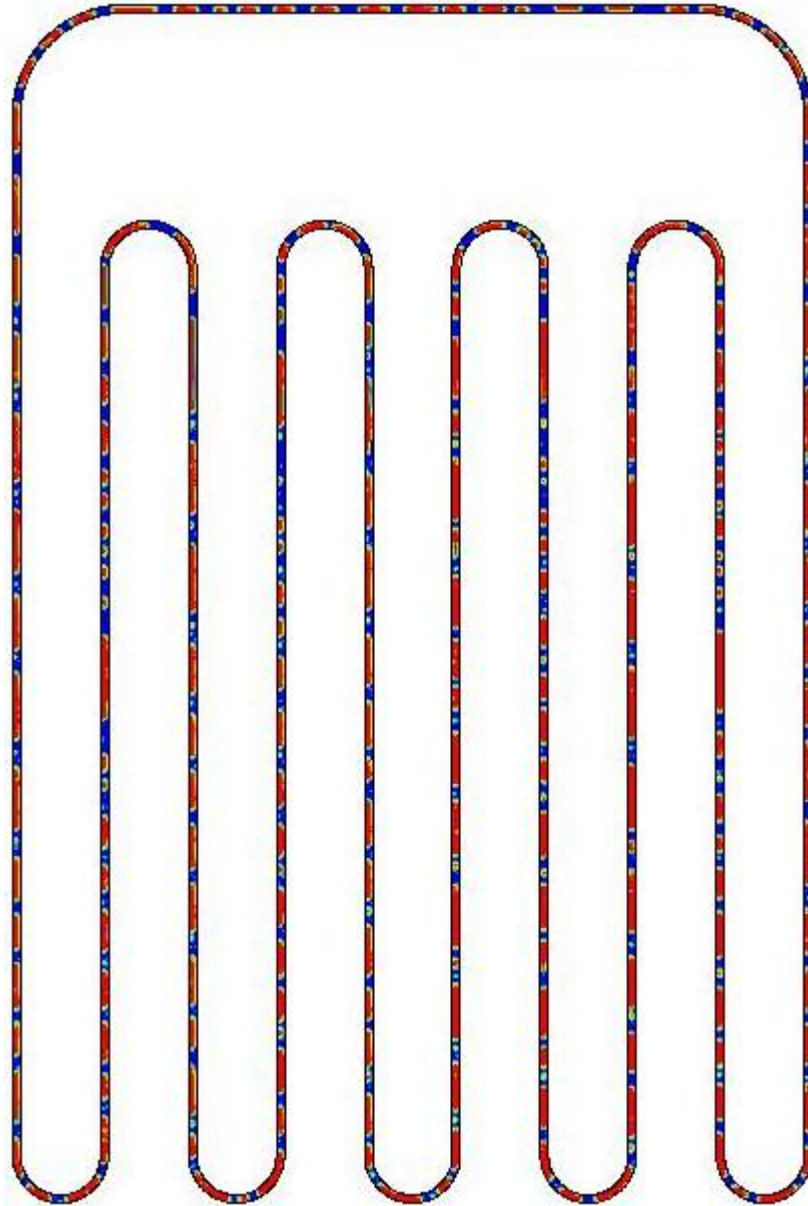


Figure 5.6. Volume fractions of liquid and vapor under heating power of 70 W and condenser temperature of 20 °C for ethanol as working fluid with FR of 40% at $t=20$ s

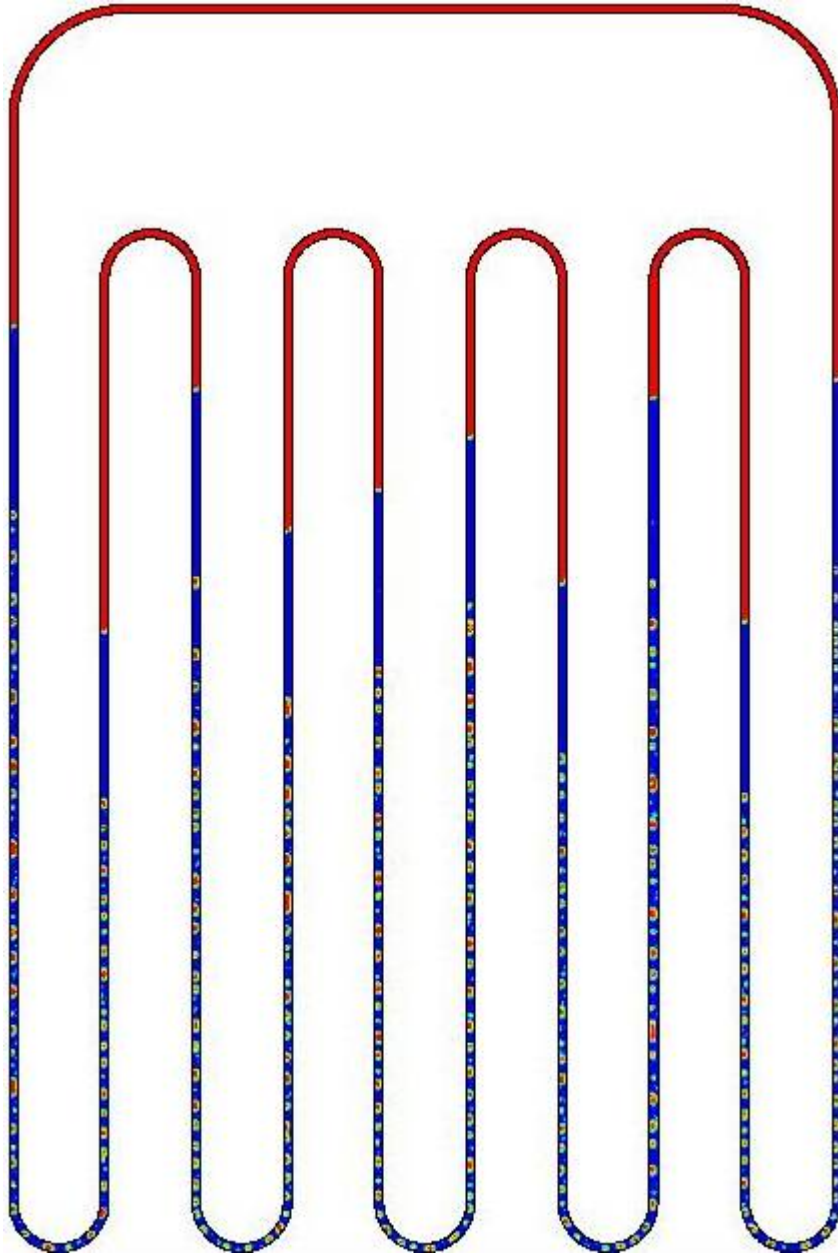


Figure 5.7. Volume fractions of liquid and vapor under heating power of 70 W and condenser temperature of 20 °C for water as working fluid with FR of 65% at $t=0.8$ s

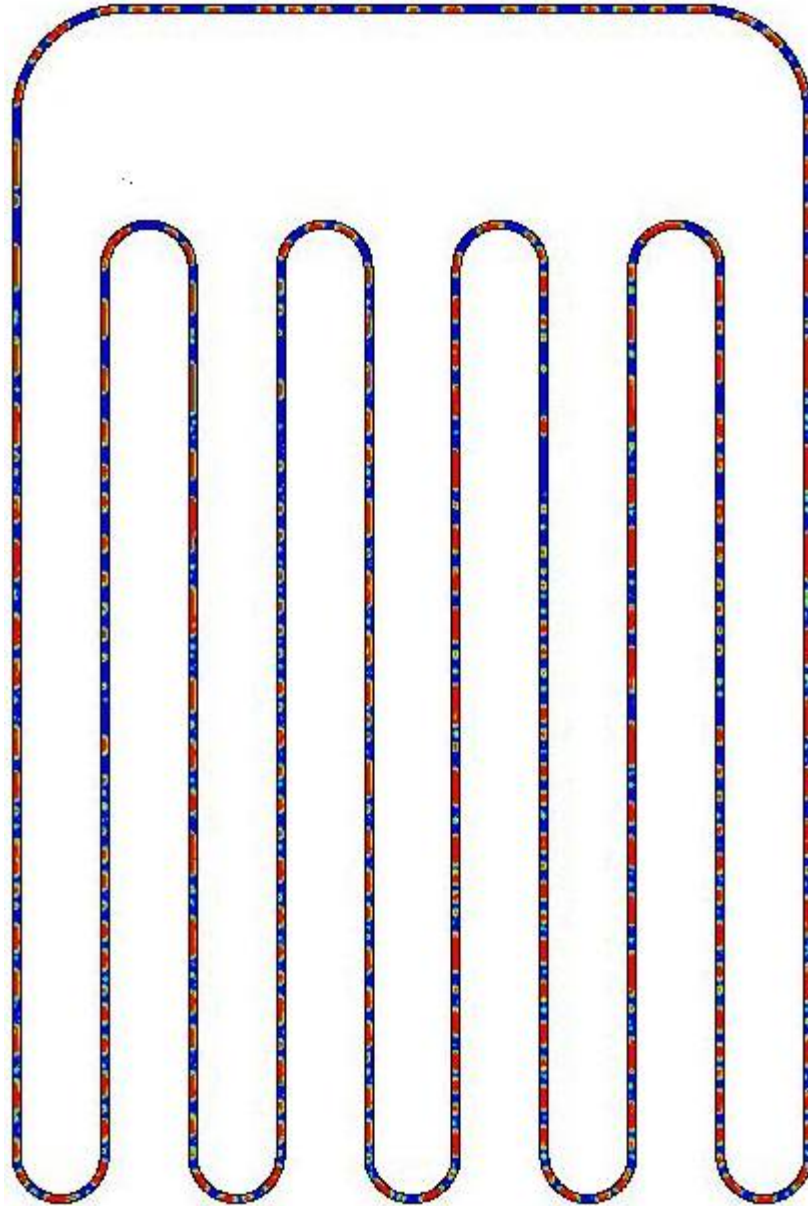


Figure 5.8. Volume fractions of liquid and vapor under heating power of 70 W and condenser temperature of 20 °C for water as working fluid with FR of 65% at $t=20$ s

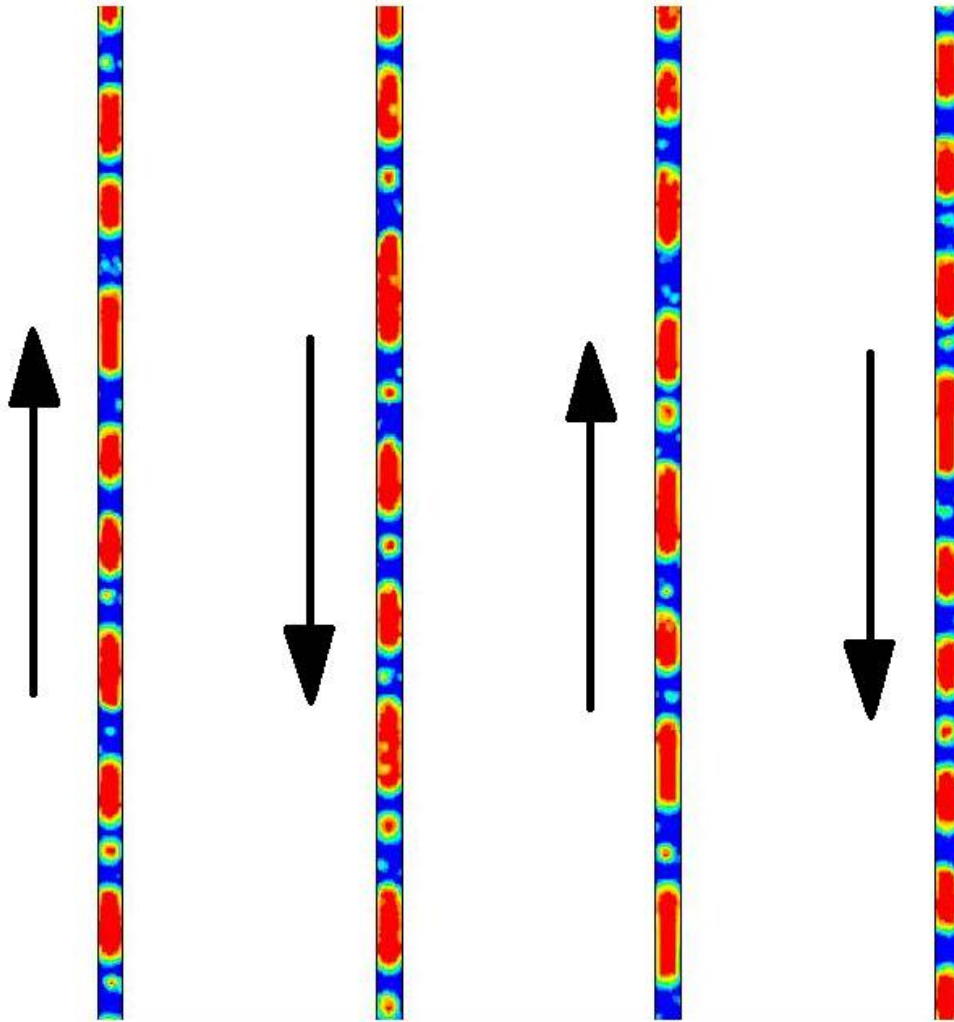


Figure 5.9. Vapor and liquid plugs in the PHP

The results showed that the fluid flow finally circulates in one direction (clockwise or counterclockwise) in the pulsating heat pipe. This direction is based on a random process and could be different even under the same operating and boundary conditions. The liquid and vapor plugs are subjected to pressure forces from the adjoining plugs.

Forces acting on the liquid plugs are due to the capillary pressures created by the menisci curvatures of the adjacent vapor bubbles. The liquid plugs and vapor bubbles experience internal viscous dissipation as well as wall shear stress as they move in the PHP tube [51]. The relative magnitude of these forces will decide the predominant force to be considered. The liquid and vapor plugs may receive heat, reject heat or move without any external heat transfer, depending on their location in the evaporator, condenser or the adiabatic section. Probability of events frequently places vapor bubbles in direct contact with the evaporator tube surface. In this case saturated vapor bubbles receive heat which is simultaneously followed up by evaporation mass transfer from the adjoining liquid plugs thereby increase the instantaneous local saturation pressure and temperature.

Liquid thin film exists around the vapor plug, and the thickness of the liquid film may vary depending on some boundary conditions. One of the most important parameters affecting the liquid film is the wall temperature in the PHP. Since evaporator, condenser and adiabatic sections have different working temperatures, liquid film with different thicknesses may form in these regions [50]. Figure 5.10 shows different liquid films surrounding the vapor plugs with different thicknesses as result of simulation. Figure 5.10 illustrates vapor plugs in the evaporator (a), adiabatic section (b) and condenser (c) respectively. It can be seen that by decreasing the wall temperature from evaporator to condenser, the liquid film thickness increases.

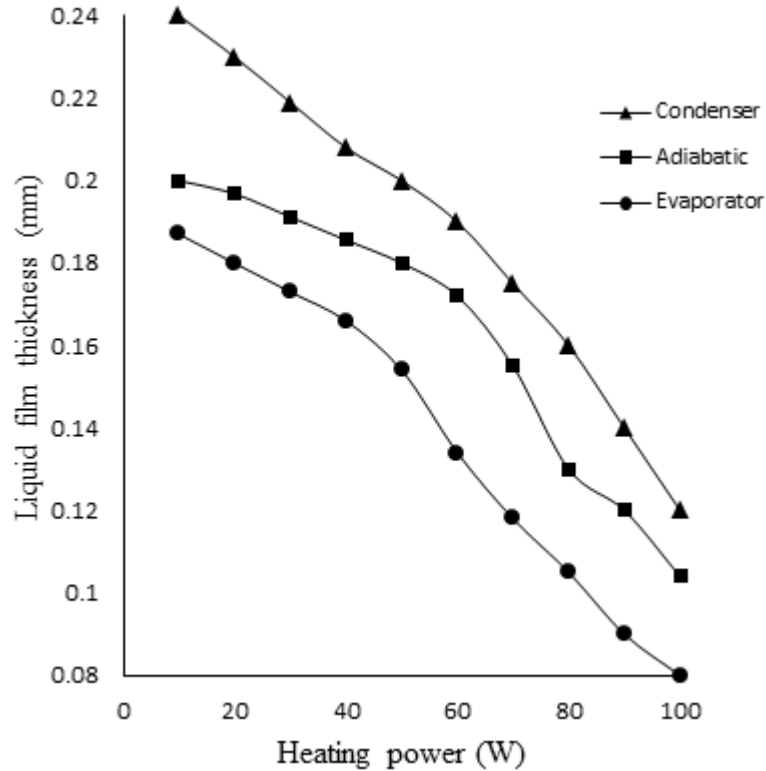


Figure 5.11. Liquid film thickness versus heating power

In adiabatic section, while passing from the evaporator to the condenser, the train of vapor-liquid plugs is subjected to a series of complex heat and mass transfer process. Essentially non equilibrium conditions exist whereby the high pressure, high temperature saturated liquid-vapor plugs is brought down to low pressure, low temperature saturated conditions existing in the condenser. Internal enthalpy balancing in the form of latent heat takes place by evaporation mass transfer from the liquid to the vapor plugs whereby saturation conditions are always imposed on the system during the bulk transient in the adiabatic section [50]. Sometimes two vapor bubbles combine together to form a larger

vapor slug [51]. Such a combination process in evaporator and adiabatic section is illustrated in Figure 5.12 as a result of simulation; this phenomenon mostly was observed in the adiabatic section and was observed rarely in the condenser.

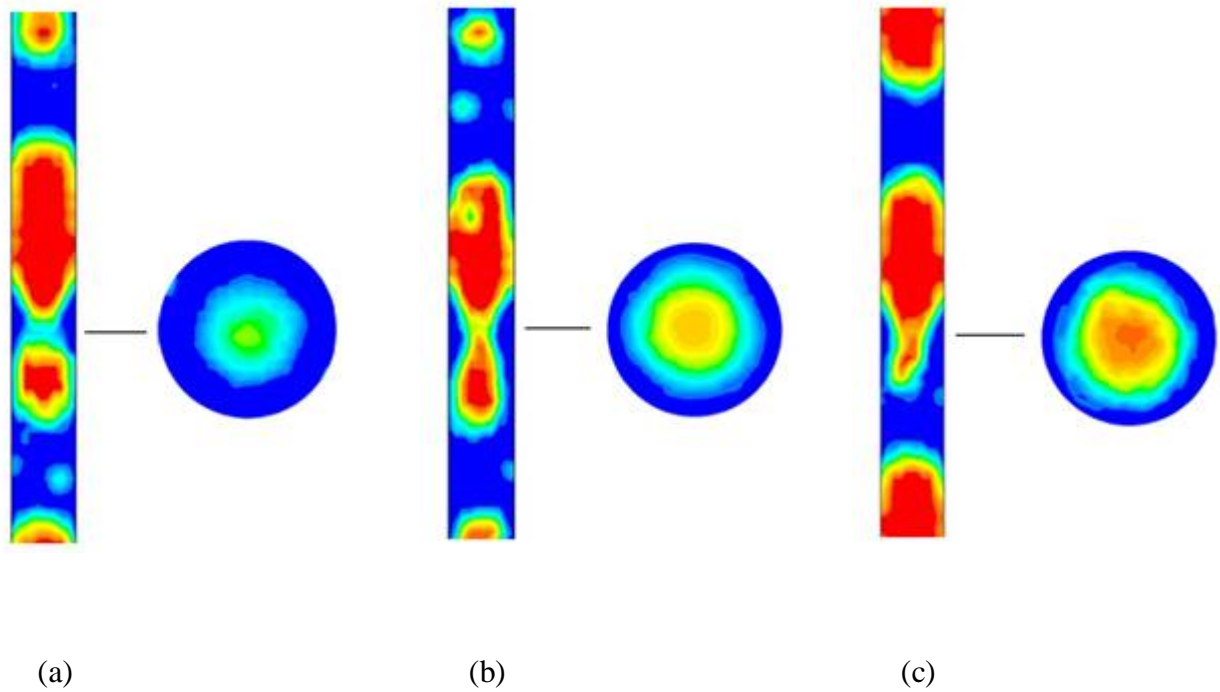


Figure 5.12. Vapor bubbles combination

After volume fractions investigation, important approaches such spectral analysis, correlation dimension, autocorrelation function, Lyapunov exponent and phase space

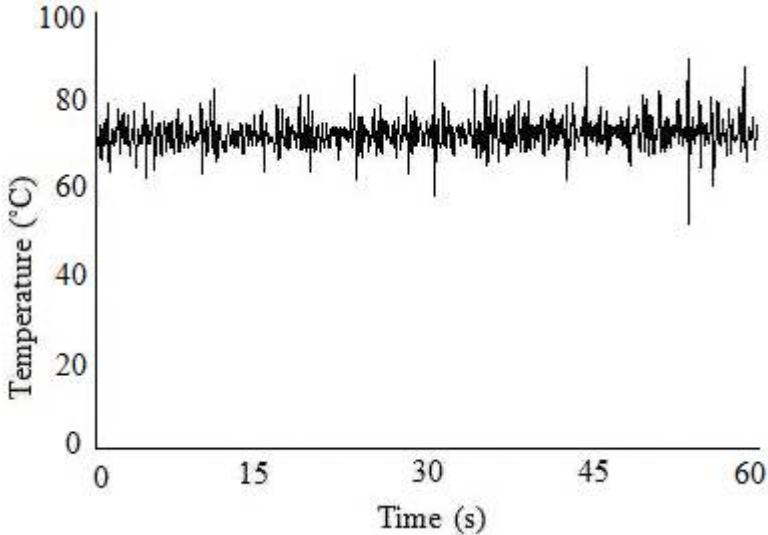
reconstruction were employed to investigate the chaotic state in the PHP. More details of the calculations in these approaches can be found in the references [60-62].

5.2.2 Spectral Analysis of Time Series

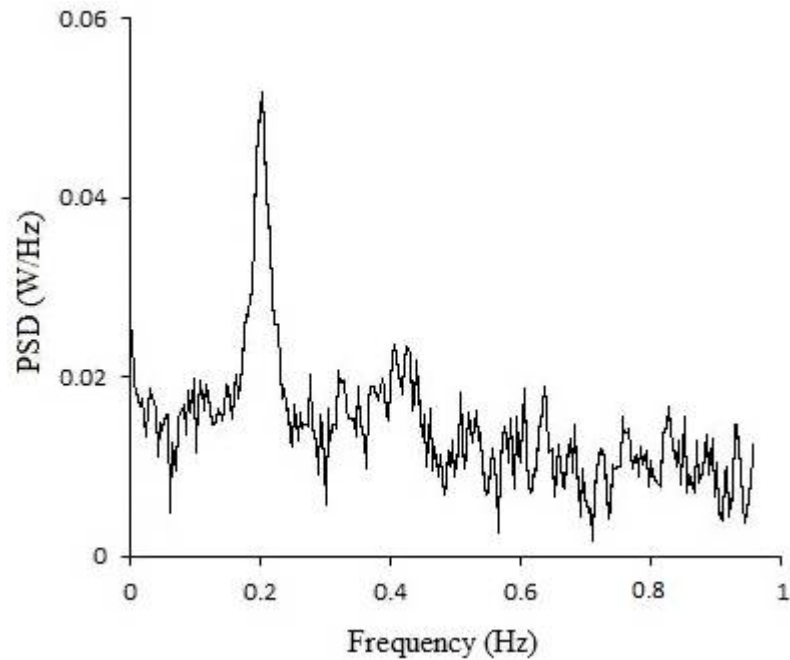
Temperature behavior of adiabatic wall of PHP is one of the most important factors to investigate chaos in the system. Thus, temperature time series analysis of the adiabatic wall is significant and crucial to analyze the chaotic state in a PHP. Recently there have been experimental studies that reported the existence of chaos in PHPs under some operating conditions. The approach in these studies is to analyze the time series of fluctuation of temperature of a specified location on the PHP tube wall (adiabatic section) by power spectrum calculated through Fast Fourier Transform (FFT) [51]. In this work, 10 points on the PHP are dedicated to measure the temperature of the adiabatic walls as shown in Fig. 1. To investigate and analyze the temperature time series, Power Spectrum Density (PSD) approach has been employed. The power spectrum of a time series describes the distribution of power into frequency components composing that signal. According to Fourier analysis any physical signal can be decomposed into a number of discrete frequencies or a spectrum of frequencies over a continuous range. The statistical average of a certain signal or sort of signal (including noise) as analyzed in terms of its frequency content is called its spectrum.

The power spectrum density is particularly useful for studying the oscillations of a system. There will be sharper or broader peaks at the dominant frequencies and at their

integer multiples, the harmonics. Periodic or quasi-periodic signals show sharp spectral lines. Measurement noise adds a continuous floor to the spectrum. Thus in the spectrum, signal and noise are readily distinguished. Deterministic chaotic signals may also have sharp spectral lines but even in the absence of noise there will be a continuous part of the spectrum [60]. This is an immediate consequence of the exponentially decaying of autocorrelation function that will be shown in the next sections afterwards. The spectral analysis of the times series was carried out using Matlab codes in this paper.



(a)

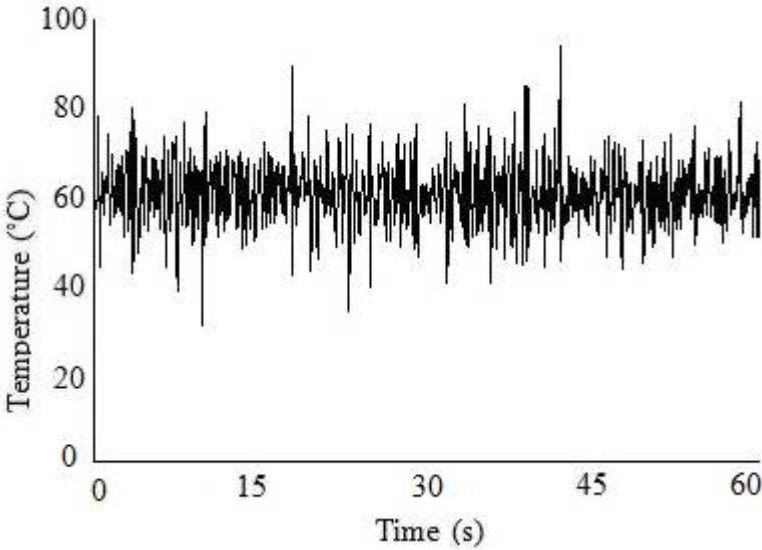


(b)

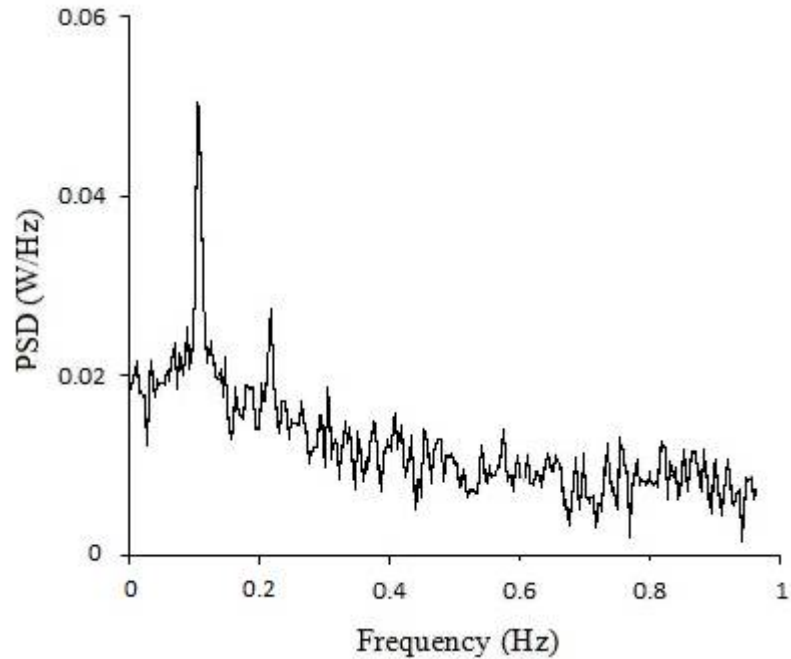
Figure 5.13. Time series of temperature (a) and PSD diagram (b) for point #16 under heating power of 90 W, condenser temperature of 20 °C, filling ratio of 45% and water as working fluid

Figure 5.13 shows the time series of the adiabatic wall temperature at point #16 under heating power of 90 W, condenser temperature of 20 °C, filling ratio of 45% and water as working fluid and its power spectrum density diagram. The spectral analysis of the time series in Figure 5.13b indicates a dominant peak around frequency of 0.2 Hz. This

signifies an intense periodic or quasi-periodic oscillation of temperature at this dominant frequency with PSD of 0.05 (W/Hz). PSD of oscillations at other frequencies are in an order to be neglected comparing with this dominant peak. Thus, the temperature behavior in Figure 5.13a can be classified as periodic or quasi-periodic with frequency of 0.2 and PSD of 0.05 under mentioned operating conditions.



(a)

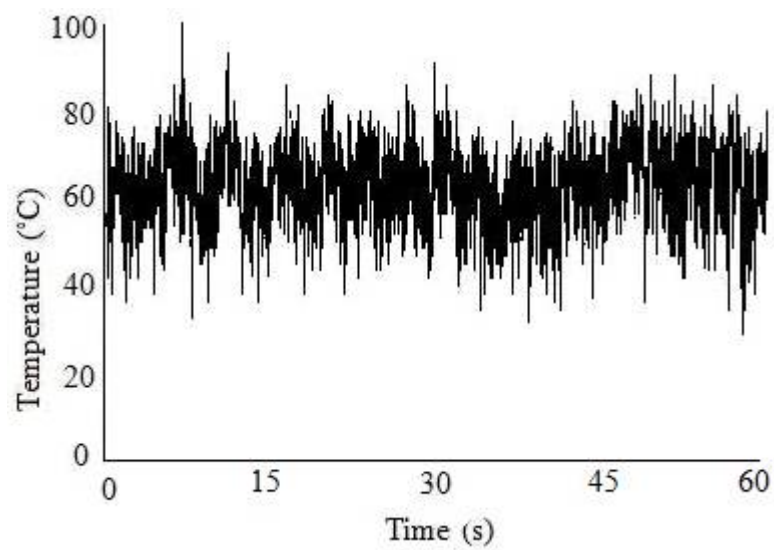


(b)

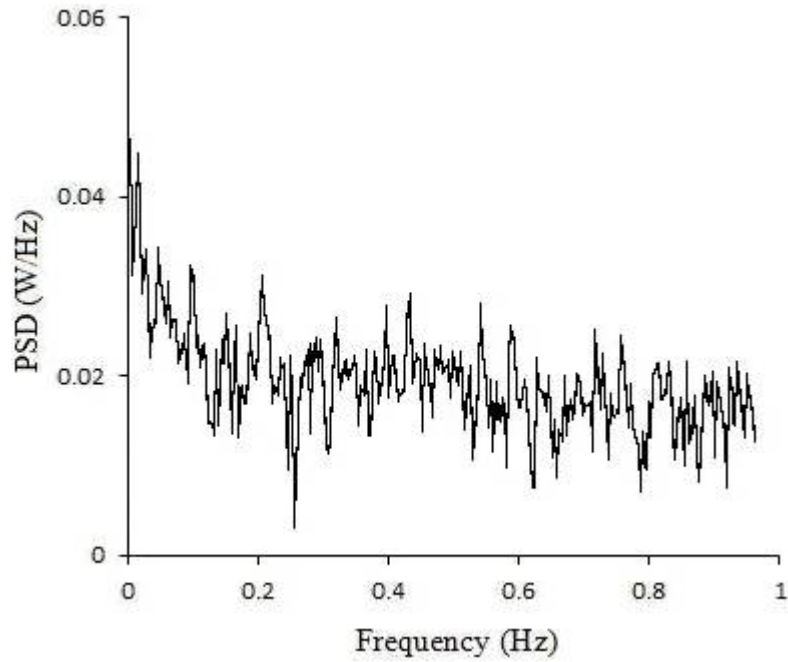
Figure 5.14. Time series of temperature (a) and PSD diagram (b) for point #11 under heating power of 90 W, condenser temperature of 20 °C, filling ratio of 55% and ethanol as working fluid

Figure 5.14 shows the time series of the adiabatic wall temperature at point #11 under heating power of 90 W, condenser temperature of 20 °C, filling ratio of 55% and ethanol as working fluid and its power spectrum density diagram. It can be seen in Figure 5.14b that there are two dominant peaks in PSD diagram. Oscillations at frequencies of 0.12 Hz and 0.23 Hz have higher PSD of 0.05 and 0.03 (W/Hz) comparing oscillations at

other frequencies. Existence of these two dominant peaks signifies periodic or quasi-periodic oscillations of temperature at these dominant frequencies. Thus, the temperature behavior in Figure 5.14a cannot be classified as chaos under the mentioned operating conditions.



(a)

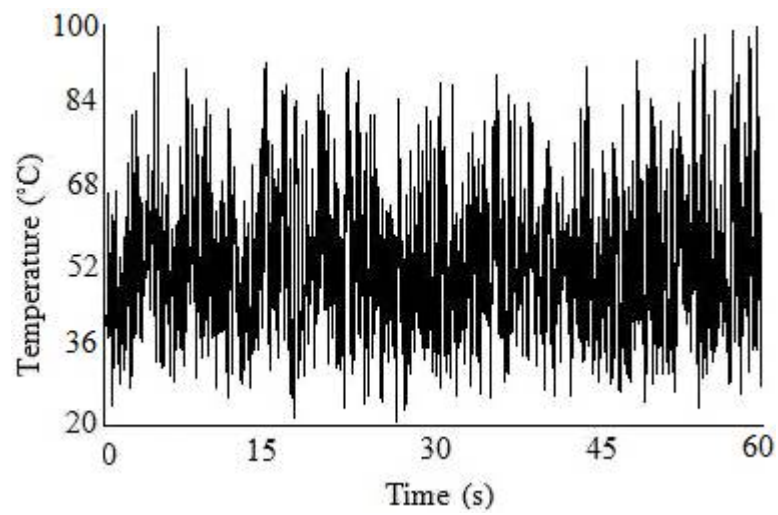


(b)

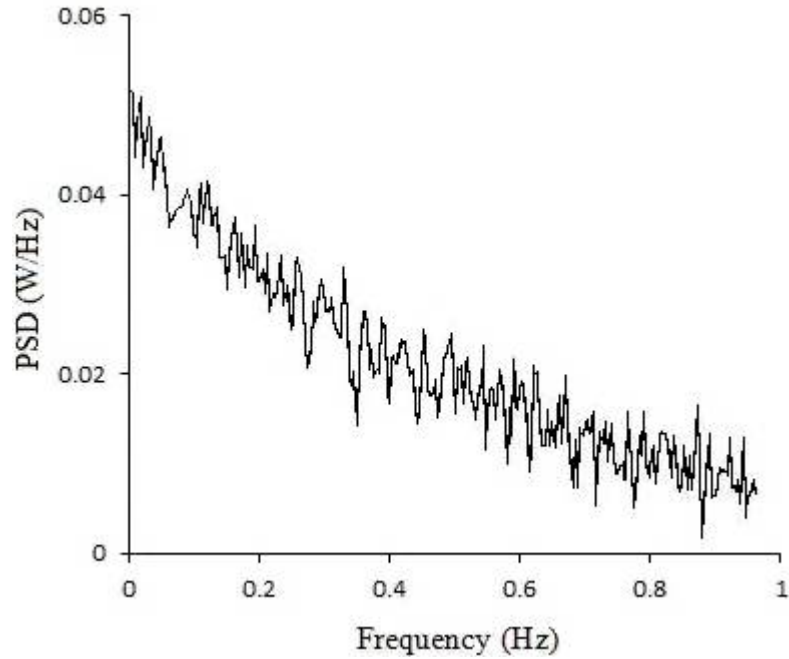
Figure 5.15. Time series of temperature (a) and PSD diagram (b) for point #20 under heating power of 90 W, condenser temperature of 20 °C, filling ratio of 70% and water as working fluid

Figure 5.15 shows the time series of the adiabatic wall temperature at point #20 under heating power of 90 W, condenser temperature of 20 °C, filling ratio of 70% and water as working fluid and its power spectrum density diagram. As shown in Figure 5.15b, there is not any significant and visible dominant peak in PSD diagram. At some frequencies, the PSD has higher value comparing other frequencies. But those higher

values of PSD are not in an order to be considered as a dominant peak. Thus, the temperature oscillations are neither periodic nor quasi-periodic. In addition, by increasing the frequency, the power spectrum density decays in Figure 5.15b as signature of chaotic behavior. Then, the temperature behavior in Figure 5.15a can be classified as chaos under mentioned operating conditions.



(a)



(b)

Figure 5.16. Time series of temperature (a) and PSD diagram (b) for point #25 under heating power of 90 W, condenser temperature of 20 °C, filling ratio of 65% and ethanol as working fluid

Figure 5.16 shows the time series of the adiabatic wall temperature at point #25 under heating power of 90 W, condenser temperature of 20 °C, filling ratio of 65% and ethanol as working fluid and its power spectrum density diagram. It is evident there is not any dominant peak in PSD diagram at all. Besides, the power spectrum density decays by frequency increment. Absence of dominant peak in PSD diagram and its decay with

respect to frequency indicate the chaotic state in the system. So, the temperature time series in Figure 5.16a can strongly be classified as chaos under mentioned operating conditions.

As mentioned earlier, there are 10 points assigned for adiabatic wall temperature measurement (#1, #5, #6, #11, #15, #16, #20, #21 and #25). Numerical simulations and analytical investigations concluded that if any of these points had periodic or quasi-periodic behavior, rest of the points (in adiabatic section) had periodic or quasi-periodic behavior in terms of temperature time series. This conclusion was also applicable for chaotic behavior of the temperature time series. Then, in order to investigate the chaotic behavior in the entire PHP, only selecting one point (in adiabatic section) was sufficient.

5.2.3 Correlation Dimension

In chaos theory, the correlation dimension is a measure of the dimensionality of the space occupied by a set of data points, often referred to as a type of fractal dimension. The correlation dimension is well known in fractal geometry and it is used to calculate a fractal dimension from a time series. The time series is embedded in n -dimensional space which is done by forming vectors of length n . The embedding dimension of an attractor dataset is the dimension of its address space. In other words, it is the number of attributes of the attractor dataset. The attractor dataset can represent a spatial object that has a dimension lower than the space where it is embedded [62]. For example, a line has an intrinsic dimensionality one, regardless if it is in a higher dimensional space. The intrinsic

dimension of an attractor dataset is the dimension of the spatial object represented by the attractor dataset, regardless of the space where it is embedded. The above definition of correlation dimension involves phase space vectors as the location of points on attractor. Thus, given a scalar time series, it is important to reconstruct an auxiliary phase space by an embedding procedure.

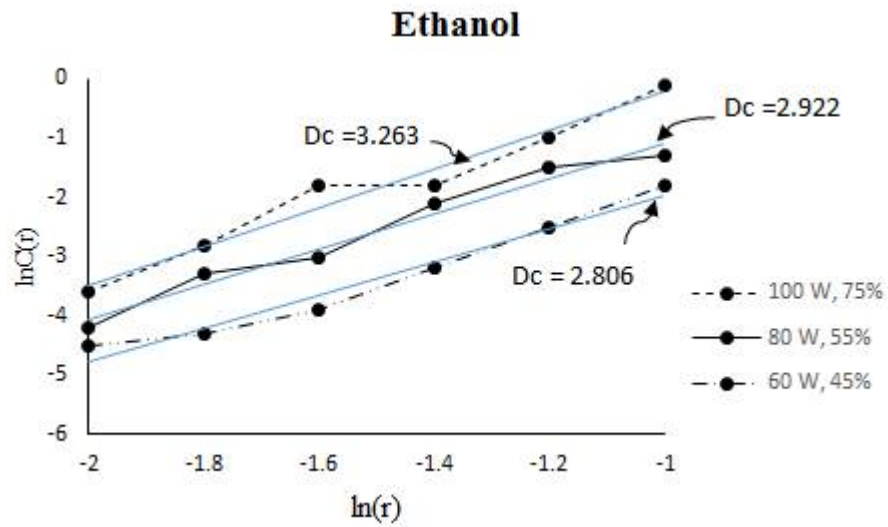
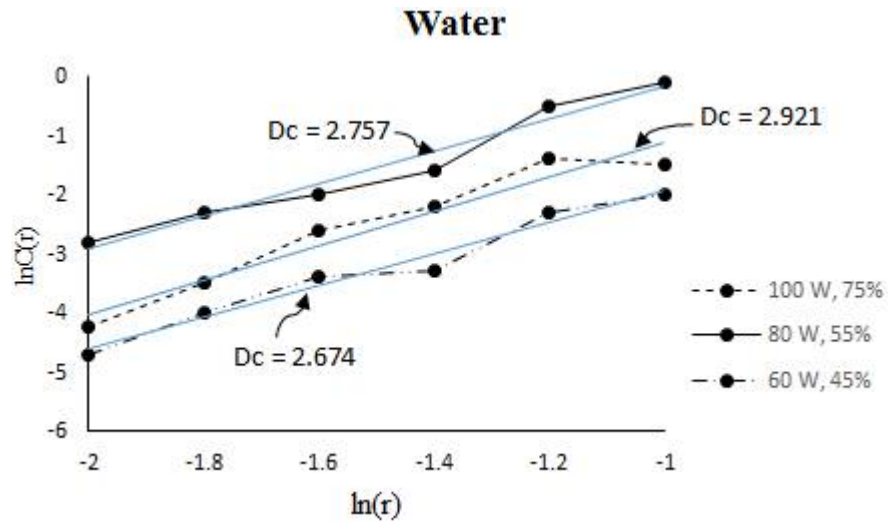


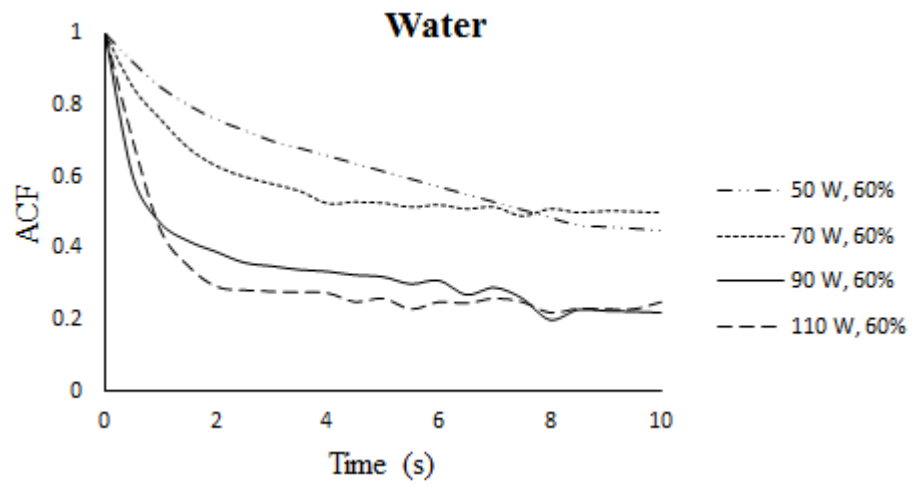
Figure 5.17. Correlation dimension values (D_c) with water (a) and ethanol (b) as working fluids

Figure 5.17 illustrates the correlation dimensions under evaporator heating powers of 60 W, 80 W and 100 W with filling ratios of 45%, 55% and 75%, respectively at condenser temperature of 20 °C for water and ethanol. Values of 2.674, 2.757 and 2.921 were obtained for water under mentioned operating conditions. In addition, values of 2.806, 2.922 and 3.263 were obtained for ethanol under the same operating conditions. It is evident for both water and ethanol that by increasing the evaporator heating power and filling ratio, the slope of the curves and correlation dimension increase. Besides, correlation dimension values for ethanol are higher than water under the same operating conditions. High values of correlation dimension refers to high frequency, small scale temperature oscillations, caused by miniature bubbles or short vapor plugs dynamically flowing in PHP tubes [51]. The lower correlation dimension corresponds to low frequency of temperature oscillations and large amplitude caused by large bubbles in the PHP. It is notable that value of correlation dimension indicates complexity of a system. Then by increasing the correlation dimension, the complexity of the PHP system increases.

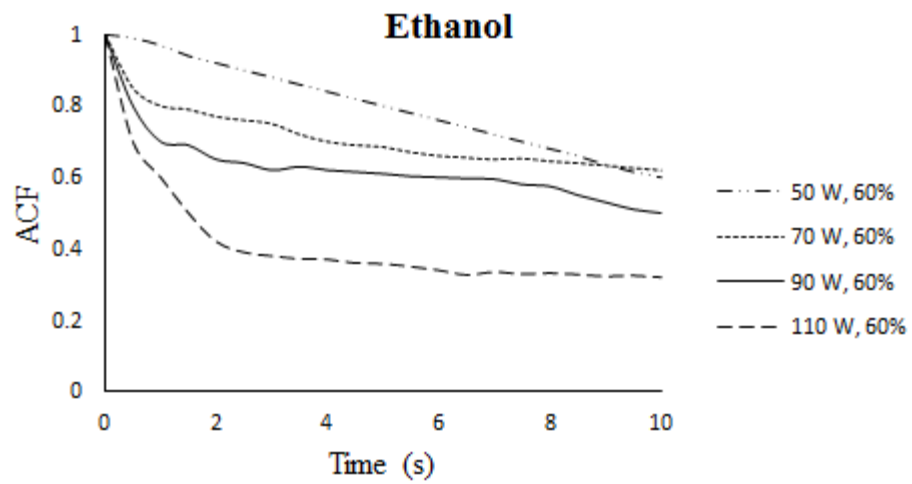
5.2.4 Autocorrelation Function

Autocorrelation is the cross-correlation of a signal with itself at different points in time (that is what the cross stands for). Informally, it is the similarity between the observations as a function of the time lag between them. It is a mathematical tool for finding repeating patterns, such as the presence of a periodic signal obscured by noise, or identifying the missing fundamental frequency in a signal implied by its harmonic

frequencies. It is often used in signal processing for analyzing functions or series of values, such as time domain signals. The autocorrelation of a random process describes the correlation between values of the process at different times, as a function of the two times or of the time lag. Often in time series it is required to compare the value observed at one time point to a value observed one or more time points earlier. Such prior values are known as lagged values. If there is some pattern in how the values of time series change from observations to observation, it would be so useful to analyze the time series. The correlation between the original time series values and the corresponding τ -lagged values is called autocorrelation of order τ . The Autocorrelation Function (ACF) provides the correlation between the serial correlation coefficients for consecutive lags. AFC helps to determine how quickly signals or process change with respect to time and whether a process has a periodic component. The autocorrelation function will have its largest value of AFC=1 at $\tau=0$. Figure 18 illustrates the autocorrelation function (AFC) of time series at filling ratio of 60% and four heating powers of 50 W, 70 W, 90 W and 110 W.



(a)



(b)

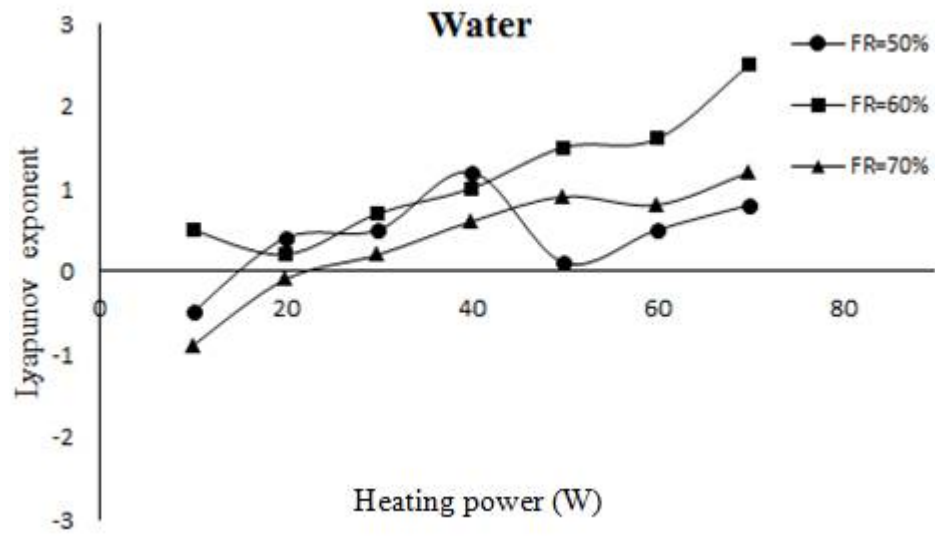
Figure 5.18 Autocorrelation function versus time with water (a) and ethanol (b) as working fluids

Behavior of ACF indicates the prediction ability of the system [60]. The autocorrelation function will have its largest value of AFC=1 at $\tau=0$. Figure 18 shows that the autocorrelation function decreases with time. Decreasing of the ACF shows that the prediction ability is finite as a signature of chaos. By increasing the evaporator heating power, ACF decreases for water and ethanol. In addition, linear behavior of the ACF changes gradually to exponential behavior by increasing the heating power. Although the same operating conditions were applied for the PHP with water and ethanol as working fluids, change in working fluid did not lead to any particular conclusion for ACF behavior.

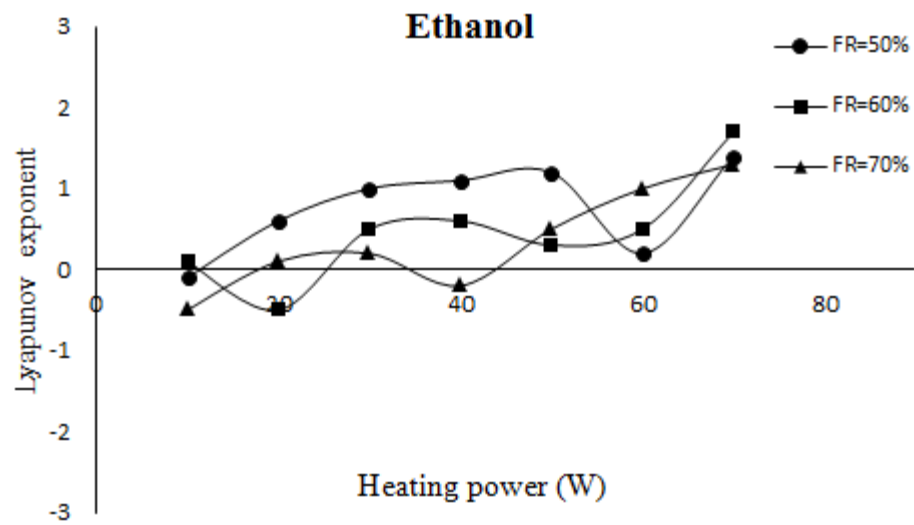
5.2.5 Lyapunov Exponent

Lyapunov exponents are dynamical quantities. Consider two points in a space, X_0 and $X_0 + \Delta x_0$, each of which will generate an orbit in that space using some equation or system of equations. These orbits can be thought of as parametric functions of a variable that is something like time. If we use one of the orbits a reference orbit, then the separation between the two orbits will also be a function of time. Because sensitive dependence can arise only in some portions of a system (like the logistic equation), this separation is also a function of the location of the initial value and has the form $\Delta x(X_0, t)$. In a system with attracting fixed points or attracting periodic points, $\Delta x(X_0, t)$ diminishes asymptotically with time. If a system is unstable, like pins balanced on their points, then the orbits diverge exponentially for a while, but eventually settle down. For chaotic points, the function $\Delta x(X_0, t)$ will behave erratically.

In the pulsating heat pipe, let X_p be the position of the liquid plug relative to its initial position. Given some initial condition X_0 , consider a nearby point $X_{0+\delta}$, where the initial separation δ_0 is extremely small. Let δ_n be the separation after n steps. If $|\delta_n| \approx |\delta_0| e^{n\lambda}$, λ will be the Lyapunov exponent. A positive λ means an exponential divergence of nearby trajectories which is a signature of chaos. A negative λ corresponds to stable fixed point and if $\lambda=0$, this means stable limit cycle.



(a)



(b)

Figure 5.19. Lyapunov exponents versus evaporator heating power at different filling ratios with water (a) and ethanol (b) as working fluids

Figure 5.19 illustrates the Lyapunov exponents versus evaporator heating power at three filling ratio of 50%, 60% and 70% at condenser temperature of 20 °C with water and ethanol as working fluids. Mostly, Lyapunov exponent increases by increasing heating power in Figure 5.19a with water as working fluid. Three exceptional points can be seen at heating powers of 20 W, 50 W and 60 W for filling ratios of 60 %, 50% and 70%. Negative Lyapunov exponents appeared at heating power of 10 W with FR of 70%, heating power of 10 W with FR of 50% and heating power of 20 W with FR of 70% indicating PHP is not in chaotic state under these operating conditions. Lyapunov exponent increases by increasing the heating power as well for the PHP with ethanol as working fluid as shown in Figure 5.19b. Exceptional points from this behavior exist under some operating conditions. Negative Lyapunov exponents appeared at heating power of 10 W with FR of 70%, heating power of 10 W with FR of 50%, heating power of 20 W with FR of 60% and heating power of 40 W with FR of 70% indicating PHP is not in chaotic state under these operating conditions. It is evident in Figure 5.18 that range of Lyapunov exponent value for the PHP with water and ethanol as working fluids are similar. This indicates strong dependency of Lyapunov exponent to the structure and dimensions of the PHP which is the same for all operating conditions in current study.

5.2.6 Phase Space Reconstruction

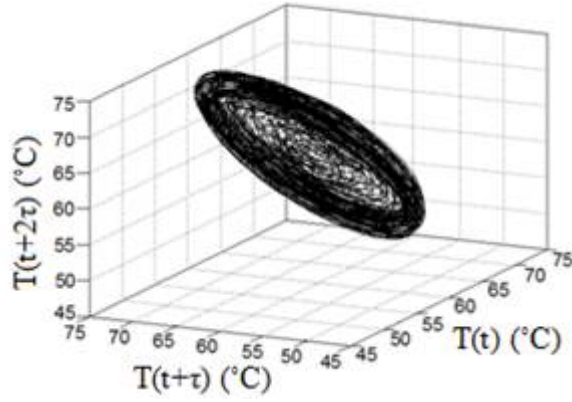
To reconstruct a useful version of the internal dynamics for a given time series from a sensor on a single state variable $x_i(t)$ in a n-dimensional dynamical system, delay-

coordinate embedding can be used. If the embedding is performed correctly, the involved theorems guarantee that the reconstructed dynamics is topologically identical to the true dynamics of the system, and therefore that the dynamical invariants are also identical. This is an extremely powerful correspondence; it implies that conclusions drawn from the embedded or reconstruction-space dynamics are also true of the real unmeasured dynamics. This implies, for example, that one can reconstruct the dynamics of the earth's weather simply by setting a thermometer on a windowsill [65]. Considering a data set comprised of samples $x_i(t)$ of a signal state variable x_i in a n -dimensional system, measured once every Δt seconds. To embed such a data set, we construct r -dimensional reconstruction-space vectors $T(t)$ from r time-delayed samples of the $x_i(t)$, such that

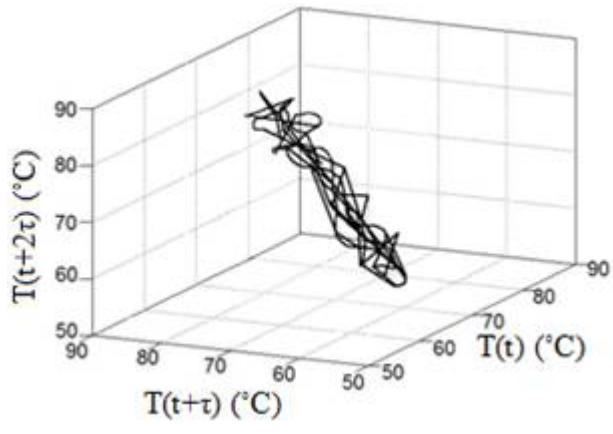
$$T(t)=[x_i(t), x_i(t+\tau), x_i(t+2\tau), \dots, x_i(t+(m-1)\tau)] \quad (5.1)$$

In a pulsating heat pipe, the time series is usually a sequence of temperature values which depends on the current phase space, taken at different points in time. It is important that given enough dimensions (r) and the right delay (τ), the reconstruction-space dynamics and the true, unobserved state-space dynamics are topologically identical. More, formally, the reconstruction-space and state-space trajectories are guaranteed to be equivalent if $r \geq 2n+1$.

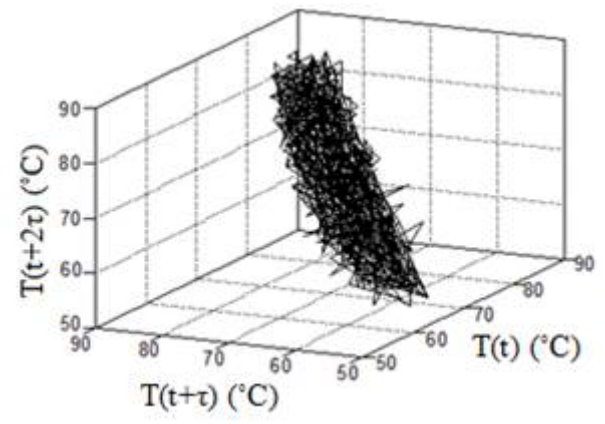
Regarding above explanations, the attractor reconstructions were carried out. It is evident in Figure 5.20a the attractor pattern is like an O-ring structure which is mostly for periodic or quasi-periodic systems. Then, the PHP behavior under heating power of 75 W, condenser temperature of 20 °C, filling ratio of 55% and ethanol as working fluid is not in a chaotic state. Figure 5.20b illustrates the attractor pattern under heating power of 40 W, condenser temperature of 20 °C, filling ratio of 60% and water as working fluid. It can be seen that the attractor pattern at this low heating power is narrow, slim and elongated, corresponding to low dimension characteristic of the temperature oscillation and chaotic properties of PHP. Figure 5.20c illustrates the attractor pattern under heating power of 80 W, condenser temperature of 20 °C, filling ratio of 65% and ethanol as working fluid. At this higher heating power, the attractor pattern is more complex. In addition, it has slight wider and more scattered distribution than the attractor pattern in Figure 5.20b, corresponding to a higher dimension characteristic of the temperature oscillation and chaotic properties of PHP. Figures 5.20b and 5.20c are strong evidence of deterministic chaotic systems under mentioned operating conditions.



(a)



(b)



(c)

Figure 5.20. Reconstructed 3D attractor patterns under (a): heating power of 75 W, condenser temperature of 20 °C, filling ratio of 55% and ethanol as working fluid (b): heating power of 40 W, condenser temperature of 20 °C, filling ratio of 60% and water as working fluid (c): heating power of 80 W, condenser temperature of 20 °C, filling ratio of 65% and ethanol as working fluid

5.2.7 Thermal Performance

In current study, effects of filling ratio and working fluid on the thermal performance of the PHP have been investigated. Filling ratios of 35%, 45%, 55%, 65% and 75% for water and ethanol have been tested under different heating powers and condenser temperature of 20 °C. For the traditional heat pipes, the filling ratio range of working fluid is lower comparing to the PHPs. Large amount of working fluid inside the channels causes liquid blockage and reduces pressure difference between heating and cooling sections which can stop the oscillation movement. But for the PHPs a filling ratio that is higher than that of traditional heat pipes is required. The overall thermal resistance of a PHP is defined as the difference average temperatures between evaporator and condenser divided by the heating power. For evaporator average temperature, 15 points (#2, #3, #4, #7, #8, #9, #12, #13, #14, #17, #18, #18, #22, #23 and #24) were used to calculate the average temperature. Since condenser has constant temperature, calculation is not necessary to get the average temperature which is equal to that constant value. Equation (5.2) defines the thermal resistance of a PHP.

$$R = \frac{T_e - T_c}{Q} \quad (5.2)$$

where T_e is the evaporator average temperature, T_c is the condenser average temperature and Q is the evaporator heating power.

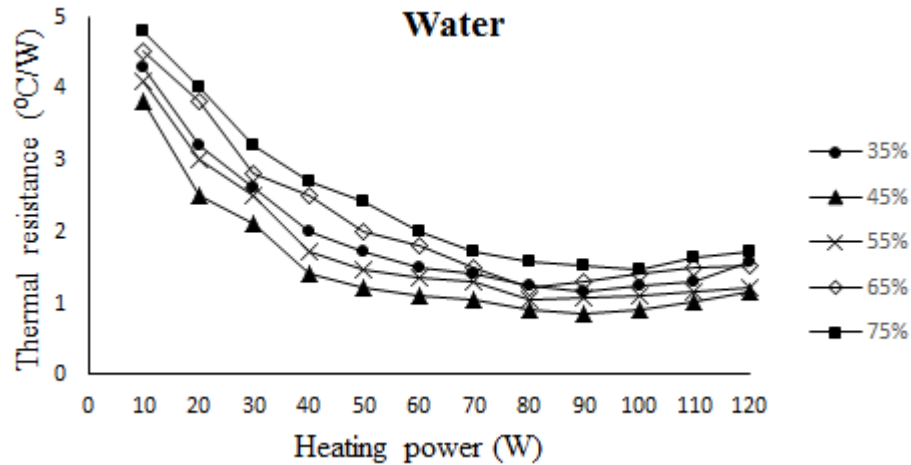


Figure 5.21. Thermal resistance versus heating power at different filling ratios and water as working fluid

Figure 5.21 illustrates the thermal resistance variation with respect to evaporator heating power at different filling ratios and water as working fluid. A general behavior of thermal resistance can be seen in Figure 5.21. At all filling ratios, by increasing the heating power, the thermal resistance decreases initially to reach a minimum value as an optimal point. Thermal resistance increases by increasing the heating power afterwards. This optimal point is important since at related operating conditions, the pulsating heat pipe transfers the maximum heat flux with a minimum temperature difference between the evaporator and condenser leads to a better thermal performance of the PHP. The minimum thermal resistance occurs at different heating powers for different filling ratios. It is obvious in Figure 5.20 that thermal resistance has lower values at filling ratio of 45%

comparing with other filling ratios. The minimum thermal resistance of $0.85\text{ }^{\circ}\text{C}/\text{W}$ happens at heating power of 90 W for this filling ratio.

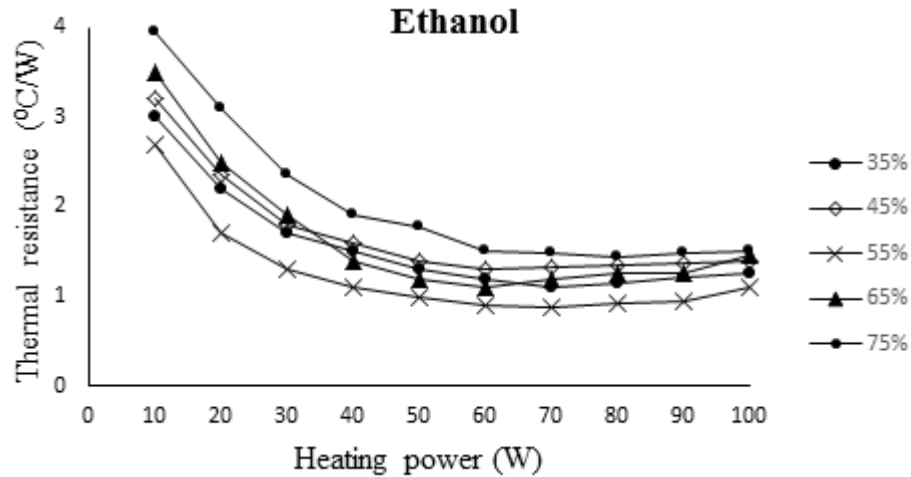


Figure 5.22 Thermal resistance versus heating power at different filling ratios and ethanol as working fluid

As shown in Figure 5.22, the same conclusion of general behavior and optimal point of thermal resistance is applicable for ethanol as well. Thermal resistance has lower values at filling ratio of 55%. The minimum thermal resistance of $0.88\text{ }^{\circ}\text{C}/\text{W}$ happens at heating power of 70 W for this filling ratio.

5.3 Conclusion

Numerical simulations have been carried out to investigate the chaotic and thermal behaviors of a 3D closed-loop pulsating heat pipe. Heat flux and constant temperature boundary conditions were applied for evaporator and condenser respectively. Water and ethanol were used as working fluids. Volume fractions of liquid and vapor were obtained and analyzed under different operating conditions. Comparison of thermal resistance behavior versus heating power between simulation results of current study and experimental results of Shafii et al. [64] confirmed a good agreement between simulation and experimental results. The following conclusions can be drawn from this work:

Spectral analysis of temperature time series using Power Spectrum Density showed existence of dominant peak in PSD diagram indicates periodic or quasi-periodic behavior in temperature oscillations at particular frequencies.

Absence of dominant peak in PSD diagram and its decay with respect to time was a signature of chaotic state under some operating conditions.

It was found for both water and ethanol as working fluids by increasing the evaporator heating power and filling ratio, correlation dimension increases.

Correlation dimension values for ethanol were higher than water under the same operating conditions. High values of correlation dimension referred to high frequency, small scale temperature oscillations, caused by miniature bubbles or short vapor plugs dynamically flowing in PHP tubes.

Decay of autocorrelation function with respect to time indicated finite prediction ability of the system. Change in working fluid did not lead to any particular conclusion for ACF behavior.

Similar range of Lyapunov exponent value for the PHP with water and ethanol as working fluids indicated strong dependency of Lyapunov exponent to the structure and dimensions of the PHP.

An O-ring structure pattern was obtained for reconstructed 3D attractor at periodic or quasi-periodic behavior of temperature oscillations.

Optimal points were found in case of thermal performance with minimum thermal resistance of $0.85 \text{ }^{\circ}\text{C/W}$ at heating power of 90 W and filling ratio of 45% for water as working fluid and minimum thermal resistance of $0.88 \text{ }^{\circ}\text{C/W}$ at heating power of 70 W and filling ratio of 55% for ethanol as working fluid.

Reference

- [1] Mishima, K. and Hibiki, T., 1996. Some characteristics of air-water two-phase flow in small diameter vertical tubes. *International Journal of Multiphase Flow*, 22(4), pp.703-712.
- [2] Thome, J.R. and Hajal, J.E., 2003. Two-phase flow pattern map for evaporation in horizontal tubes: latest version. *Heat Transfer Engineering*, 24(6), pp.3-10.
- [3] Wojtan, L., Ursenbacher, T. and Thome, J.R., 2005. Investigation of flow boiling in horizontal tubes: Part I—A new diabatic two-phase flow pattern map. *International Journal of Heat and Mass Transfer*, 48(14), pp.2955-2969.
- [4] Zürcher, O., Favrat, D. and Thome, J.R., 2002. Development of a diabatic two-phase flow pattern map for horizontal flow boiling. *International Journal of Heat and Mass Transfer*, 45(2), pp.291-301.
- [5] Chen, Q., Xu, J., Sun, D., Cao, Z., Xie, J. and Xing, F., 2013. Numerical simulation of the modulated flow pattern for vertical upflows by the phase separation concept. *International Journal of Multiphase Flow*, 56, pp.105-118.
- [6] Banasiak, R., Wajman, R., Jaworski, T., Fiderek, P., Fidos, H., Nowakowski, J. and Sankowski, D., 2014. Study on two-phase flow regime visualization and identification using 3D electrical capacitance tomography and fuzzy-logic classification. *International Journal of Multiphase Flow*, 58, pp.1-14.

- [7] De Mesquita, R.N., Masotti, P.H.F., Penha, R.M.L., Andrade, D.A., Sabundjian, G., Torres, W.M. and Macedo, L.A., 2012. Classification of natural circulation two-phase flow patterns using fuzzy inference on image analysis. *Nuclear Engineering and Design*, 250, pp.592-599.
- [8] Baker, O., 1953, January. Design of pipelines for the simultaneous flow of oil and gas. In *Fall Meeting of the Petroleum Branch of AIME*. Society of Petroleum Engineers.
- [9] Mandhane, J.M., Gregory, G.A. and Aziz, K., 1974. A flow pattern map for gas—liquid flow in horizontal pipes. *International Journal of Multiphase Flow*, 1(4), pp.537-553.
- [10] Hubbard, M.G. and Dukler, A.E., 1966. The characterization of flow regimes for horizontal two-phase flow. *Heat Trans. & Fluid Mech. Inst., M. A. Saad and JA Miller, eds., Stanford U. Press*, pp.101-121.
- [11] Zeguai, S., Chikh, S. and Tadrist, L., 2013. Experimental study of two-phase flow pattern evolution in a horizontal circular tube of small diameter in laminar flow conditions. *International Journal of Multiphase Flow*, 55, pp.99-110.
- [12] Pietrzak, M., 2014. Flow patterns and volume fractions of phases during liquid—liquid two-phase flow in pipe bends. *Experimental Thermal and Fluid Science*, 54, pp.247-258.

- [13] Zhao, Y., Bi, Q. and Hu, R., 2013. Recognition and measurement in the flow pattern and void fraction of gas–liquid two-phase flow in vertical upward pipes using the gamma densitometer. *Applied Thermal Engineering*, 60(1), pp.398-410.
- [14] Babuška, R., 2012. *Fuzzy modeling for control* (Vol. 12). Springer Science & Business Media.
- [15] Hughmark, G.A. and Pressburg, B.S., 1961. Holdup and pressure drop with gas-liquid flow in a vertical pipe. *AIChE Journal*, 7(4), pp.677-682.
- [16] Fang, J.H. and Chen, H.C., 1997. Fuzzy modelling and the prediction of porosity and permeability from the compositional and textural attributes of sandstone. *Journal of Petroleum Geology*, 20(2), pp.185-204.
- [17] Hambalek, N. and González, R., 2003, January. Fuzzy logic applied to lithofacies and permeability forecasting case study: sandstone of Naricual formation, El Furrial field, Eastern Venezuela Basin. In *SPE Latin American and Caribbean Petroleum Engineering Conference*. Society of Petroleum Engineers.
- [18] Jang, J.S.R., Sun, C.T. and Mizutani, E., 1997. Neuro-fuzzy and soft computing: a computational approach to learning and machine intelligence.
- [19] Juang, C.F. and Lin, C.T., 1998. An online self-constructing neural fuzzy inference network and its applications. *Fuzzy Systems, IEEE Transactions on*, 6(1), pp.12-32.

- [20] Jang, J.S.R., 1993. ANFIS: adaptive-network-based fuzzy inference system. *Systems, Man and Cybernetics, IEEE Transactions on*, 23(3), pp.665-685.
- [21] Taitel, Y. and Dukler, A.E., 1976. A model for predicting flow regime transitions in horizontal and near horizontal gas-liquid flow. *AIChE Journal*, 22(1), pp.47-55.
- [22] Takagi, T. and Sugeno, M., 1983, July. Derivation of fuzzy control rules from human operator's control actions. In *Proceedings of the IFAC symposium on fuzzy information, knowledge representation and decision analysis* (Vol. 6, pp. 55-60). sn.
- [23] Zadeh, L.A., 1965. Fuzzy sets. *Information and control*, 8(3), pp.338-353.
- [24] Gao, Z.K., Fang, P.C., Ding, M.S. and Jin, N.D., 2015. Multivariate weighted complex network analysis for characterizing nonlinear dynamic behavior in two-phase flow. *Experimental Thermal and Fluid Science*, 60, pp.157-164.
- [25] Gao, Z.K., Yang, Y.X., Fang, P.C., Jin, N.D., Xia, C.Y. and Hu, L.D., 2015. Multi-frequency complex network from time series for uncovering oil-water flow structure. *Scientific reports*, 5.
- [26] Zhang, Y., Zou, Q.P. and Greaves, D., 2012. Air–water two-phase flow modelling of hydrodynamic performance of an oscillating water column device. *Renewable Energy*, 41, pp.159-170.

- [27] Anandan, S.S. and Ramalingam, V., 2008. Thermal management of electronics: A review of literature. *Thermal science*, 12(2), pp.5-26.
- [28] Myers, S.H. and Smith, A.N., 2008, June. Demonstration of combined spray and evaporative cooling of an electromagnetic railgun. In *Electromagnetic Launch Technology, 2008 14th Symposium on* (pp. 1-6). IEEE.
- [29] Akachi, H., 1990. *Structure of a heat pipe. US, Patent 4921041*.
- [30] Vasiliev, L.L., 2002. Heat Pipe Thermal Control for Sorption Machines. In *Proceedings of 12th International Heat Pipe Conference* (pp. 65-73).
- [31] Liang, S.B. and Ma, H.B., 2004. Oscillating motions of slug flow in capillary tubes. *International communications in heat and mass transfer*, 31(3), pp.365-375.
- [32] Zuo, Z.J., North, M.T. and Ray, L., 1999. Combined pulsating and capillary heat pipe mechanism for cooling of high heat flux electronics. *ASME-PUBLICATIONS-HTD*, 364, pp.237-244.
- [33] Nishio, S., Nagata, S.I., Numata, S. and Shirakashi, R., 2003. Study of thermal characteristics of bubble-driven heat-transport device. *Heat Transfer—Asian Research*, 32(2), pp.167-177.
- [34] Cao, Y. and Gao, M., 2002. Wickless network heat pipes for high heat flux spreading applications. *International Journal of Heat and Mass Transfer*, 45(12), pp.2539-2547.

- [35] Nishio, S., 2004. Single-phase laminar-flow heat transfer and two-phase oscillating-flow heat transport in microchannels. *Heat transfer engineering*, 25(3), pp.31-43.
- [36] Shafii, M.B., Faghri, A. and Zhang, Y., 2001. Thermal modeling of unlooped and looped pulsating heat pipes. *Journal of Heat Transfer*, 123(6), pp.1159-1172.
- [37] Shafii, M.B., Faghri, A. and Zhang, Y., 2002. Analysis of heat transfer in unlooped and looped pulsating heat pipes. *International journal of Numerical Methods for heat & fluid flow*, 12(5), pp.585-609.
- [38] Zhang, Y. and Faghri, A., 2002. Heat transfer in a pulsating heat pipe with open end. *International Journal of Heat and Mass Transfer*, 45(4), pp.755-764.
- [39] Zhang, Y. and Faghri, A., 2003. Oscillatory flow in pulsating heat pipes with arbitrary numbers of turns. *Journal of Thermophysics and Heat Transfer*, 17(3), pp.340-347.
- [40] Zhang, Y. and Faghri, A., 2008. Advances and unsolved issues in pulsating heat pipes. *Heat Transfer Engineering*, 29(1), pp.20-44.
- [41] Shao, W. and Zhang, Y., 2011. Thermally-induced oscillatory flow and heat transfer in an oscillating heat pipe. *Journal of Enhanced Heat Transfer*, 18(3).
- [42] Kim, S., Zhang, Y. and Choi, J., 2013. Entropy generation analysis for a pulsating heat pipe. *Heat Transfer Research*, 44(1).

- [43] Kim, S., Zhang, Y. and Choi, J., 2013. Effects of fluctuations of heating and cooling section temperatures on performance of a pulsating heat pipe. *Applied Thermal Engineering*, 58(1), pp.42-51.
- [44] Ma, H.B., Borgmeyer, B., Cheng, P. and Zhang, Y., 2008. Heat transport capability in an oscillating heat pipe. *Journal of Heat Transfer*, 130(8), p.081501.
- [45] Tong, B.Y., Wong, T.N. and Ooi, K.T., 2001. Closed-loop pulsating heat pipe. *Applied thermal engineering*, 21(18), pp.1845-1862.
- [46] Borgmeyer, B. and Ma, H., 2007. Experimental investigation of oscillating motions in a flat plate pulsating heat pipe. *Journal of Thermophysics and Heat Transfer*, 21(2), pp.405-409.
- [47] Qu, J., Wu, H.Y. and Cheng, P., 2010. Thermal performance of an oscillating heat pipe with Al₂O₃-water nanofluids. *International Communications in Heat and Mass Transfer*, 37(2), pp.111-115.
- [48] Dobson, R.T. and Harms, T.M., 1999, September. Lumped parameter analysis of closed and open oscillatory heat pipes. In *Proceedings of the 11th International heat pipe Conference* (pp. 137-142).
- [49] Khandekar, S., Dollinger, N. and Groll, M., 2003. Understanding operational regimes of closed loop pulsating heat pipes: an experimental study. *Applied Thermal Engineering*, 23(6), pp.707-719.

- [50] Khandekar, S. and Groll, M., 2004. An insight into thermo-hydrodynamic coupling in closed loop pulsating heat pipes. *International Journal of Thermal Sciences*, 43(1), pp.13-20.
- [51] Khandekar, S., Schneider, M. and Groll, M., 2002. Mathematical modeling of pulsating heat pipes: state of the art and future challenges. *Heat and Mass Transfer*, SK Saha, SP Venkateshen, BVSSS Prasad, and SS Sadhal, eds., Tata McGraw-Hill Publishing Company, New Delhi, India, pp.856-862.
- [52] Dobson, R.T., 2004. Theoretical and experimental modelling of an open oscillatory heat pipe including gravity. *International Journal of Thermal Sciences*, 43(2), pp.113-119.
- [53] Dobson, R.T., 2005. An open oscillatory heat pipe water pump. *Applied thermal engineering*, 25(4), pp.603-621.
- [54] Xiao-Ping, L. and Cui, F.Z., 2008. Modelling of Phase Change Heat Transfer System for Micro-channel and Chaos Simulation. *Chinese Physics Letters*, 25(6), p.2111.
- [55] Song, Y. and Xu, J., 2009. Chaotic behavior of pulsating heat pipes. *International Journal of Heat and Mass Transfer*, 52(13), pp.2932-2941.
- [56] Louisos, W.F., Hitt, D.L. and Danforth, C.M., 2013. Chaotic flow in a 2D natural convection loop with heat flux boundaries. *International Journal of Heat and Mass Transfer*, 61, pp.565-576.

- [57] Ridouane, E.H., Danforth, C.M. and Hitt, D.L., 2010. A 2-D numerical study of chaotic flow in a natural convection loop. *International Journal of Heat and Mass Transfer*, 53(1), pp.76-84.
- [58] Louisos, W.F., Hitt, D.L. and Danforth, C.L., 2015. Chaotic natural convection in a toroidal thermosyphon with heat flux boundaries. *International Journal of Heat and Mass Transfer*, 88, pp.492-507.
- [59] FLUENT, A., 6.3. Theory Manual. 2005. Fluent Inc. Central Source Park, 10 Cavendish Court, Lebanon, NH 03766, USA.
- [60] Kantz, H. and Schreiber, T., 2004. *Nonlinear time series analysis* (Vol. 7). Cambridge university press.
- [61] Strogatz, S.H., 2014. *Nonlinear dynamics and chaos: with applications to physics, biology, chemistry, and engineering*. Westview press.
- [62] Gao, J., Cao, Y., Tung, W.W. and Hu, J., 2007. *Multiscale analysis of complex time series: integration of chaos and random fractal theory, and beyond*. John Wiley & Sons.
- [63] Zaslavsky, G.M., 2007. *The physics of chaos in Hamiltonian systems*.
- [64] Shafii, M.B., Arabnejad, S., Saboohi, Y. and Jamshidi, H., 2010. Experimental investigation of pulsating heat pipes and a proposed correlation. *Heat Transfer Engineering*, 31(10), pp.854-861.

[65] Bradley, E., 1999. Time-series analysis. *Intelligent Data Analysis: An Introduction*, Springer.

VITA

Sam Pouryoussefi was born in Kalamazoo, Michigan in 1982. He went to ALBORZ high school in Tehran and after graduation, entered K.N. Toosi University of Technology. After graduating with a Bachelor of Science in Mechanical Engineering, he continued his Master in Aerospace Engineering. His Master's thesis focused on experimental investigation of cascade of stator blades. He started his PhD at University of Missouri-Columbia in January 2013. Sam was a research assistant and teaching assistant (in Thermal/Fluid laboratory) during his PhD in Mechanical and Aerospace Engineering department. His dissertation focused on investigation of two phase flow using automatic controller system and chaotic approach.